Development of the Online Data Reduction System and Feasibility Studies of 6-Layer Tracking for the Belle II Pixel Detector

vorgelegt von
David Münchow

24. April 2015

Justus-Liebig-Universität Gießen
II. Physikalisches Institut
Heinrich-Buff-Ring 16
D-35392 Gießen

Dekan:	Prof. Dr. Peter Jens Klar
1. Berichterstatter:	Prof. Dr. Wolfgang Kühn
2. Berichterstatter:	Prof. Dr. Alfred Müller

CONTENTS

Das Belle II Experiment, die Aufrüstung vom Belle Experiment, am KEK (Hochenergie-Beschleuniger-Forschungsorganisation) in Tsukuba, Japan, wird gebaut um z.B. fundamentale Fragen, die nicht durch das Standardmodell der Teilchenphysik erklärt werden können, zu beantworten. Zu diesem Zweck ist es notwendig, Zerfälle mit hoher Prezision zu messen.

Um in der Lage zu sein, Zerfallsprodukte mit einer hohen Vertexauflösung messen zu können, hat man sich entschlossen einen Pixeldetektor (PXD) mit einem inneren Radius von nur 14 mm mit geringer Distanz um das Strahlrohr (äußerer Radius 12,5 mm) hinzuzufügen. Dies erhöht die Vertexauflösung und es ist möglich die Rekonstruktionseffizienz und -genauigkeit zu verbessern. Auf Grund der kurzen Distanz zum Wechselwirkungspunkt erwarten wir eine Okkupanz von bis zu 3% im Pixeldetektor, die hauptsächlich durch Hintergrundeffekte verursacht wird. Diese wird eine erwartete Datenrate von etwa 20 GB/s generieren, welche die Bandbreitenbeschränkungen des Datenspeichers überschreitet. Basierend auf Treffern in den äußeren Detektoren werden Rückprojektionen von Spuren durchgeführt und „Region-of-Interests" (Region von Interesse – ROI) auf den PXD Sensoren berechnet. Basierend auf diesen ROIs werden die Daten reduziert.

Als Hardware Plattform werden „Compute Nodes" (Rechen Knoten – CN) verwendet die in enger Zusammenarbeit vom Institute of High Energy Physics (IHEP) in Peking zusammen mit der Justus-Liebig-Universität Gießen entwickelt wurden.

In dieser Arbeit präsentiere ich meine Entwicklung des ROI basierenden Datenreduktionsalgorithmus sowie meine Machbarkeitsstudie über ein zukünftiges „6-Layer-Tracking" (6 Lagen Spuhrensuche).

Online Datenreduktion für Belle II

Ein erster Test mit der vollständigen Vernetzung der DAQ und Prototypsensoren des PXD und des SVD wurde am DESY durchgeführt. Zur Verifizierung der ROI Selektions Logik wurde eine vollständige Aufzeichnung der Ein- und Ausgabedaten eingefügt.

Mit diesem Aufbau habe ich $1{,}2 \cdot 10^6$ Ereignisse mit insgesamt $4{,}8 \cdot 10^8$ Treffern aufgezeichnet. Die Okkupanz wurde hierbei von ursprünglich $\approx 0{,}80\%$ durch meine ROI Selektions Logik um einen Faktor $6{,}9$ auf $\approx 0{,}12\%$ rediziert unter Verwerfung aller Treffer außerhalb jeglicher ROIs.

Zusätzlich habe ich die ROI Positionierung untersucht und erhielt das Ergebnis eines Abstandes zwische ROI Mittelpunkt und Treffer von $17{,}624 \pm 0{,}029$ bei einer hauptsächlichen Versatzrichtung von $\frac{\pi}{2}$ und $\frac{3\pi}{2}$. Mit einer genaueren Position der ROIs, könnte ihre Größe reduziert werden was den Reduktionsfaktor verbessern würde.

Machbarkeitsstudie über ein „6-Layer-Tracking" für Belle II

In diesem Teil habe ich die Grenzen des aktuell geplanten Systems mit ROI Selektion und „Cluster-Rescue" (Clusterrettung) untersucht. Des weiteren habe ich untersucht ob es möglich wäre die Qualität der Daten Selektion durch ein „6-Layer-Tracking" zu verbessern. Ein Konzept bei dem alle Daten von PXD und SVD vor der Reduktion genutzt werden würden. Das aktuelle System bezieht die PXD Daten nicht in die Spurensuche ein. In meiner Untersuchung konzentriere ich mich auf zwei Fälle bei denen es zu Problemen bei der Ereignisrekonstruktion kommen könnte: sekundäre Vertices und geladene Teichen mit niedrigem Impuls.

Als Beispiel für sekudäre Vertices habe ich Ereignisse mit K_S^0 ausgewählt. Ich fand heraus, dass ein „6-Layer-Tracking" die Anzahl der Rekonstruierbaren Pionen aus K_S^0 um etwa $0{,}75\%$ erhöhen kann im Vergleich zum aktuellen System. Für transversale Impulse von etwa $p_t \approx 200\,\mathrm{MeV}$ die Zunahme kann sogar $\approx 2\%$ erreichen.

Als ein Beispiel für Teilchen mit niedrigem Impuls habe ich eine Zerfallskanal von $Z_c(3900)^-$ über D^{*-} welches in $\overline{D}^0$ und π^- zefällt gewählt. Dieses Pion hat einen sehr kleinen Impuls und erreicht vielleicht nicht genügend SVD lagen für eine Spurensuche ohne PXD. Hier ist mein Ergebnis, dass die Pionen mit solch niedrigen transversalen Impulsen in der minimal ionisiereden Impulsregion liegen. Hierdurch deckt das „Cluster-Rescue" diese Pionen bereits ab. Die Zunahme durch ein „6-Layer-Tracking" wird nur $0{,}12\%$ sein.

ABSTRACT

The Belle II experiment, the upgrade of the Belle experiment, at KEK (High Energy Accelerator Research Organization) in Tsukuba, Japan, will be built to answer fundamental questions that are not covered by the Standard Model of particle physics. For this reason, decays should be observed with high precision.

To be able to measure all decay products with a very accurate vertex resolution, it was decided to add a Pixel Detector (PXD) with an inner radius of only $14\,\mathrm{mm}$ in short distance around the beam (outer radius $12.5\,\mathrm{mm}$). This increases the vertex resolution and it is possible to improve the reconstruction efficiency and accuracy. Because of the short distance to the interaction point, we expect to have a background induced occupancy of up to 3% on the pixel detector. This generates an expected data rate of about $20\,\mathrm{GB/s}$ and exceeds the bandwidth limitations of the data storage. Based on hits in the outer detectors, back projections of particle tracks are performed and Region of Interests (ROI) on the PXD sensors are calculated. Based on those ROIs the data are reduced.

In this thesis I present my development of the ROI based data reduction algorithm as well as my feasibility studies about a future 6-layer tracking.

Online Data Reduction for Belle II

A first test with the whole DAQ integration and prototype sensors of PXD and SVD had been performed at DESY. For the verification of the ROI selection logic a full recording of in- and output data was included. With this setup I recorded $1.2 \cdot 10^6$ events containing in total $4.8 \cdot 10^8$ hits. The occupancy of originally $\approx 0.80\%$ was reduced with my ROI selection logic by a factor of 6.9 to $\approx 0.12\%$ by rejecting all hits outside any ROI.

In addition I investigated the ROI positioning and got a result of a distance between ROI center and hit of 17.624 ± 0.029 with a main offset direction of $\frac{\pi}{2}$ and $\frac{3\pi}{2}$. With a more accurate position of the ROIs their size could be reduced which would optimize the reduction factor.

Feasibility Studies of 6-Layer Tracking at Belle II

In this part I investigated the limitations of the currently planned system with ROI selection and cluster rescue. Furthermore I investigated if it would be possible to increase the quality of data selection by adding a 6-layer tracking, a concept which would use all unreduced data from PXD and SVD to perform a tracking. The recent system does not include the PXD data in their tracking. In my studies I focused on two cases which could cause problems at the reconstruction of events: secondary vertex and low momentum charged particles.

As an example for secondary vertex events I chose events including a K_S^0. I investigated that a 6-layer tracking can increase the number of reconstructable pions from K_S^0 about 0.75% compared to the recently system. For transversal momenta of about $p_t \approx 200\,\mathrm{MeV}$ this increase can reach even $\approx 2\%$.

For an example of low momentum particles I chose a decay channel of $Z_c(3900)^-$ via D^{*-} which decays in $\overline{D}^0$ and π^-. This pion has a very small momentum and may not reach enough SVD layer for a tracking without PXD. Here my result is, that the pions with such a low transversal momentum will be below the minimum ionizing momentum region. Therefore the cluster rescue covers those pions already. The increase of a 6-layer tracking will be only 0.12%.

CHAPTER 1

PHYSICS MOTIVATION

The structure of the macroscopic observable matter is based on small structures with substructures like an atomic nucleus formed of protons and neutrons. These contents are again formed of smaller structures until at the smallest level there are the elementary particles. There are several possibilities for investigating the smallest structures made of elementary particles. Based on beam and target type and the used beam energy it is possible to investigate different physics phenomena. To investigate a certain kind of physics, like at Belle II the B physics, an experiment is designed to run most efficiently at the energy which we need to generate the desired states. In the following I introduce the SM of particle physics as the physics basis.

1.1. Introduction

The Standard Model of Particle Physics

The Standard Model (SM) of particle physics describes the elementary particles and the interactions between these particles: the weak interaction, the strong interaction and the electromagnetic interaction. Currently this theory together with gravity is the best verified way for describing all known particles and their interactions.

Quarks and Leptons

The fundamental particles in physics (figure 1.1) are particles without a substructure. We can characterize them by spin. All particles with spin $\frac{1}{2}$ are fermions and those with an integer spin are bosons. The fermions are the fundamental particles of the atomic nuclei stable matter (protons and neutrons) and we can characterize them again in two groups: the quarks and the leptons. Quarks are particles carrying color charge and experience strong interaction where gluons may cause a change of the color charge. Leptons do not carry color charge and do not interact via strong interaction.

Figure 1.1.: Overview about the fundamental particles in physics. On the left side quarks and leptons are arranged in their three generations. The gauge bosons, responsible for the different kinds of interactions, are in the orange column. According to [1][2]

Both kind of fermions respond to weak and electromagnetic interaction.

We can distinguish three generations of fermions. In the first generation are the quarks 'up' (u) and 'down' (d) and the leptons 'electron' (e^-) and 'electron-neutrino' (ν_e) which form the matter we can observe in our stabile world.

Bosons are additional to the fermions. Gauge bosons are responsible for the interactions and can carry different kind of charge. The four gauge bosons are the photon (γ) for the electromagnetic interaction, the gluons (g) for the strong interaction and the Z and $W^{\pm}$ for the weak interaction. I explain these interactions in detail later in this chapter. The additional Higgs boson with spin 0 does not mediate an interaction but is important to explain the mass of the standard model particles. cf. [1][3]

Hadrons are particles formed of multiple quarks, anti-quarks or gluons. Each of those quarks carries color and anti-quarks carry anti-color. Because of the confinement, we can only observe color-neutral particles and a required condition is to fulfill this confinement. With this it is not possible to observe a free quark. We call the combinations of three quarks baryons and we call a combination of one quark and one anti-quark mesons. I explain in the following chapters, baryons and mesons in more detail. For a simplification I include only the light quarks (u, d, s) in the following discussions. cf. [1][3]

As I mentioned before, baryons are three quark combinations and their spin is half-integer. In the stable world we can observe two kind of baryons: protons (uud) and neutrons (udd) which have a spin $\frac{1}{2}$.

Eight possible bound states exist for spin $\frac{1}{2}$ baryons and allowed strangeness. A combination of three identical flavored quarks in ground state is not possible because of its wave functions. For spin $\frac{1}{2}$ the spins are combined e.g. as ↑↑↓ which means that the spin wave functions are mixed symmetric. Therefore the flavor wave functions have to be mixed symmetric as well. A combination of three identical flavored quarks in ground state is not allowed because of the Pauli principle. Each baryon has four degrees of freedom (orbital, spin, flavor, color). In case of e.g. uuu, the flavor is the same, so the wave function is symmetric. In ground state the orbital wave function is also symmetric and for baryons the color is always anti-symmetric. For a together anti-symmetric wave function, the wave function of spin must be symmetric. At the baryon out of uds the isospin of the u and d quarks can couple to a triplet and a singlet which gives two states: the Σ^0 and the Λ. This results in eight states which form the baryon octet.

With spin $\frac{3}{2}$, it is possible to form baryons also out of three identical flavored quarks (e.g. Δ^-, Δ^{++} or Ω^-). This is possible because the three spins (e.g. ↑↑↑) are symmetric and therefore the flavor wave function can be symmetric as well which is the case for the uuu, ddd or sss states. In total it is possible to form ten different states. cf. [1][3] Mesons are states formed of one quark and one anti-quark. Because anti-quarks carry anti-color, it is possible to form a color neutral state with one color and its corresponding anti-color. The spin in such a state can couple to integer values. It is possible to form nine pseudo-scalar mesons out of the three light quarks while the quark anti-quark states with same flavor form mixing states. cf. [1][3] There are also three generations of leptons, in each of which there is one charged and one uncharged lepton. The charged leptons are electron (e), muon (μ) and tau (τ). The electron is involved at the macroscopic matter and neutrinos appear e.g. at the β-decay. cf. [1][3]

Interactions

We can trace all observed forces in physic back to four fundamental interactions;

- strong interaction

- electromagnetic interaction

- weak interaction

- gravity

Here I present the fundamental interactions in the order of their strength (see table 1.1). Because of their infinite range in macroscopic scale only electromagnetic interaction and gravity are observable. The electromagnetic content of macroscopic objects is based on the multiple particles carrying charge. The gravity is based on all particles carrying mass but can affect massless particles like photons by curved space-time. cf. [1][3]

Table 1.1.: The fundamental interactions and some of their characteristics. According to [1][3]

interaction	coupling on	strength	range	gauge bosons
strong	color charge	1	10^{-15} m	8 gluons (g)
electromagnetic	electric charge	$\frac{1}{137}$	∞	photons (γ)
weak	weak charge	10^{-5}	10^{-18} m	$W^{\pm}$, Z^{0}
gravity		10^{-38}	∞	

Electromagnetic Interaction

The electromagnetic interaction affects all charged particles (figure 1.2). The range of the electromagnetic interaction is infinite and the responsible gauge boson is the photon (γ).

Electromagnetic interactions always include photons. An annihilation of an electron positron pair produces photons carrying energy and momentum of the incoming particles. It is possible to annihilate an electron poision pair via a virtual photon and generate a muon anti-muon pair if the energy of the energy. cf. [1][3]
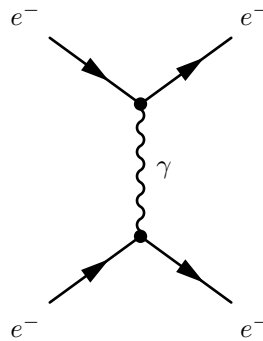
Figure 1.2.: Feynman diagram[1] for electromagnetic interaction between two electrons by exchanging one virtual photon. In this example the electrons change their momenta and directions because of scattering.

Weak Interaction

Compared to the strong interaction, the weak interaction affects beside hadrons also to leptons with Z^{0} and $W^{\pm}$ as gauge bosons.

At an interaction of a quark by emitting a virtual W boson, it changes the flavor as well as the charge (figure 1.3). Here the Cabibbo-Kobayashi-Maskawa (CKM) matrix (see following chapter for CKM matrix) is a transformation matrix where the absolute of its parameters describe the likelihood of the different flavor changes. Because of

---

[1] Feynman diagrams illustrate of the interaction between subatomic particles. They represent matrix elements for decays and scattering processes and simplify their calculation in quantum field theory.
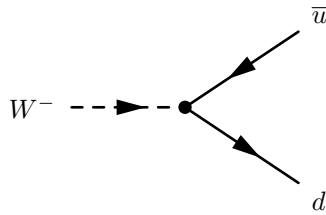
Figure 1.3.: Feynman diagram for weak interaction vertex. In this example the an virtual W^- creates by weak interaction a $\overline{u}\, d$ pair.

the charge ± 1 of the W boson, the charge of the quark has to change from $-\frac{1}{3}$ to $+\frac{2}{3}$ or vice versa.

For leptons the emission of a W boson changes a charged lepton to the corresponding neutrino. E.g. an electron to an uncharged electron-neutrino. This process preserves the lepton family.

At a neutral current interaction with exchange of a Z^0 boson, charge and flavor of all particles are preserved. A flavor changing neutral current is only possible with loop processes (see chapter 1.2.1) or processes beyond Standard Model.

At the weak interaction the number of baryons and leptons stays constant. This leads us to the conservation laws which I explain on page 20. A special case is the neutrino oscillation. In each interaction vertex also the family of a lepton is preserved, but because of the neutrino oscillation this family can change until a later point in time. cf. [1][3]

The Cabibbo-Kobayashi-Maskawa Quark Mixing Matrix
Before prediction or discovery of the third generation (b and t quarks) the quark mixing at weak interaction could be described with the 2×2 Cabibbo matrix. This matrix needs only one real parameter, the Cabibbo angle θ_c with $\sin \theta_c \approx 0.23$ and $\sin \theta_c \approx 0.95$. This description did not need a complex phase and could not explain CP violation (see chapter 1.2.2).

The Cabibbo-Kobayashi-Maskawa (CKM) matrix is an extension to three generations formulated by Nicola Cabibbo, Makoto Kobayashi and Toshihide Maskawa and describes the quark mixing in a similar way. Beside the three families, this matrix has also a complex phase which allows CP violation. In most cases a $W^\pm$ exchange causes a flavor change with preserving the quark generation. In detail this means, mostly an u changes to d described by $|V_{ud}| = 0.97427 \pm 0.00014$. Equivalent $|V_{cs}|$ for c to s and $|V_{tb}|$ for t to b. A smaller fraction changes the generation, so an s quark can change to a u ($|V_{us}| = 0.22536 \pm 0.00061$) by emitting a virtual W^+. For all combinations we need a unitary 3×3 matrix.

$$V_{\text{CKM}} = \begin{pmatrix} V_{ud} & V_{us} & V_{ub} \\ V_{cd} & V_{cs} & V_{cb} \\ V_{td} & V_{ts} & V_{tb} \end{pmatrix}$$

A description of the CKM matrix elements by mixing angles is much more complex
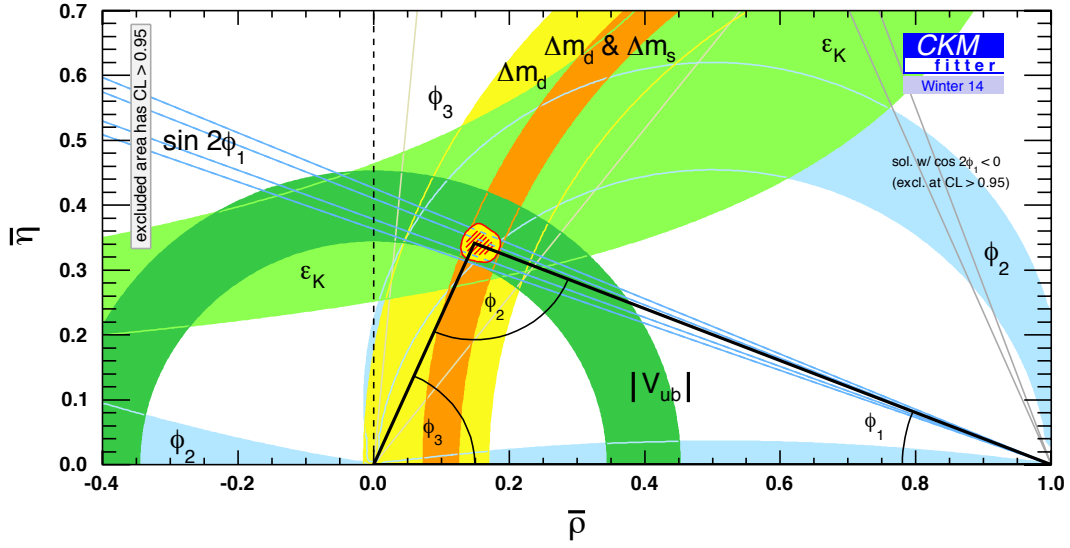
(a) State of the art unitarity triangle in 2014. The dimensions for the triangle are given by several experimental measurements. For instance the angles $\sin 2\phi_1$ (blue ■) are measured by $B \to \pi\pi, \rho\pi$ decays, ϕ_2 (light blue ■) by $B^0 \to J/\psi K_S^0, D^*\overline{D}^*$ decays and ϕ_3 (brown ■) by $B \to D^*\pi, DK, \pi K$ decays. The value $|V_{ub}|$ (green ■) can be adjusted by $B \to \tau\nu$.[9]
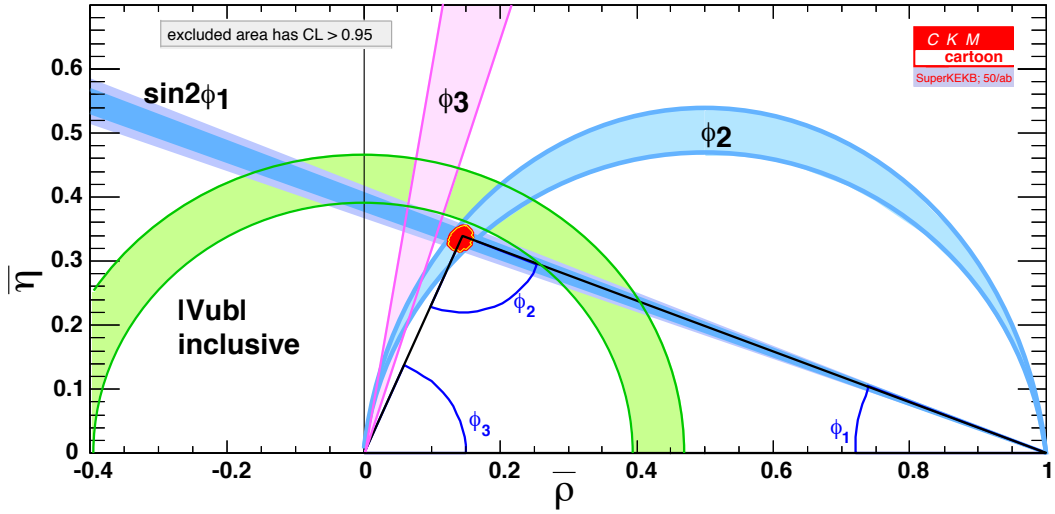
(b) Expected unitarity triangle with data of an integrated luminosity of $50\,\text{ab}^{-1}$ at SuperKEKB. Here is shown the expected ranges of $\sin 2\phi_1$ (blue ■), ϕ_2 (light blue ■), ϕ_3 (purple ■) and $|V_{ub}|$ (green ■)[10]

Figure 1.4.: The unitarity triangle with the apex given by the coordinate $(\overline{\rho}, \overline{\eta})$. Its sides are decided by $V_{cb}^* V_{cd}$ so the base base the length 1. The other two sides have the lengths $\frac{V_{ub}^* V_{ud}}{V_{cb}^* V_{cd}}$ and $\frac{V_{tb}^* V_{td}}{V_{cb}^* V_{cd}}$. On the left is shown the state of the art situation in comparison to the expected situation with SuperKEKB and Belle II on the right.

than it is for the 2×2 Cabibbo matrix. Here we need three real parameters and a complex phase to describe the elements. In an other notation we can write the matrix with the Wolfenstein parameters (cf. [2][11]) λ, A, ρ and η:

$$
V_{\text{CKM}} = \begin{pmatrix}
1 - \frac{\lambda^2}{2} & \lambda & A\lambda^3(\rho - i\eta) \\
-\lambda & 1 - \frac{\lambda^2}{2} & A\lambda^2 \\
A\lambda^3(1 - \rho - i\eta) & -A\lambda^2 & 1
\end{pmatrix}
$$

Where $V_{us} = \lambda$ and $C_{cb} = A\lambda^2$. To go to order λ^3 two new parameters (ρ and η) must be introduced. cf. [11] In this notation, the CP violation can be verified by measuring of the complex phase ($\rho - i\eta$).

Because of its unitarity, the sum of the transition probabilities from or to a certain quark must be 1, so the matrix covers all possible transitions.

The values of the CKM matrix describe three triangles in the complex space, the so-called unitarity triangles (see figure 1.4).

The CKM matrix is fundamental in the standard model and the knowledge about their precise value is important. The absolute values of the nine CKM matrix elements as they ares known so far are:

$$
V_{\text{CKM}} = \begin{pmatrix}
0.97427 \pm 0.00014 & 0.22536 \pm 0.00061 & 0.00355 \pm 0.00015 \\
0.22522 \pm 0.00061 & 0.97343 \pm 0.00015 & 0.0414 \pm 0.0012 \\
0.00886^{+0.00033}_{-0.00032} & 0.0405^{+0.0011}_{-0.0012} & 0.99914 \pm 0.00005
\end{pmatrix}
$$

To investigate the complex phase of the CKM matrix it is important to measure the difference in the decay time (Δt) of e.g. $\overline{B}^0$ and B^0 which needs a high precision in a Δz measurement. I describe this in more detail in chapter 1.2.2 about CP violation. For such a measurement with a high precision, it is needed to have high vertex resolution like it is provided by the Pixel Detector (PXD) (see chapter 2.3) of Belle II. cf. [3][1][12][2][45]

Strong Interaction

The strong interaction appears between all particles carrying color charge (figure 1.5). In baryons like protons and neutrons, the strong interaction binds the quarks based on the color charge of the quarks. The responsible gauge bosons in this interaction are the gluons.

All quarks carry color (r, g, b) and all anti-quarks carry anti-color ($\overline{r}$, $\overline{g}$, $\overline{b}$). While gluons change color of quarks, they carry one color and one anti-color. The composition of the eight possible basic states is dependent on the convention. With a rotation in the color space we can modify them. One possible choice of the eight basic states is (cf. [3]):

$$
r\overline{g} \; , \; r\overline{b} \; , \; g\overline{r} \; , \; g\overline{b} \; , \; b\overline{r} \; , \; b\overline{g} \; , \; \sqrt{\frac{1}{2}}\left(r\overline{r} - g\overline{g}\right) \; , \; \sqrt{\frac{1}{6}}\left(r\overline{r} + g\overline{g} - 2b\overline{b}\right)
$$
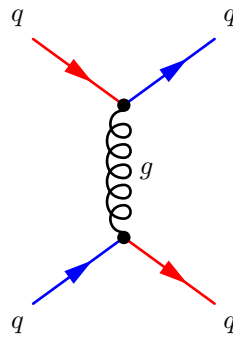
Figure 1.5.: Feynman diagram for strong interaction between two quarks by exchanging one gluon. Because a gluon carries color and anti color it exchanges the color of the two quarks.

Gluons interact with color charged particles and because of its own color charge, gluons are also able to interact with other gluons. This distinguishes them from photons, which cannot interact with other photons.

Because of this additional degrees of freedom, it would be possible that for each hadron exists a collection of particles which only differ by their total color charge. Due to the color confinement a color charged particle, such as quarks and gluons, cannot be observed singular. We can observe only color-neutral objects.

The term color-neutral is, analog to the colors of light, an addition of all three colors results to $r + g + b = color\text{-}neutral$ and for anti-colors $\bar{r} + \bar{g} + \bar{b} = color\text{-}neutral$. In quark anti-quark pairs the combination of color and anti-color also results in a color-neutral state (i.e. $r + \bar{r} = color\text{-}neutral$).

Additional to the mesons $|q\bar{q}\rangle$ or baryons $|qqq\rangle$ we could build also other quarks and anti-quark combinations. With the color confinement it is possible to form states out of four quarks $|qq\bar{q}\bar{q}\rangle$, a so-called tetraquark. First observation of a tetraquark candidate is the $X(3872)$ by the Belle cf. [4] and determined by cf. LHCb cf. [5]. An other candidate is the $Z_c(3900)$ found at the study of $e^+e^- \rightarrow \pi^+\pi^- J/\psi$. An alternative theory explains this state as a meson molecule cf. [6]. It was found by BES III cf. [7] and Belle cf. [8].

Conservation Laws

Conservation laws are important in physics. In the macroscopic world we know as conservation factors energy, momentum and angular momentum. Those do not change in each physical interaction. Also in particle physics those values are conserved. Additional to this, exist some conservation laws only for particle physics. Some are valid for all interactions and others are only valid in certain interactions. cf. [1][3]

The conservation of baryon number and lepton number exist as general conservation laws additional to the macroscopic ones.

Each baryon gets the baryon number $B = +1$ and each anti-baryon $B = -1$ while

non-baryon particles get $B = 0$. The baryon number before and after a reaction is the sum of baryon numbers of all particles involved in the reaction. Conservation of baryon number means, the sum of baryon numbers does not change before and after the reaction. As an example you can see the baryon numbers in the neutron decay:

$$
\begin{array}{ccccccccc}
 & n & \to & p & + & e^- & + & \overline{\nu_e} & \\
B: & 1 & = & 1 & + & 0 & + & 0 & \text{conserved}
\end{array}
$$

cf. [1][3]

Equivalent to the baryon number exist a lepton number L. For leptons (e, μ, τ and their neutrinos) it is $L = +1$ and for the anti-leptons $L = -1$. For non-leptons the value is $L = 0$. Additionally we can postulate a lepton family number for each family in the same way (L_e, L_μ and L_τ). In most reactions also this number is conserved and e.g. a muon cannot be transformed into an electron or vice versa. Because Neutrinos are not massless, it is possible to have neutrino oscillation in which only the lepton number L is conserved, but not the lepton family numbers.

$$
\begin{array}{ccccccccc}
 & \mu^- & \to & e^- & + & \overline{\nu_e} & + & \nu_\mu & \\
L: & 1 & = & 1 & + & -1 & + & 1 & \text{conserved} \\
L_e: & 0 & = & 1 & + & -1 & + & 0 & \text{conserved} \\
L_\mu: & 1 & = & 0 & + & 0 & + & 1 & \text{conserved}
\end{array}
$$

cf. [1][3]

There are also values which are conserved in some interactions, but not in all. There are e.g. strangeness, isospin or parity. Strangeness is the flavor quantum number which shows the amount of strange quarks in a particle. A strange quark (s) gives $S = -1$ and an anti-strange ($\overline{s}$) gives $S = +1$. The strangeness is conserved in electromagnetic and strong interaction but not in weak interaction. Therefore a particle with strangeness $S \neq 0$ like e.g. $K^\pm$ can decay only via weak interaction. cf. [1][3]

Equivalent to the strangeness we can form a quantum number based on the amount of charm quarks or the amount of bottom quarks. These are then called charmness and bottomness. They are also conserved by electromagnetic and strong interaction and need weak interaction to change. cf. [1][3]

Isospin is the flavor quantum number which is preserved only in the strong interaction. Similar to the classic Spin, the isospin for fermions has the numeric value of $\frac{1}{2}$, but has additional an orientation which results to the possible values of $I_3 = +\frac{1}{2}$ and $I_3 = -\frac{1}{2}$. For the quarks the up quark has isospin $+\frac{1}{2}$ and the down quark $-\frac{1}{2}$. All other quarks have the isospin 0 and anti particles have the inverse isospin. cf. [1][3]

An additional property of particles are the symmetries. The parity describes this characteristic. If the sign of the wave function changes after an inversion in space it has a negative parity. If the wave function is the same the parity is positive and otherwise it has a non good parity. This parity is preserved in strong and electromagnetic interaction.

The weak interactions can violate this parity. If we add a charge conjugation (replacement of all particles by its anti particles) we speak of the C-parity and we get a new conservation law, the CP-conservation. In most interactions which violate the parity, after a charge conjugation the CP-parity is preserved again.

1.2. Physics at Belle II

At Belle II some of the physics goals are the investigation of physics beyond Standard Model, CP violation and CPT violation, charmonium and bottomonium spectroscopy.

At Belle the charmonium and bottomonium spectroscopy (see chapter 1.2.3) was performed intensively. To enhance their precision and find some predicted but not yet observed states, this will be still a subject of interest at Belle II. But more and more the focus interest moves to the quarkonium like X, Y, Z states (see chapter 1.2.4).

As a main subject of interests the physics beyond Standard Model has the goal to answer questions which are not explained within the SM. Some of these phenomena I explain in chapter 1.2.1.

In the following I describe the physics basis behind these planned investigations.

1.2.1. Physics Beyond Standard Model

Belle II has its main interests not at the quarkonia, but mainly at new physics. The Standard Model of particle physics is the state of the art to describe the elementary particles and their interactions. It describes the most observed phenomena, but it cannot describe everything. For example it does not explain why there should be only three generations and the Standard Model has too many degrees of freedom. The mixing parameters and the masses of the bosons and fermions in the Standard Model are unknown and must be determined experimentally. There exist several suggested theories to solve this problem, like supersymmetric particles with masses in the order of TeV/c^2 or the existence of extra dimensions which most probably lead to new particles, generations and processes.

The matrix elements of the CKM matrix (see chapter 1.1) are only determined experimentally which means, that they are free parameters in the Standard Model. The number of degrees of freedom in the Standard Model should be as little as possible. For these parameters it should be possible to explain them over other theories which gives us a motivation for new physics beyond Standard Model.

Over the complex phase of the CKM matrix it is possible to find an explanation for the matter anti-matter asymmetry in the universe, but recently it looks like that this explanation is insufficient and asks for new theories.

To reach new physics beyond Standard Model several experiments search at the precision and energy frontier. At the energy frontier are searching e.g. the experiments ATLAS and CMS located at LHC at CERN. Here is also an experiment at the precision frontier, the LHCb. Other experiments in this field are e.g. BES III at
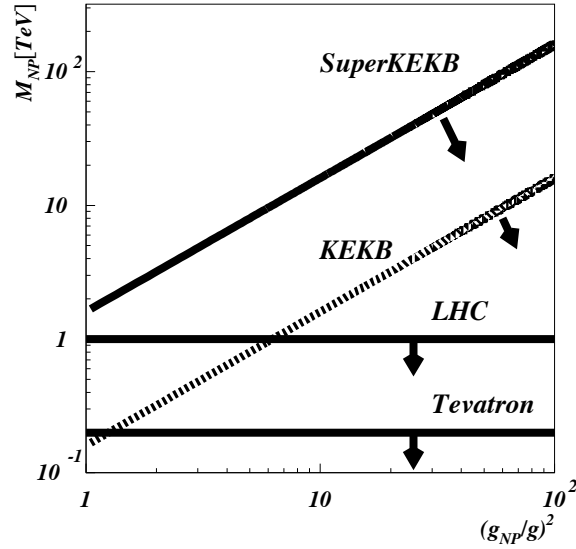
Figure 1.6.: Region of sensitivity for new physics as a function of the flavor violating couplings in the indirect searches at KEKB and SuperKEKB, and direct searches at LHC and Tevatron. [45]

BEPC II and Belle II at SuperKEKB. The energy frontier experiments at LHC using proton-proton collisions to find new particles with a mass range up to $1\,\mathrm{TeV}/c^2$. The sensitivity of the precision frontier experiments to new physics strongly depends on the strength of the flavor violating couplings in the new physics. Because of this, the mass range can be in best case in a range up to $100\,\mathrm{TeV}/c^2$ or in worst case still in a range up to $1\,\mathrm{TeV}/c^2$. The reach in searches for new physics is shown in figure 1.6. cf. [41][45]

Matter Anti-Matter Asymmetry

With the processes of Standard Model it is possible to motivate an asymmetry of matter anti-matter but not in the magnitude as in the content of the universe. To be able to generate this asymmetry Sakharov was postulating three rules: thermal imbalance, violation of the baryon number conservation (for baryon number conservation see page 20) and CP violation. The observed CP originates in the complex phase of the CKM matrix and, like already mentioned, is many orders of magnitude to small. This indicates that there must be other unknown sources for CP violation. Only by violating the baryon number it is possible to generate an asymmetric number of baryons and anti-baryons and this process violates also CP conservation. cf. [41][3][42][45]

Minimal Supersymmetric Standard Model (MSSM)

The Minimal Supersymmetric Standard Model (MSSM) is a minimal extension to the Standard Model based on supersymmetry. In this model all bosons and fermions have so-called supersymmetric partners from the other group. These supersymmetric partners have the same mass. Because the supersymmetric partners are also expected at masses below $1\,\mathrm{TeV}\,c^{-2}$ but were not observed yet, the supersymmetry must be broken. A problem in supersymmetry is, even with the minimal extension it needs > 100 parameters. cf. [41]

Penguin Processes

For known origin particles and resulting particles it is possible to describe this decay. The classical way is the so-called tree process. As an example figure 1.7(a) shows the Feynman diagram of the tree process for $B^0 \rightarrow \pi^+\pi^-$. Based on this, it is possible to calculate the branching fraction of this process. It was observed, that the real branching fraction of such decays deviates from the prediction explained by tree process. Because the total branching fraction of a decay is the sum of all possible ways from certain origin to resulting particles, other ways than tree processes have to be taken into account as well. One possibility for the example decay is the so-called penguin[2] process (figure 1.7(b)). In this process the incoming $\bar{b}$ is split into quark ($\bar{u}$, $\bar{c}$, $\bar{t}$) and W which form a loop and join to a $\bar{d}$. The quark can create a quark anti-quark pair via a virtual gluon.

(a) $B^0 \rightarrow \pi^+\pi^-$ in a tree process.   (b) $B^0 \rightarrow \pi^+\pi^-$ in a penguin process.
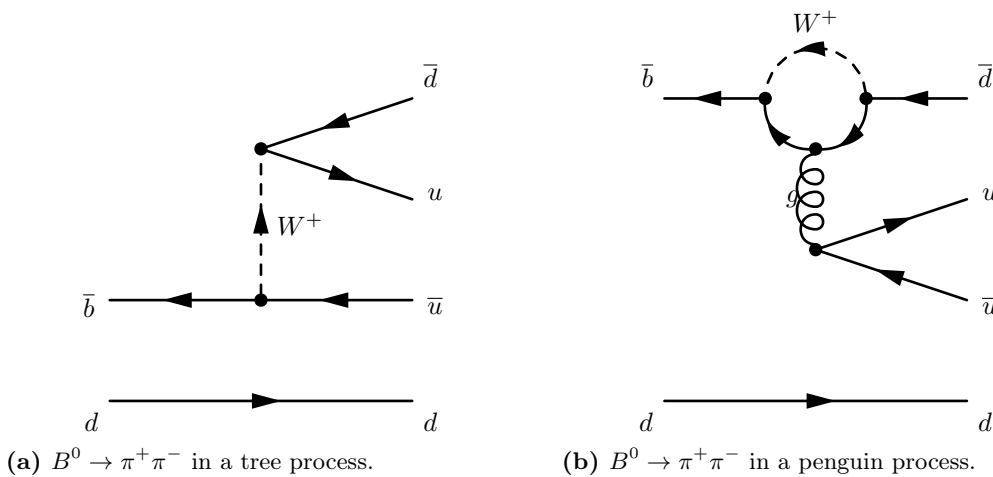
Figure 1.7.: Feynman diagrams for two different processes describing the decay $B^0 \rightarrow \pi^+\pi^-$.

---

[2] John Ellis was the first who published the penguin diagrams named because of their shape. As a second aspect he chose the name because of a lost bet, which said that he had to use the word penguin in his next publication.
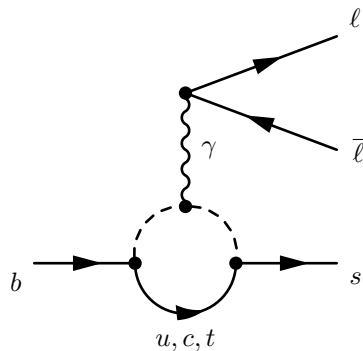
Figure 1.8.: Feynman diagram for penguin process of $b \to s\ell\bar{\ell}$. Based on the Standard Model, in this process the quark in the loop can be any positive charged quark (u, c, t).

There is also decays where the penguin process is the major part because a tree process is not possible. One example is the decay $b \to s\ell\bar{\ell}$ in figure 1.8. Based on the Standard Model we can use u, c or t for the quark in the loop. With this it is possible to calculate the branching fraction of this process. If there is a fourth generation of quarks, this quark line could also be one of those and the branching fraction of loop processes will be higher. Beside a fourth generation any other new particle, such as supersymmertic particles, could enhance the branching fraction as well. Measuring of the breaching fraction of penguin processes are promising candidates to find a new generation or indications for other unknown particles which would lead us to new physics. cf. [41][44]

Rare and Forbidden Decays

According to the Standard Model the Baryon and Lepton Number is conserved. Searches for lepton number violating processes (e.g. $\tau^- \to \mu^-\mu^+\mu^-$) or baryon number violating processes (e.g. $\tau^- \to \bar{p}\mu^+\mu^-$) are currently subject of research. In Standard Model exist charged lepton number violating processes with a branching fraction $< 10^{-40}$[43] (e.g. neutrino oszillation). With physics beyond Standard Model this value can increase and a baryon number violating will be possible. The mentioned decays are just some examples which makes the experiments sensitive for new physics searches at the precision frontier at Belle II. The chosen rare decays for those searches is strongly dependent on the experiment. The LHCb will be more precise at measurements for $B_s \to \mu^+\mu^-$, a flavor changing neutral current process. Belle II will reach a higher sensitivity on $B^0 \to K_S^0\pi^0\gamma$, a radiative quark tradition which can lead to a sizable CP violation. cf. [41][43][45]

1.2.2. CP Violation

As described in chapter 1.1 (section about conservation laws on page 21), the CP conservation is the conservation of the combination of C-parity and parity. In case of neutrinos we can observe a C-parity violation or a parity violation, because only lefthanded[3] neutrinos were observed and righthanded anti-neutrinos. If we look only at parity, we would change a lefthanded neutrino to a righthanded neutrino. In case of only C-parity it would change from a lefthanded neutrino to a lefthanded anti-neutrino. Both lead to particles which did not get observed yet. If we look at both parities, a lefthanded neutrino would change to a righthanded anti-neutrino, which describes the observations.

It was possible to observe decay products which do not fulfill the CP conservation. The first observed CP-violating decay was the decay of neutral kaons. More precisely the indirect CP violation was observed. The CP violation is most intense at a change between third and first generation quarks because their CKM parameter (V_{ub} and V_{td}) contain a complex phase. Therefore the B meson decays are an interesting subject to investigate CP violation. The first observation of CP violation with B mesons was at the decay $B \to K_S^0 J/\psi$ (see figure 1.9) [13][14]. In chapter 1.2.2 I describe in more detail the high ratio of kaons in B decays and the challenges in their measurement. In this decay are only transitions between third and second generation. B^0 mesons as well as $\overline{B}^0$ mesons can decay into $K_S^0 J/\psi$. Because of the B meson oscillation a B^0 meson can oscillate to a $\overline{B}^0$ and then decay into $K_S^0 J/\psi$. This describes a second channel with the same start and end product but here this decay contains the CKM matrix element V_{td} which has a complex phase already in lower order.

As a second aspect a CP violation is also possible without the oscillation because
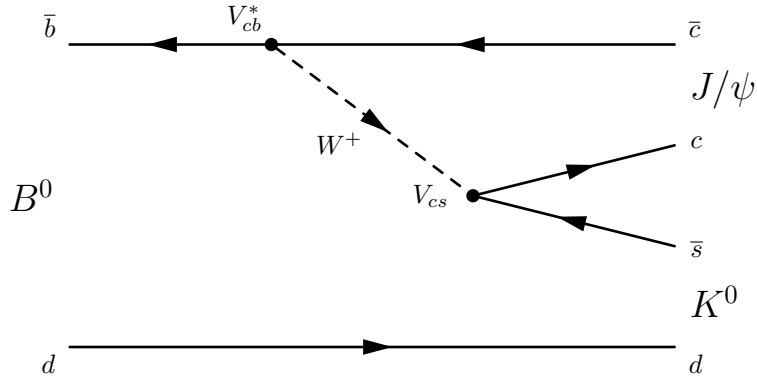
Figure 1.9.: Example decay for $B \to Kc\bar{c}$. In this case a B^0 decays into an K^0 and a charmonium state (e.g. J/ψ)

---

[3] In fraction of the spin in direction of the momentum is called helizity and defined as $h = \vec{I}(\vec{p}/|\vec{p}|)$ with the spin $\vec{I}$ and the momentum $\vec{p}$. In case that the spin points to the same direction as the momentum, the helizity is positive and we call the particle righthanded. For negative helizity we call it lefthanded cf. [3]

in higher order the Wolfenstein parametrization contains a complex phase also in the terms V_{cb} and V_{cs}.

To measure the CP violation in B decays, one of the B mesons gets reconstructed by its decay products. By identifying the flavor of the other meson this is then tagged as B^0 or $\overline{B}^0$ and additional the flight distance difference of the B mesons (see Δz in figure 1.10) is measured which is dependent on the time difference Δt. As shown in figure 1.11, the CP violation is recognizable as a difference between both curves. The amplitude of the difference of the two curves (figure 1.12) is proportional to $\sin{(2\beta\Delta t)}$ were β is one angle of the unitarity triangle (figure 1.4) and describes the position of the point (η, ρ) in the complex plane. In case of no CP violation the curves for B^0 and $\overline{B}^0$ mesons should be the same and then their difference is zero as in the Non-CP sample in figure 1.12(b). With this, β is a direct value to describe CP violation. cf. [1][3][11][13][14][15]

Many of the B decays contain kaons which are therefore an important issue for measuring CP violation. In the following I discuss the B decays and the observability
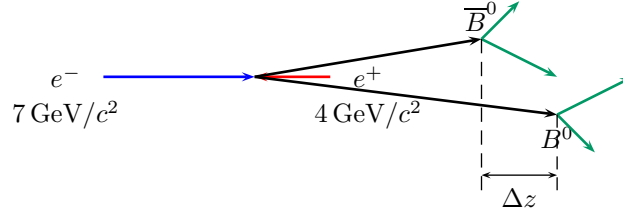

Figure 1.10.: CP violation measurement in B meson decay at Belle II. The asymmetric electron positron collision of $7\,\text{GeV}/c^2$ and $4\,\text{GeV}/c^2$ causes a boost for the two B mesons. A difference in their decay time (Δt) causes also a Δz of the decay vertex.
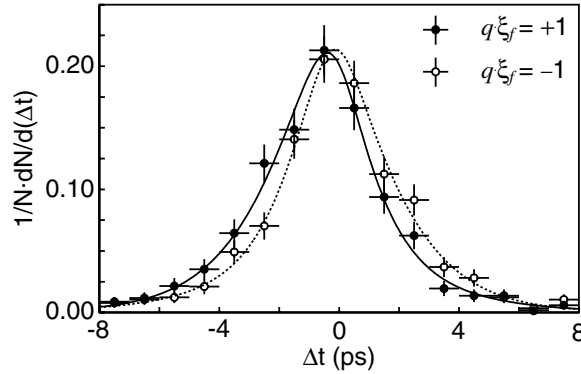
Figure 1.11.: Δt distributions for B decays. The $\overline{B}^0$ mesons are shown as $q\xi_f = +1$ (solid points and fit as solid line) and the B^0 mesons as $q\xi_f = -1$ (open points and fit as dashed line). [14]

of the kaons more precisely.

(a) Kaon oscillation with W exchange.   (b) Kaon oscillation with quark exchange.
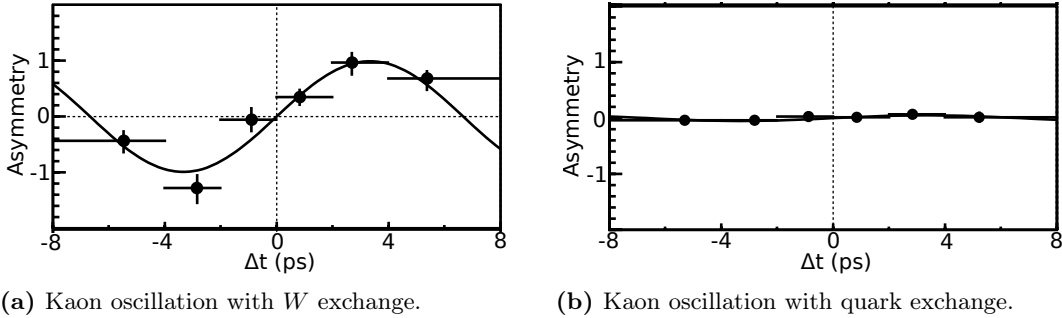
Figure 1.12.: Amplitude of the $B^0\,\overline{B}^0$ asymmetry. In (a) we see the result of the full data sample. In (b) is shown the corresponding plot for Non-CP control samples. [14]

Kaons in B Decays

At Belle II the experiment is running on energies where the probability to produce $B\overline{B}$ pairs is very high. At the decay of B mesons the decay channel $B \to Kc\overline{c}$ is dominant. This is the case because for the b quark the most dominant process with flavor change by emitting an W is from b to c. The CKM matrix elements show that $|V_{cb}| > |V_{ub}|$ and therefore the cb process is one of the dominant. The W can produce a quark anti-quark pair where the cs production is dominant while $|V_{cs}|$ is a diagonal element. In figure 1.9 is shown a Feynman diagram for such a decay.

To investigate the K_S^0 and its decays is important for the studies about CP-violation (chapter 1.2.2). The K_S^0 decay almost only into two pions which can carry asymmetric momentums due to the fact that the kaon has some momentum. Additional to this asymmetry in the momentum comes the phenomena of secondary vertex. In general all particles generate a secondary vertex at their decay point compared to the place where they are produced. This is the case because of a lifetime larger than 0. In case of short-lived particles like B or D, this offset is very small. In case of a particle which is able to fly in r direction for several centimeters before it decays, this displaced vertex can cause that we get problems with the detector acceptance (an illustration for a secondary vertex event is shown in figure 5.7 in chapter 5.3.2 about the secondary vertex problem). To be able to make accurate studies on these phenomena it is important to register all of the decay products. Also particles with hits only very close to the interaction point are interesting. Without them, a part of the decay would be missing, and a reconstruction of the kaon is not possible anymore. In chapter I made 5.4 an analysis on the possibilities of measuring pions from K_S^0 in the Vertex Detector system of Belle II.

1.2.3. Quarkonium Spectroscopy

Already at Belle and still at Belle II quarkonium states are a subject of investigations. Quarkonia are flavorless mesons by combining a quark and its anti-quark. For pseudo-scalar mesons out of lighter quarks (u, d, s) they form mixed states like π^0 ($\frac{1}{\sqrt{2}}\left(u\overline{u} - d\overline{d}\right)$) and cannot be distinguished in exact $u\overline{u}$ or $d\overline{d}$ states. For the more heavy quarks like charm or bottom it is possible to form well-defined quarkonium states. We call mesons formed of charm quarks charmonia and its most prominent representative is the J/ψ. With bottom quarks it is possible to form e.g. different Υ states called bottomonium. Solving the non relativistic Schrödinger equations including a potential description of the QCD $V(r)$, we can calculate their masses.

$$V(r) = \frac{-4\alpha_s}{3r} + kr$$

Here α_s is the strong coupling constant and k covers the confinement. This is a simplified potential. For a more accurate description one has to take into account some additional terms for fine structure splitting, hyperfine structure splitting and tensor corrections. With this theory the predicted states match quite well (see figures 1.13 and 1.14).

In the past it was already an important subject at Belle to search for new states of this group and investigate their properties. This will still be the case in the future as long as there are many states with a lot of unknown characteristics. cf. [1][16][17]

Charmonium

Charmonia are in a mass region of about $2.9\,\mathrm{GeV}/c^2$ to about $4.5\,\mathrm{GeV}/c^2$ [2] and the first observed charmonium state was the J/ψ. With its observation was confirmed, that there exists a fourth quark type beside the already known u, d and s at this time. This state does not mix with the other quarkonium states because their mass is much higher and the width is very narrow. Like many other states, also charmonium states are not observable directly. They have to be reconstructed by their decay products. The first charmonium (J/ψ) was generated in parallel by $p\mathrm{Be} \rightarrow e^+e^- x$ directly with $e^+e^- \rightarrow$ hadrons. Because of this, only $J^{PC} = 1^{--}$ states like J/ψ were possible. We can generate other states over e.g. two-photon production, initial state radiation or B decays. Because of huge data samples, we can find also rare states with this method. An overview of observed and predicted charmonium states is shown in figure 1.13. cf. [1][16]
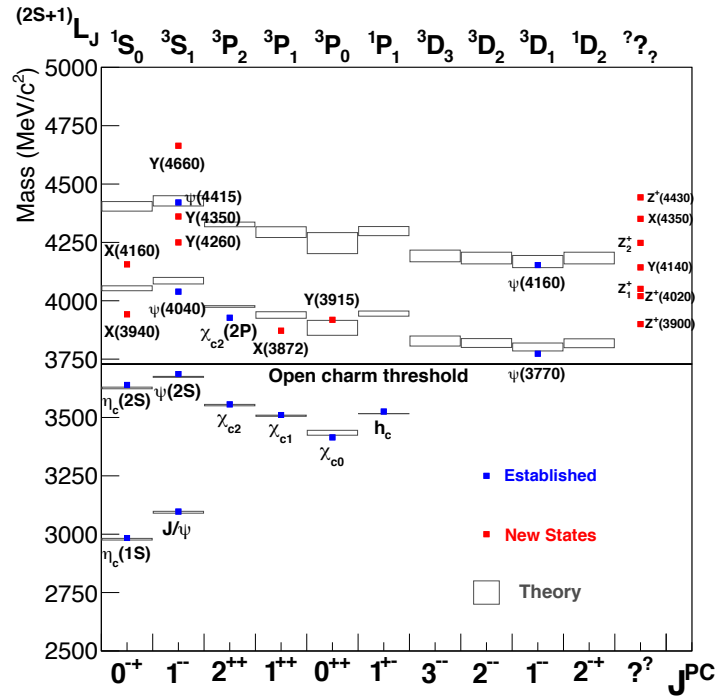
Figure 1.13.: The Charmonium energy levels as known so far. The blue ■ states agree with the theory while the red ■ states describe new states which not agree with the theory or the properties are not exactly measured yet. At the open charm threshold the energy is high enough to produce a $D\overline{D}$ pair. [16]

Bottomonium

The bottomonium mass region is above $9\,\mathrm{GeV}/c^2$ [2]. The 1^{--} state with then smallest mass ($\Upsilon(1S)$) was the first observed member. Like the charmonium, also the bottomonium do not mix with other quarkonium states. It is possible to produce those states directly in a e^+e^- annihilation as long as $J^{PC} = 1^{--}$ like it is for the Υ states. By radiative transitions also other states can be produced. Equivalent to the charmonium, an overview of observed and predicted bottomonium states is shown in figure 1.14. cf. [1][16]
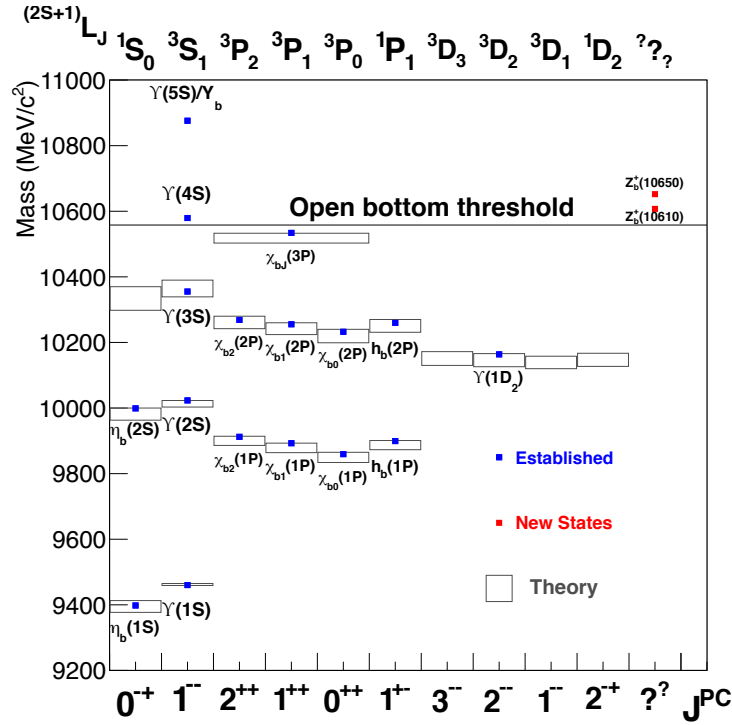
Figure 1.14.: The bottomonium energy levels as known so far. The blue ■ states agree with the theory while the red ■ states describe new states which not agree with the theory or the properties are not exactly measured yet. At the open bottom threshold the energy is enough to produce a $B\overline{B}$ pair. [16]

1.2.4. Quarkonium-Like X, Y, Z States

Like discussed before, there exist the heavy quarkonium states called charmonium (e.g. η_c, J/ψ[4], ψ', h_c, χ_{c0}) and bottomonium (e.g. η_b, Υ, h_b, χ_{b0}). Additional there are new observed states, which are charmonium-like but do not fit to the general scheme of $c\overline{c}$ mesons, the X, Y and Z states. States called X or Y are uncharged (states called Y have the quantum numbers 1^{--}, for all other quantum numbers they are called X) while Z states carry electrical charge. Reasons why they do not fit into the general naming scheme is, that some of them are charged and that their mass does not fit to the predicted charmonium states. Concepts to explain some of those charged and uncharged states are tetraquark or bound states of two mesons (meson molecules).

---

[4] the $\psi(1S)$ state is called J/ψ because of historical reasons. It was first observed in parallel by SLAC and BNL. To name the particle, the group around Burton Richter from SLAC decided to use the unused greek letter ψ. In parallel Samuel Chao Chung Ting from BNL named it as J as his family name is written in Chinese as 丁, which looks very similar to a J. To take both discoverers into account, it was named J/ψ from this point. [18][19]

The first discovered exotic state was the $X(3872)$ by Belle [4] and the first Y state was $Y(4260)$ by BaBar [20]. As a first charged exotic state BES III observed the $Z_c(3900)^{\pm}$ [7]. In the following I describe these three states as examples for X, Y, Z states in detail. cf. [21][2][22][23]

The $X(3872)$ state

The first discovery of $X(3872)$ was at Belle [4] in year 2003, while the first indications were found 1993 at E705 spectrometer at Fermilab [24]. The discovery got confirmed by several experiments like Babar [25], CDF II [26][27][28], DØ [29], LHCb [30] and CMS [31][32]. The mass of the $X(3872)$ is measured very precisely to $3871.69 \pm 0.17 \, \text{MeV}/c^2$ [2].

The decay with the highest branching fraction is $X(3872) \rightarrow \pi^+\pi^-$, but beside this exist the very important decay $X(3872) \rightarrow J/\psi\gamma$. With this decay it was possible to get the quantum numbers of 1^{++} [5]. Because of the mass region and the electromagnetic decay and that the decay products contain only a $c\bar{c}$ state, we can conclude that $X(3872)$ is most likely a charmonium-like state. As quantum numbers of the $X(3872)$ are 1^{++} and if we look at the charmonium spectrum (figure 1.13) we can see that its mass is to far away from the predicted region of the χ_{c1} state.

Due to the fact that the $X(3872)$ mass is very close to the $D^{0*}\overline{D}^0$ threshold of $3871.84 \pm 0.28 \, \text{MeV}/c^2$ [2] there were discussions if it is a bound state of a D^{*0} with a $\overline{D}^0$ with gluon binding equivalent to the deuteron. Another theory explains this state as a tetraquark cf. [33]. A bound state of four quarks without a meson-molecule structure. Most likely the quark content contains a charm anti-charm pair and an light quark pair but the exact quark content is not known yet. This state is not well understood yet and therefore an important object of future research at experiments like Belle II or BES III. cf. [2][22][33]

The $Y(4260)$ state

The state $Y(4260)$ was first discovered in 2005 by BaBar [20] and confirmed at other experiments like Belle [34][8] and CLEO [35]. Due to the fact that it was observed in the initial state radiation process $e^+e^- \rightarrow \gamma_{\text{ISR}}\pi^+\pi^-J/\psi$ it follows that this state is a 1^{--} state and therefore an Y. At a closer look to production processes via initial state radiation ($e^+e^- \rightarrow \gamma_{\text{ISR}}Y$) there were observed three more states ($Y(4008)$, $Y(4250)$ and $Y(4660)$ [34][36][37][38]) and because of the initial state radiation process, all of them have the quantum numbers 1^{--}. As the Y states are 1^{--}, they are in the area of ψ mesons, but if we check the charmonium spectrum (figure 1.13) we see that there are more states observed than there exist predictions for ψ mesons. So far there is no explanation for the Y state masses. One discussed theory for the $Y(4260)$ is a hybrid state of a charmonium with a gluon $c\bar{c}g$ [39] but also tetra quark states are a possible concept.

The charged $Z_c(3900)^\pm$ state

The first observation of the charged $Z_c(3900)^\pm$ state was 2013 at BES III [7]. Short after is first observation it got confirmed by Belle [8]. Its observation was through the production channel $Y(4260) \rightarrow Z_c(3900)^\pm \pi^\mp$ and a reconstructed decay into $Z_c(3900)^\pm \rightarrow J/\psi \pi^\pm$. With a mass of $3888.7 \pm 3.4 \,\text{MeV}/c^2$ [2] it is in the range of charmonium states but quarkonium states always have to be uncharged. Therefore it is not possible to explain this state as a pure $c\bar{c}$ combination. Theories to explain this state are, that it could be a combination of four quarks because here the two light quarks could add charge to the charmonium-like system. Similar to the $X(3872)$ it is close to the $D^\pm \overline{D}^{0*}$ threshold and can be explained as a molecule state of $D^\pm$ and $\overline{D}^{0*}$. Additional exist the theory of a tetra quark with e.g. $c\bar{c}u\bar{d}$. An angular analysis favors quantum numbers of 1^+ [40][2]. Because of its exotic characteristics of being in the charmonium like region and being charged at the same time it is a very interesting subject for future investigations.

Low Momentum Pions from D^{*-} in $Z_c(3900)^-$ Decays

Figure 1.15.: A decay channel of $Z_c(3900)^-$. In this chosen channel an D^{*-} decays in $\overline{D}^0$ and a low momentum π^- (red ■).

Like mentioned before, it is not exactly known what kind of particle the $Z_c(3900)^\pm$ is. But so far it is known, that it looks like a four quark state cf. [8][7]. It is yet unknown how the four quarks are bound in the system. Two possibilities are a tetraquark or a meson molecule. Further studies on this state shall clarify this question.

To investigate the $Z_c(3900)$ it is important to check all its decays. In case of the decay shown in figure 1.15 it is possible to have a low momentum pion. In this decay the mass difference at the $Z_c(3900)$ decay into $D^{*-} D^0$ is only about $25 \,\text{MeV}/c^2$ and at the D^{*-} decay into $\overline{D}^0 \pi^-$ is even smaller at only about $6 \,\text{MeV}/c^2$. At a production at Belle II over an $\Upsilon(4S)$ and B decay this will lead to a very small momentum for the pion. To register and investigate this decay channel, we have to measure the pion, otherwise it would be lost. To be able to detect also pions which reach only the inner layers of the Belle II detector a new concept of 6-layer tracking was drafted. In chapter 5.3.4 I give a description of this concept and an examination about possibilities to detect this $Z_c(3900)$ decay in a B decay I show in chapter 5.5.

CHAPTER 2

EXPERIMENTAL SETUP

At the KEK (japanese: 高エネルギー加速器研究機構 kō-enerugī kasokuki kenkyū kikō, english: High Energy Accelerator Research Organization) will run a ring accelerator for electrons and positrons, the SuperKEKB (see figure 2.1). The SuperKEKB is the recent upgrade of the KEKB accelerator with asymmetric beam energies of $7 \, \text{GeV}/c^2$ for electrons and $4 \, \text{GeV}/c^2$ for positrons. With these energies it is constructed to be an asymmetric B-factory. In the recent upgrade the luminosity[5] will be increased by a factor of 40 to the previous experiment and will lead to $L = 8 \cdot 10^{35} \, \text{cm}^{-2} \, \text{s}^{-1}$. cf. [45]

2.1. The Belle II Detector Overview

The collider experiment Belle II (figure 2.2) will be placed at the SuperKEKB accelerator ring and is an upgrade of the Belle experiment. This experiment is designed to specifically investigate B decays and CP violation in those decays. In the following I will introduce the main components of the future Belle II experiment. cf. [45]

Pixel Detector (PXD) and Silicon Vertex Detector (SVD)
As the innermost detector will be a silicon pixel detector. It will be installed with a distance of only 1.5 mm around the beam pipe and it consists of two layers. It is a key component for the vertexing in the detector upgrade. I will describe the PXD more detailed in chapter 2.3. Around the PXD will be a silicon strip detector called Silicon Vertex Detector (SVD) (chapter 2.2). The combination of these two detectors is called Vertex Detector (VXD). cf. [45]

---

[5] Luminosity describes the amount of events with the accelerator beam per time and interaction cross-section. It is a value to characterize the performance of an accelerator. The luminosity of KEKB was $L = 2.11 \cdot 10^{34} \, \text{cm}^{-2} \, \text{s}^{-1}$ and is so far the highest luminosity for an electron positron collider.
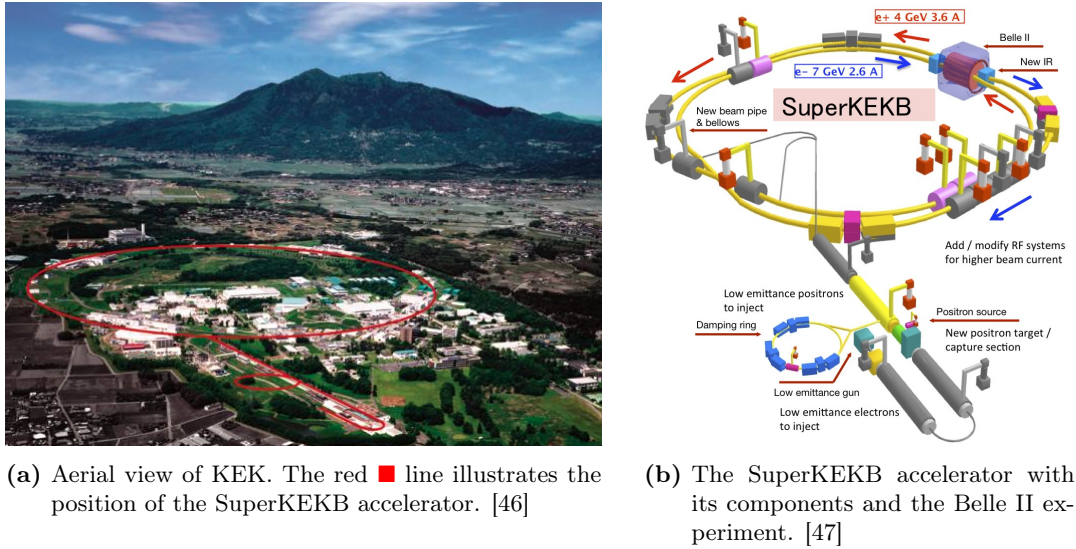
(a) Aerial view of KEK. The red ■ line illustrates the position of the SuperKEKB accelerator. [46]

(b) The SuperKEKB accelerator with its components and the Belle II experiment. [47]

Figure 2.1.: The SuperKEKB accelerator at KEK in Tsukuba, Japan.

Central Drift Chamber (CDC)

The Central Drift Chamber (CDC) of Belle II is based on the CDC used in Belle. The major changes in the design are the dimensions. In Belle the CDC had radii of 77 mm (inner cylinder) to 880 mm (outer cylinder). The upgrade at Belle II increased in size to 160 mm (inner cylinder) to 1130 mm (outer cylinder).

With this detector it is possible to reconstruct tracks of charged particles and measure their momenta. Additionally it is possible to measure the energy loss in the gas volume of the CDC and provide a particle identification for particles which do not reach the detectors around the CDC. cf. [45]

Čerenkov Detectors

In the Barrel part the Čerenkov detector consists of Time of Propagation (TOP) counters using 16 quartz plates surrounding the CDC. Charged particles passing though the quartz plates produce Čerenkov photons[6] which propagate to the end of the plate over total internal reflection. These photons are detected with photo detectors placed at the end of each plate. With this detector it is possible to measure the velocity of particles and perform a particle identification.

In the end-cap region is used an Aerogel Ring-Imaging Čerenkov detector (ARICH) which is able to separate kaons and pions at a wide momenta region. cf. [45]

---

[6] Charged particles passing though matter with a velocity higher than the speed at which light propagates in this matter emit Čerenkov radiation (named by its discoverer Pavel Alexeevič Čerenkov; russian: Па́вел Алексе́евич Черенко́в). cf. [3]
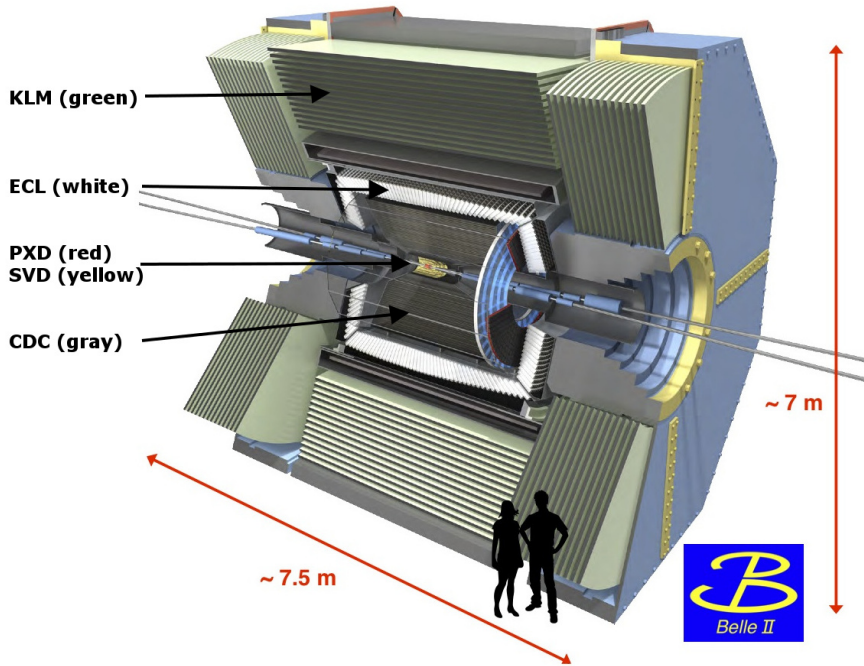
Figure 2.2.: CAD image of the future Belle II detector with the Pixel Detector (PXD) (red ■) and the Silicon Vertex Detector (SVD) (yellow ■) as the two innermost detectors. Surrounded by the Central Drift Chamber (CDC) (gray ■), Electromagnetic Calorimeter (ECL) (white ■) and the K_L^0 and μ detection (KLM) (green ■). According to [47]

Electromagnetic Calorimeter (ECL)

From the interaction point to Čerenkov detectors only charged particles can be detected. To be able to detect also neutral particles the Electromagnetic Calorimeter (ECL) is used. Particles like e.g. photons create an electromagnetic shower of electrons and photons. Here thallium doped cesium iodide crystals are chosen as scintillators with the advantages of a high light output and short radiation length. In these crystals particles like π^0 create photons which produce then electromagnetic showers and generate scintillation light. This light gets detected with a photomultiplier. cf. [45]

K_L^0 and μ detection (KLM)

As a last component the K_L^0 and μ detection (KLM), a hadronic calorimeter, detects uncharged particles which did not interact with the ECL. Here particles are detected which interact over strong interaction. It consist of 14 layers of iron and in between are sensitive detector layers. The iron plates in between are used to have interaction of the particles with the material. This interaction creates e.g. photons and electrons. In the sensitive layers the produced photons and electrons are detected over their

scintillation light. With this setup is possible to detect hadronic particles. cf. [45]

2.2. Silicon Vertex Detector (SVD)

A silicon strip detector will be used as the second inner detector (figure 2.3). This consist of 4 double-sided layers with radii of 38 mm to 140 mm and an angular acceptance of 17° forward to 150° backward. For the outer three layers the forward end is tilted to the beam pipe. Together with the PXD these two detectors form the Vertex Detector (VXD) and provide a high vertex resolution of up to 25 μm in beam direction.

The design of SVD is optimized for a low background, high precision measurement together with a high radiation hardness. With the high precision and together with the PXD (chapter 2.3) this system has the ability to reconstruct decay vertices of short lived particles with a very high precision. We need this high precision to reconstruct the decay vertices of e.g. B mesons. With these results, it is possible to measure the CP-violation (see chapter 1.2.2) in B mesons. Additionally it will be possible to improve the corresponding measurements for CP-violation at K_S^0 mesons. cf. [45]
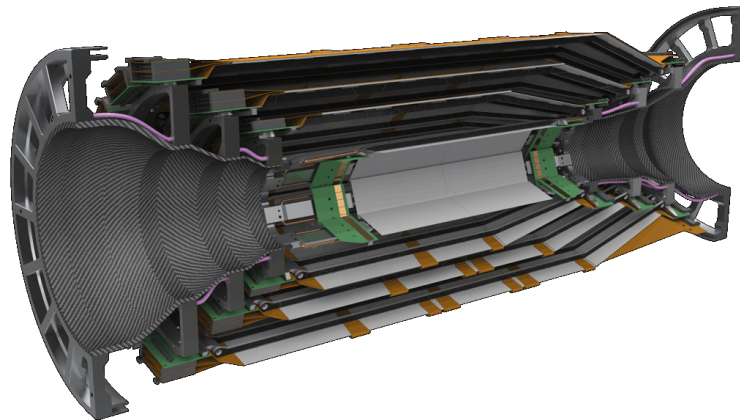
Figure 2.3.: A lengthwise cut through the SVD detector. One can see the barrel shaped innermost SVD layer, and the outer three layers with a tilted sensor at the front end. [48]

2.3. Pixel Detector (PXD)

As the innermost detector, a silicon pixel detector will be used (figure 2.4). It consists of two active layers. The inner layer has a radius of 14 mm and a sensitive length of 90 mm, the outer a radius of 22 mm and a length of 123 mm. The sensitive length of both layers cover an angular acceptance similar to SVD (17° forward to 150° backward).
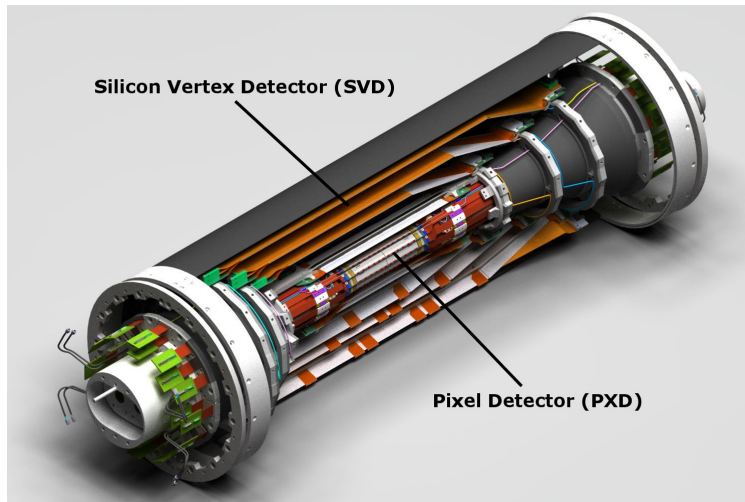
Figure 2.4.: The Vertex Detector (VXD) are the system formed by Pixel Detector (PXD) and Silicon Vertex Detector (SVD) (chapter 2.2). One can see the PXD as the innermost barrel shaped component. According to [49]

As sensor is used a DEPFET (DEPleted Field Effect Transistor, chapter 2.3.1) matrix with pixel size of $50 \times 55 - 60\,\mu\text{m}^2$ (inner layer) and $50 \times 70 - 85\,\mu\text{m}^2$ (outer layer) and a pixel number of 250×768. Multiple ASICs will read out these pixel in rolling shutter mode. The currents from the DEPFET pixels get digitized and send to the next chip, the Data Handling Processor, for further data acquisition. (see chapter 2.5) cf. [45]

2.3.1. Depleted Field Effect Transistor Principles

A DEPFET (DEPleted Field Effect Transistor) is a detector based on semiconductor and is a special version of a field effect transistor. It consists of two parts. A fully depleted silicon substrate which forms the particle detector and a field effect transistor onto the substrate which does a first preampfification of the detected signals.

If a particle passes the detector substrate, it generates electron-hole pairs like in a regular semiconductor based detector. The so generated free electrons get collected in the internal gate right under the FET while the positive charged holes drift to the negative charged back contact (figure 2.5).

For a measurement the FET will be switched on. Because the channel current is dependent on the charge of the internal gate, the charge collected in the internal gate can be determined by measuring the current. This process can be repeated without deleting or changing the charge in the internal gate.

To reset the internal gate, an additional FET providing a clear gate will be used. This a positive voltage generates a connection between the clear gate and the internal gate and through this connection the internal gate will be discharged. cf. [45][50]
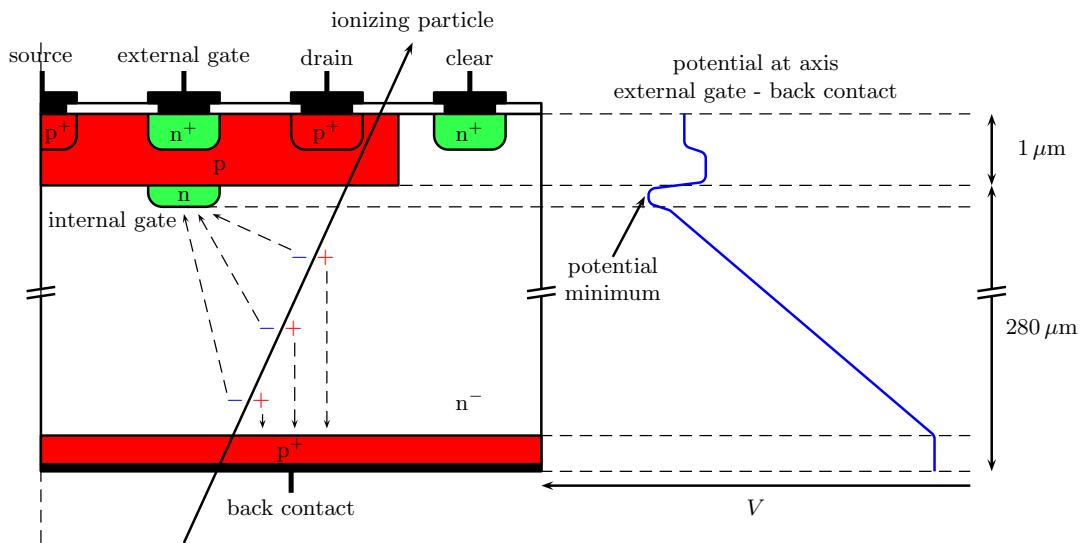
Figure 2.5.: Cut through a DEPFET detector with its potential gradient. One can see a potential minimum at the internal gate caused by the collected electrons generated by an ionizing particle. Its magnitude depends on the amount of electron hole pairs generated by this passing particle. After a reset through the clear gate, this minimum is less distinctive. According to [51]

2.4. Sources of Background in the PXD

We expect to have several effects which generate additional hits from background effects beside the physics indicated hits. Possible effects are synchrotron radiation, scattering of the beam on residual gas, Touschek scattering, radiative Bhabha scattering and electron-positron pair production.

• 2.4.1. Synchrotron Radiation

When a charged particle changes direction, synchrotron radiation is emitted tangential which hits the outside wall of the accelerator ring (figure 2.6). But the last direction change before the beam leads to the interaction region and can emit synchrotron radiation into the beam pipe and close to it and can hit detector components. Because of its character of a hard radiation there is a risk of damage if it hits the detector, so the interaction region is designed to minimize this effect in the detectors. cf. [45]
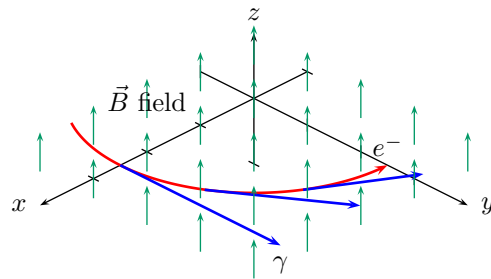
Figure 2.6.: Synchrotron radiation (blue ■) is emitted tangential from a curved track of charged particles (red ■) in a magnetic field (green ■).

- ## 2.4.2. Scattering of the Beam on Residual Gas

  The scattering of the beam on residual gas is a combination of bremsstrahlung and Coulomb scattering of beam particles with the residual gas. Induced of this processes the momentum of beam particles decreases and changes direction. As a result of the direction change the particles hit the beam pipe and create showers which are shown in the detector as one of the main background effects. cf. [45]

- ## 2.4.3. Touschek Scattering

  Similar to the scattering of beam particles on residual gas, the beam particles can scatter on other beam particles. Also here the momenta change value and direction and hit the beam pipe. The created showers are an other major background effect (see figure 2.7). cf. [45]
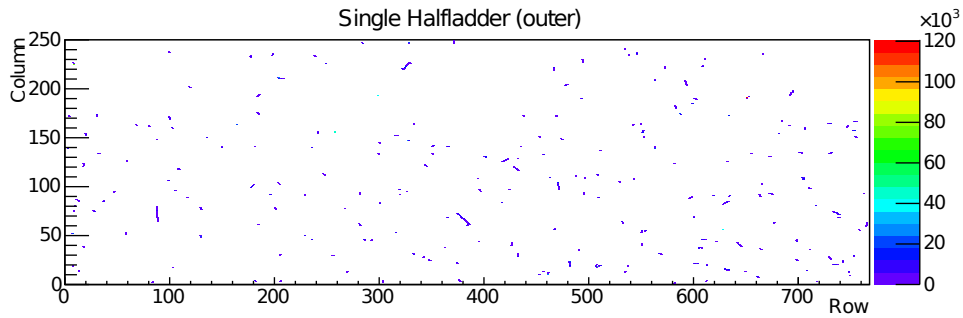
(a) Touschek scattering hit on outer PXD layer.
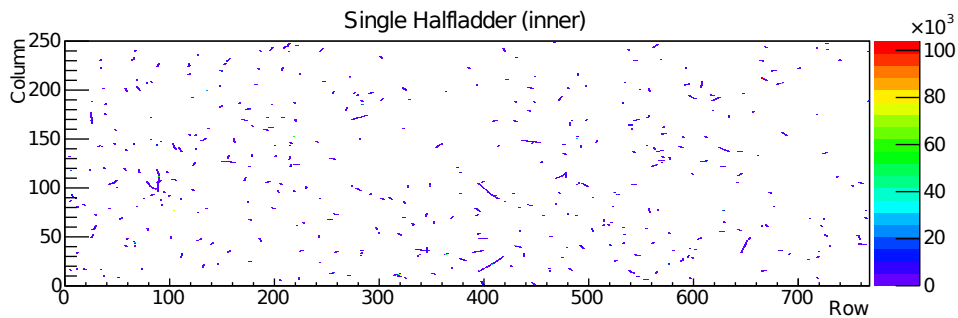
(b) Touschek scattering hit on inner PXD layer.

Figure 2.7.: Simulated hits from Touschek scattering on PXD detector ladders. As one can see, the occupancy from Touschek effect on the inner layer is much higher than on the outer layer. [52]

- ## 2.4.4. Radiative Bhabha Scattering

    During the electron positron scattering ($e^+e^- \rightarrow e^+e^-\gamma$; see figure 2.8) both particles (electron and positron) lose energy. Because those particles have less energy than the unscattered beam particles, they will get redirected out of the beam line at the next beam magnet. In the interaction region the beam lines are almost straight and in the center of the solenoid which minimizes this effect and it is only a minor part of the background. cf. [45]
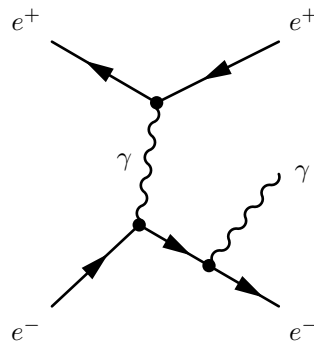
Figure 2.8.: Feynman diagram for radiative Bhabha scattering.

• 2.4.5. Electron-Positron Pair Production

It is also possible to produce electron positron pairs ($e^+e^- \rightarrow e^+e^-e^+e^-$). Because these new particles have a relatively low momentum, they mostly reach only detector parts very close to the interaction region. In the design of Belle II the inner layer of the PXD is only $14\,\mathrm{mm}$ around the beam, so it is important to include this effect to the background studies. cf. [45]
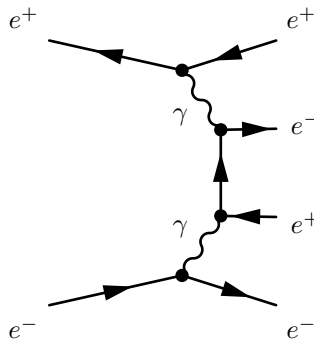
Figure 2.9.: Feynman diagram for electron positron pair production generated by electron positron pair with high energy.

Induced by these background effects it is expected having an occupancy of 3% on the inner PXD layer and still 1% on the outer PXD layer. With 250×768 pixel per sensor and 40 sensors in the PXD we have to read out about 8 million pixel and after a zero suppression processed in the PXD readout (see chapter 2.5.1) we expect a total data rate of up to $20\,\mathrm{GB/s}$. To be able to handle this data rate on the event builder and data storage a data reduction is needed. cf. [45]

2.5. Data Acquisition (DAQ)

In figure 2.10 you can see an overview of the data acquisition at Belle II. In this chapter you will find a detailed description of its components like PXD readout, ROI sources (High Level Trigger (HLT) and Data Acquisition Tracking Concentrator Online Node (DATCON)) and the data reduction system called Online Selection Nodes (ONSEN) system which performs a Region of Interests selection.

Additional the outer detectors will deliver data to the Event Builder 1 from where the High Level Trigger (HLT) will receive its data to perform a Region of Interests calculation (see chapter 2.5.2). The Event Builder 2 at the end of the DAQ chain receives the reduced data from the ONSEN (see chapter 3) and the HLT to forward them to the storage. [53]

2.5.1. PXD Read-Out

The PXD data which got digitized by some ASICs right beside the sensor (see chapter 2.3) get read out by four Data Handling Processor (DHP) which also process a zero suppression. All data below a defined threshold are suppressed which causes a strong data reduction. The data from four DHPs get combined on one FPGA based Data Handling Engine (DHE)[7]. At this point, for each of the 40 half ladders exists one DHE and one optical output link. The inner layer has an occupancy of 3% while the outer only has 1%. This effect causes a much higher bandwidth usage in the inner layer compared to the outer layer. Additionally a particle from interaction point causes hits in the same segment of the detector. To equalize the load on the 40 links, eight FPGA based Data Handling Concentrator (DHC)[8] perform a load balancing. Therefore each DHC reads data from two sensors on the inner layer and three sensors on the outer layer in opposite direction. A sub event building combines the data and sends it out alternating to one of the four output links (figure 2.11). Because of the load balancing, the data coming from five links can be reduced to four links without data reduction. The combined system out of five DHE and one DHC is called DEPFET Handling Hub (DHH)[9]. The total number of links after the DHHs is then 32 and these 32 output links lead then to 32 Online Selection Nodes. cf. [45][54][55]

---

[7] In previous versions the Data Handling Engine (DHE) was called Data Handling Hybrid (DHH)

[8] In previous versions the Data Handling Concentrator (DHC) was called Data Handling Hybrid Controller (DHHC)

[9] In previous versions the DEPFET Handling Hub (DHH) did not have a name yet and the acronym DHH was used for the system which is now called DHE.
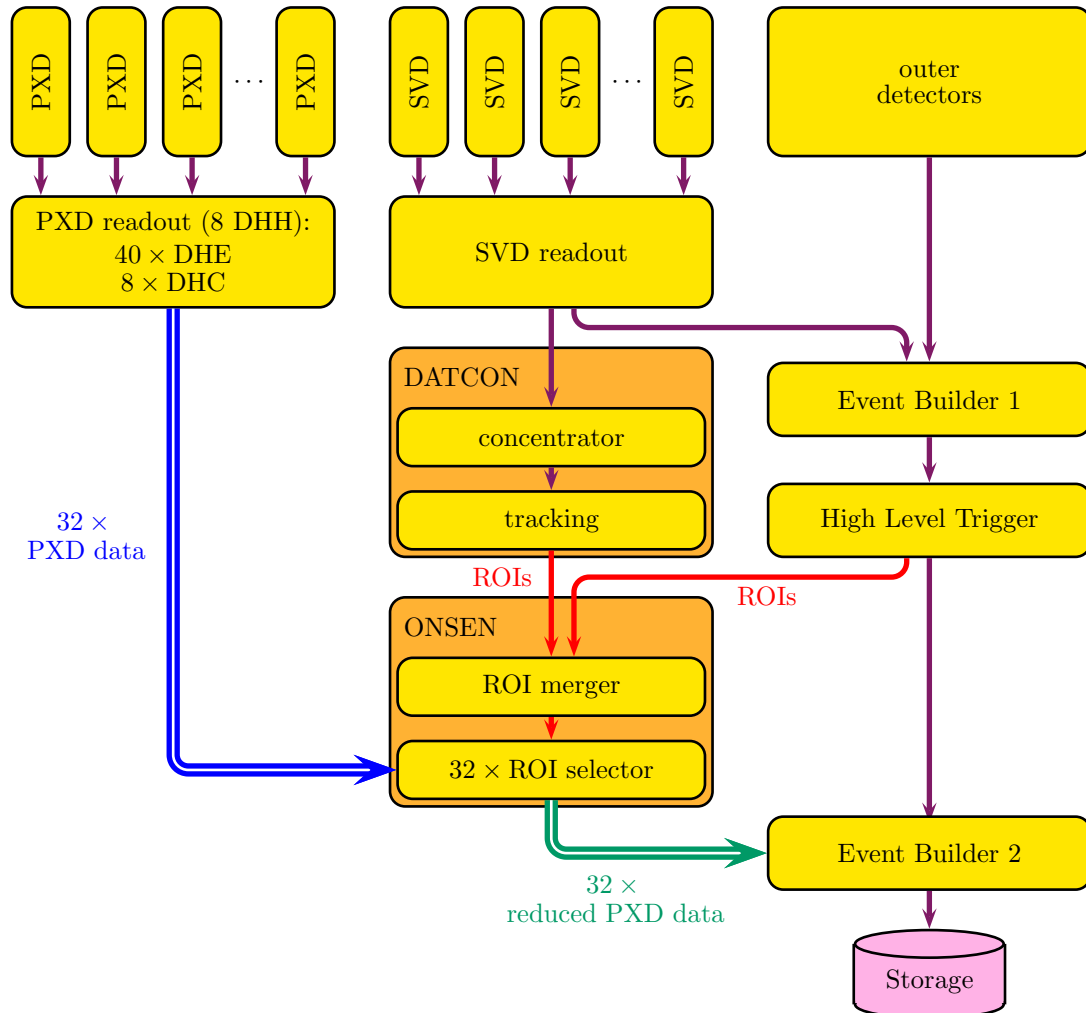
Figure 2.10.: Schematic view of the DAQ for the setup at KEK. From the eight DHC (see chapter 2.5.1) will go 32 links (blue ■) to 32 ROI selector nodes to reduce the data based on the ROIs (red ■) from High Level Trigger (HLT) and Data Acquisition Tracking Concentrator Online Node (DATCON). The reduced data (green ■) will be sent to the event builder.
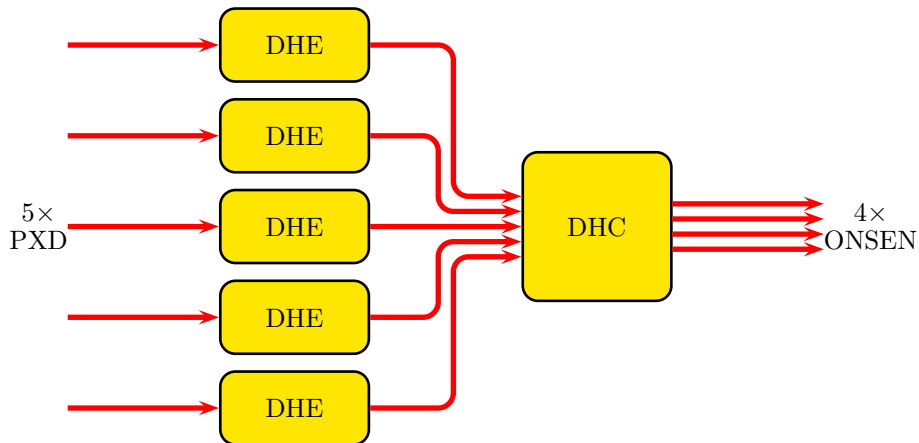
Figure 2.11.: Schematic view of the DHH readout behind the DHPs. The DHC receives data from five DHE which includes data of one sensor per DHE. After the load balancing and sub event building, four outputs send data to four ONSEN ROI selector nodes. With this setup, in total eight DHHs will be used.

2.5.2. Region of Interests (ROI) Selection

To be able to select physics hits out of the huge amount of background hits, the concept of Region of Interests (ROI) is used. For this, tracks of particles from physics events are extrapolated by using data from outer detectors. Around those tracks the tracking systems calculate areas on the PXD sensors where the particles passed the PXD and only data in those areas are kept. More details on this concept I describe in chapter 3.4.

As source for ROIs are used two independent systems with different algorithms. One is the High Level Trigger (HLT) and the other is the Data Acquisition Tracking Concentrator Online Node (DATCON).

High Level Trigger (HLT)

The HLT is based on a PC farm with in total about ≈ 1600 cores. It uses data from SVD and the outer detectors (CDC, particle identification, ECL, KLM). After a helix track finding it back projects the tracks to the PXD sensors and based on the inaccuracy of the tracking it calculates the ROI size. Beside the ROI calculation, also a software trigger for event rejection is performed. Because of the big amount of data used on HLT and the usage of PC architecture, we expect a latency up to 5 s. cf. [56]

Data Acquisition Tracking Concentrator Online Node (DATCON)

As a second source of ROIs, the DATCON uses only data from SVD. Data from the outer detectors are not used on this system. It runs on a FPGA based hardware (Compute Node; see chapter 3.1) and the algorithm is based on a fast Hough transfor-

mation for helix tracking. With the smaller amount of data and the hardware which supports pipelining and high rate of parallelisation the latency is only up to $10\,\mu s$. cf. [57][58]

2.5.3. Trigger Concept at Belle II

At the Belle II experiment the SuperKEKB accelerator will operate with a luminosity of $L = 8 \cdot 10^{35}\,\mathrm{cm}^{-2}\,\mathrm{s}^{-1}$. The trigger has to fulfill the requirement, to trigger all physics processes which are included in the planned research as well as processes used for calibration. The trigger rates for some physics processes are shown in table 2.1.

Table 2.1.: Interesting physics processes and calibration events for $\Upsilon(4S)$ decays. cf. [45]

Physics process	Cross section (nb)	Trigger rate (Hz)
$\Upsilon(4S) \rightarrow B\,\overline{B}$	1.2	960
Hadron production from continuum	2.8	2200
$\mu^+\,\mu^-$	0.8	640
$\tau^+\,\tau^-$	0.8	640
for $\theta_{\mathrm{lab}} \geq 17°$:		
Bhabha	44	350
$\gamma\,\gamma$	2.4	19
2γ (for $p_t \geq 0.1\,\mathrm{GeV}/c$)	≈ 80	≈ 15000
Total	≈ 130	≈ 20000

The requirements for the trigger system are then a high efficiency for $\Upsilon(4S) \rightarrow B\,\overline{B}$ decays and continuum, an average trigger rate of $30\,\mathrm{kHz}$, and a latency of $5\,\mu s$, all of this with a precision smaller than $10\,\mathrm{ns}$ and an event separation of at least $200\,\mathrm{ns}$. At the end the setup should be robust and flexible.

To be able to fulfill these requirements, the Belle II trigger works in two steps. As first, the sub-detectors have separate sub-triggers. These sub-triggers are based on Field Programmable Gate Array (FPGA) to support reconfiguration as well as a high-speed serial data processing. All these sub-triggers forward their trigger decisions to the Global Decision Logic (GDL) which sends the final decision as a trigger signal. Overall the latency fulfills the requirement of $5\,\mu s$ latency. The sub-triggers are for the sub-detectors CDC, ECL, PID and KLM. cf. [45]

CDC Trigger

At the CDC the trigger is split in two parts: a 2D and a 3D trigger. Both work partly in parallel. The 2D trigger processes the CDC data in perpendicular projection and triggers by tracking. For a tracking of charged tracks it is searching for circular shaped tracks. At first the data are transformed in a conformal transformation where all hits

circular tracks from the vertex will describe a line in the conformal space. As second step the tracks are found by a Hough transformation. The results of this tracking are sent to the GDL as the CDC 2D trigger. With these values a 3D fit is performed by running an r-ϕ-fit and r-z-fit to find the axial coordinate of the track. The result is then the CDC 3D trigger. cf. [45]

ECL Trigger

For a trigger based on the ECL data an FPGA based hardware is used. Here it analyzes the data from the ECL. A key component is the so-called fast shaper. It analyzes the signal by pulse height and time length. Based on these values ECL trigger forward the trigger decision to the GDL. cf. [45]

PID Trigger

The PID trigger uses the data of the Čerenkov detectors which were not used for triggering before. The parameters to calculate a trigger decision are position and time. cf. [45]

KLM Trigger

The outermost trigger is from the KLM detector and is manly for a trigger decision based on existing μ pairs in the event. It is planned to perform a 3D tracking on those data if there is enough hits in the KLM. cf. [45]

CHAPTER 3

THE REAL-TIME DATA REDUCTION SYSTEM

The Online Selection Nodes (ONSEN), as the real-time data reduction system, consists of two key components, the ROI Merger Node and the ROI Selector Node. The ROI Merger Node receives the ROIs from the two sources, HLT and DATCON, to combine them for further processing. The ROI Selector Nodes receive the pixel data and ROIs to process a pixel data reduction. [59][60]

3.1. Compute Node

The ROI Merger Node, ROI Selector Node as well as the DATCON use the same hardware. The Institute of High Energy Physics (IHEP) in Beijing together with Justus-Liebig-Universität Gießen (JLU) developed this hardware in a close cooperation and called it Compute Node (CN). We will use the newest revision 3 in this Experiment. The previous versions 1 and 2 were developed using one board in AdvancedTCA standard equipped with five FPGAs, four for algorithms and one as a switch to connect the algorithm FPGAs with the backplane connector.

It was decided to use a more modular design in the following development. In the recent version 3, the CN got split in small AMC cads (figure 3.1) in xTCA (see chapter 3.1.1) standard holding one Xilinx Virtex5 fx70T FPGA as well as a RAM slot supporting up to $2 \times 2\,\mathrm{GB}$ DDR2 RAM, four SFP cages for e.g. optical links with up to $3.125\,\mathrm{Gbit/s}$ and one RJ45 gigabit Ethernet connector. In the next revision the AMC boards will have only two cages but they will be SFP+ and support up to $6.25\,\mathrm{Gbit/s}$.

One Carrier Board (figure 3.2) can hold up to four AMC cards. This Carrier Board is equipped with an Xilinx Virtex 4fx60 FPGA as a switcher to support connections between the AMC cards and the AdvancedTCA backplane. It also offers hard-wired high-speed interconnections between all AMC cards on the Carrier Board. The combination of four AMCs and the Carrier Board forms one CN revision 3. cf. [61][62]
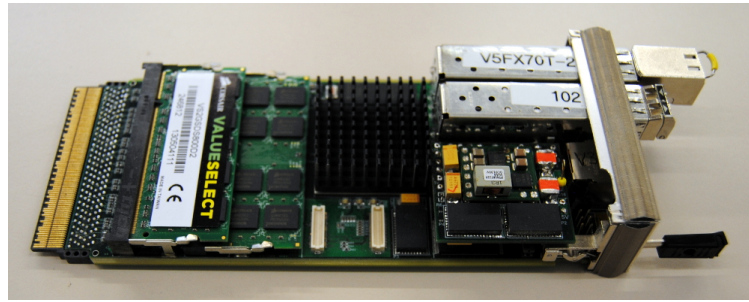
Figure 3.1.: xFP of CN rev. 3 equipped with 2×2 GB DDR2 RAM, one SFP optical transceiver and one SFP transceiver for RJ45 cables. [59]

Figure 3.2.: Prototype of AdvancedTCA carrier board equipped with 4 xFP. [59]

3.1.1. AdvancedTCA, AMC and xTCA

The Advanced Telecommunications Computing Architecture (AdvancedTCA) is a specification for telecommunication industry and designed for high-speed data processing and transfer. In big AdvancedTCA shelfs with up to 14 boards (figure 3.3(a)) in $19''$ racks or 16 boards in $23''$ racks this standard supports a full mesh backplane (figure 3.3(b)). With this possibility the shelf provides direct hardwired interconnections between all boards. A full size AdvancedTCA board supports the usage of multiple Advanced Mezzanine Card expansion boards. In case of the Compute Node is used a xTCA card which is a AMC card based on MicroTCA standard with some modifications.
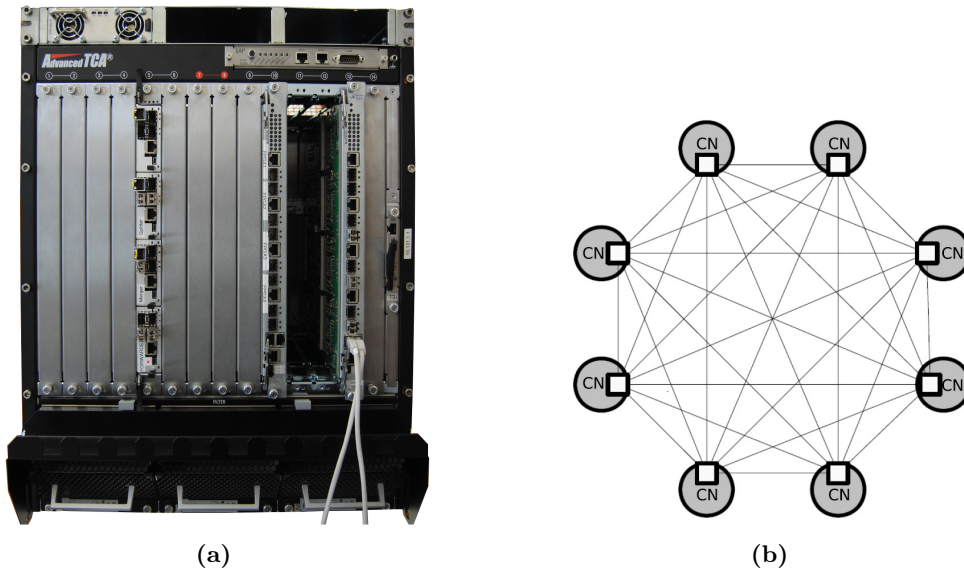
Figure 3.3.: (a) A 19″ AdvancedTCA shelf with 14 slots equipped with one CN of version 3 (5th slot from left) and two of version 2 (2nd and 5th slot from right). (b) Scheme of full mesh interconnections. For clarity the number of CN is reduced to 8. [63]

3.2. ROI Merger Node

The ONSEN system needs one ROI Merger Node to combine all incoming ROIs from HLT and DATCON. Because of the different latencies of the two systems, the ROIs from DATCON arrive already after 10 µs while HLT could need up to 5 s. For the further processing all ROIs for one trigger have to be sent at once. Therefore the DATCON ROIs will be stored until the also HLT delivers its corresponding ROIs. As soon as the HLT ROIs arrive, the DATCON data for the same trigger are read back from memory and get merged with the HLT data. At this merging process the data are combined in a way, that the order of sensor ID is kept as far as it is important for the selection process. The priority in the merging is on HLT side. As soon as the HLT delivers data, the merging process starts. The resulting merged ROI data will be sent forward to all ROI Selector Nodes (figure 3.4). For the final setup at the experiment an ROI distribution system running on the Carrier Board is under development. This system demultiplexes the merged ROI data to the different ROI Selector Nodes in the way that each node receives only the ROIs needed for processing the incoming DHC data and reduces the bandwidth. cf. [61]
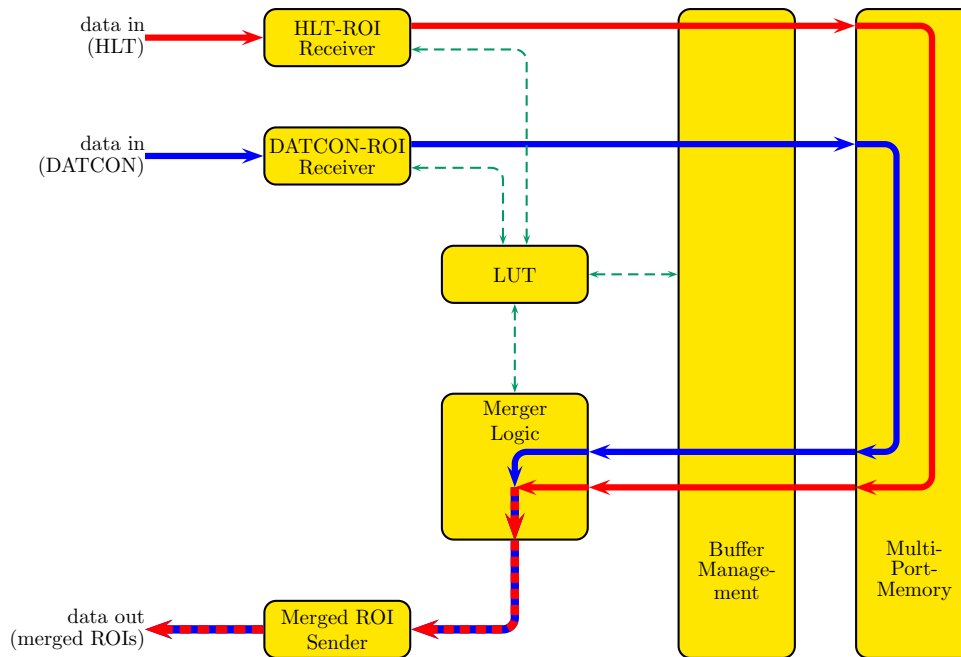
Figure 3.4.: Schematic diagram of the ROI merger node. Data path of ROIs from HLT in red ■ from DATCON in blue ■ and the merged output data in red-blue ■■ dashed. The green ■ dashed lines represent the communication to the look-up table for a correct buffer handling.

3.3. ROI Selector Node

The ROI Selector Node works with a similar data handling logic like the ROI Merger Node. Here The PXD data arrive directly from the DHC. The ROIs from the Merger Node arrive as soon as the HLT was delivering ROIs which can take up to 5 s. Until this moment the DHC data have to be stored in memory. As soon as ROIs arrive there, they are transmitted to the Selection Logic followed by the DHC data for the same trigger. The selection logic performs a data reduction based on the ROIs and sends out the reduced data to the event builder for storage and later offline analyses (figure 3.5). cf. [61]
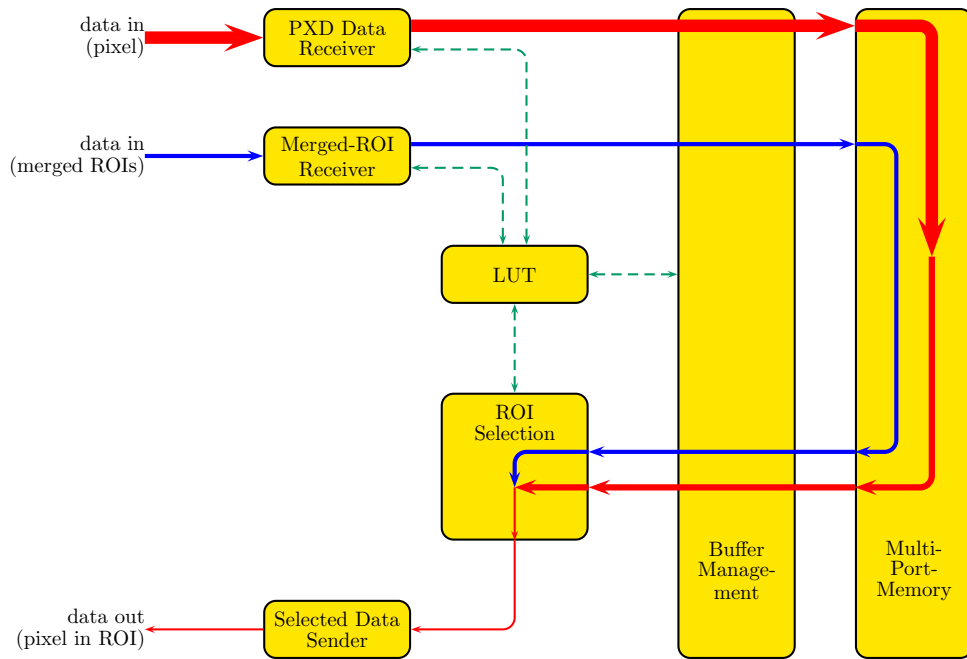
Figure 3.5.: Schematic diagram of the ROI selector node. The pixel data path in red ■, the ROIs from the merger node in blue ■. The green ■ dashed lines represent the communication to the look-up table for a correct buffer handling. The amount of pixel data gets rejected at two points. First in the memory by event rejection and second in the ROI selection logic.

3.4. The Region of Interests

As mentioned before, the PXD detector will have a huge background during the physics runs. We expect to have a maximum occupancy of 1% in the outer PXD layer and 3% in the inner layer. With the size of the sensors of 250×768 pixels this results to ≈ 1900 firing pixel per sensor in the outer layer and ≈ 5700 in the inner layer. with 40 sensors, a trigger rate of $30\,\mathrm{kHz}$ and the used data format, this leads to a data rate of up to $20\,\mathrm{GB/s}$. This data rate is much too high to be able to store all registered data. For an effective data storage it is important to reduce it. This will be done in two ways: first is by rejecting data for events without interesting data and filtering out the physics data on the sensors. The second way is a so-called Region of Interests selection and I will explain it in detail in the following chapters (figure 3.6).
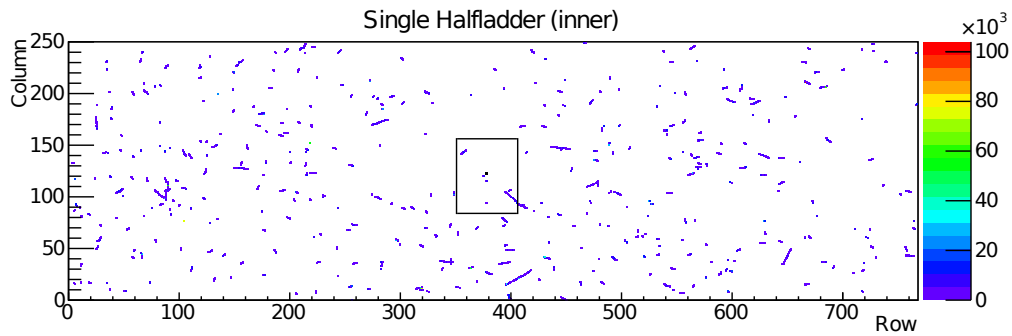
Figure 3.6.: Inner layer of PXD with simulated Touschek background data (see figure 2.7) and one example hit and ROI to illustrate the data reduction mechanism. All data outside the Region of Interests would be discarded by the ROI selection system. [59]

3.4.1. The Concept

A Region of Interests selection is based on the idea that we want to keep only data where we know that they include hits from the collision event. At Belle II we use two systems, HLT and DATCON (see chapter 3.4.2) to fulfill this function based on the data of the outer detectors. Because every reconstruction of the possible hit point has an error, not only one hit on the PXD will be kept but instead a small region where a possible hit could be will be kept.The error of the ROI calculation systems cause the size of regions and the errors are dependent on the direction. The describe these errors in the ROI definition, several shapes are possible and were discussed during

(a) Rectangular ROI definition with two points. One at the minimum for both coordinates (x_1, y_1) and one for the maximum coordinates (x_2, y_2). This definition is used at the experiment.

(b) Alternative rectangular ROI definition. Here one point is set at the minimum coordinates (x_0, y_0) and the width is defined over Δx and Δy.

(c) Elliptic ROI definition. Here the ROI is defined with the center point (x_c, y_c) and the size over the radii in two direction r_x and r_y.

Figure 3.7.: Examples for possible ROI definitions. Beside others these three possibilities were discussed. The version in (a) is the definition which is used in the experiment.

development (figure 3.7).

Beside the accuracy of describing the possible hit and the calculation errors, also the data format was important in the decision. Each ROI has to include some information for position and size. In the current format this data needs additional the information on which sensor the ROI is placed (called DHE-ID), because the ROIs are delivered globally and get split to the corresponding Selection Nodes on a later stage of the system.

Two point definition

A ROI definition based on two points is the simplest way. It provides the maximum and minimum for hit plus inaccuracy in both coordinates (figure 3.7(a)). This version has the advantage that we have some values for a simple and especially fast comparison $x_1 < x < x_2$ and $y_1 < y < y_2$.

Beside the DHE-ID (6 bit) the coordinates have to be included in the data format. We need 10 bit for 768 rows and 8 bit for 250 columns. In total this format needs 42 bit. Because of the decision of a 32 bit alignment we need two 32 bit words for the information.

Point and width definition

Another possibility for a rectangular definition is one point and the width. The point can be placed on several places of the ROI. It could be at the edge (figure 3.7(b)) or at the center. The coordinate check is still a simple comparison like with a two point definition, just that the minimum and maximum coordinates have to be calculated before (for the example in figure 3.7(b): $x_{min} = x0$ and $x_{max} = x_0 + \Delta x$ and similar for the y coordinates). Because additions are easy and fast to calculate on a FPGA platform it is not more complex or resource consuming than the two point version. It only has to be taken care of that the calculated minimum and maximum coordinates have to be within the sensor size.

With a maximum ROI size which covers the whole sensor for the width, the same resolution is needed as for points. This results to 42 bit as well and we would need also two 32 bit words like in the two point version.

Square ROI

With a square shaped ROI both widths are the same, so we could save one value. If we allow ROI widths of maximum 256 instead of the full ladder, the width needs only 8 bits and the whole data format would fit in 32 bit. It would be a strong data reduction but the ROIs are not symmetric. Because a track from interaction point which goes through the sensor in a flat angle has a long width in z-direction and only a small dimension in r-direction a square shape would give a big ROI where the most of the covered area is known as area without interesting data.

Elliptic ROI

An elliptic ROI is closer to the real inaccuracy of the tracking systems. It can describe

55

the best the intersection of the particle track and sensor together with the tracking error. As the best description the orientation of the ellipse matters, but as well for reducing the data amount the definition can be reduced to a fixed orientation with the ellipse axis in x and y direction (see figure 3.7(c)). In total we would need then the center point (x_c, y_c) and the two radii r_x and r_y. This would need about the same amount of bits per ROI like the rectangular version. At the end there stands only the more accurate description which would reduce the background data about 20% more compared to the rectangular ROIs covering the same area. But against this stands a complicated check logic to see if the hit is inside of the ROI. Mathematically the functions look simple. For an ellipse with the two focal points F_1 and F_2 the definition of a helix says, that for all points P of the ellipse the sum of the distances from point to focus is constant.

$$\overline{PF_1} + \overline{PF_2} = C = \text{const.}$$

This would mean that we could perform a simple comparison of the value C for an arbitrary point and the constant for the ellipse to perform an ROI check. The constant we can get from the radii in the ellipse definition, but the value C for each point has to be calculated by using the Pythagorean theorem. FPGA platforms are not efficient in calculations with floating point variables or complex functions. The square root in this formula has to be implemented as logic and would be very resource consuming and can cause a bad timing. At the end it was decided to keep the two point definition to be sure to meet the performance requirements for ROI reduction.

3.4.2. ROI Sources

Because of different algorithms there we use two separate ROI sources: The High Level Trigger and the Data Acquisition Tracking Concentrator Online Node. They are used in parallel and the ONSEN system merges the data. Both will deliver the ROI information in the form of two points which mark the lower edge and the upper edge (figure 3.8).

High Level Trigger (HLT)

The hardware for the algorithm of the HLT is a PC farm. As data source the HLT uses the SVD hits and also the hits from the outer detectors (CDC, PID, ...). The tracking algorithm is based on a hit to hit neighbor finding and is using a neural network. The calculation time of this system is then up to 5 s and the resulting ROIs are send forward to the ONSEN merger node. cf. [56]
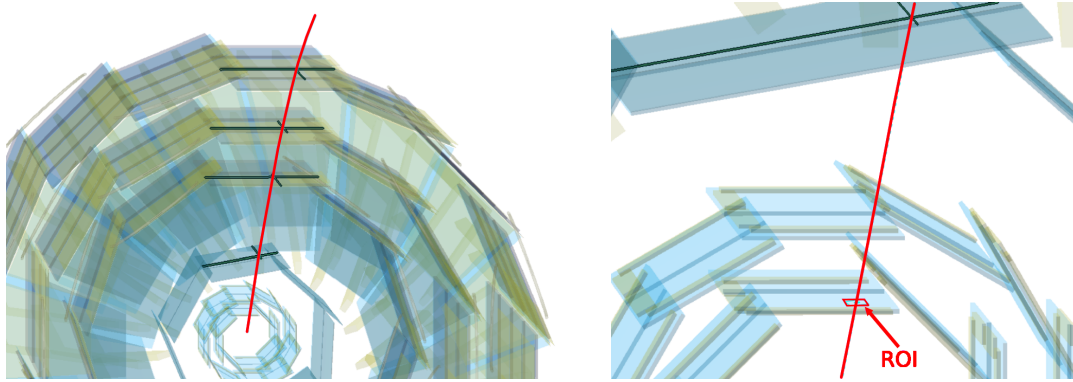
Figure 3.8.: Illustrations of track projection from SVD to PXD. Based on the fired strips in SVD (upper four layer in left picture), a track is reconstructed and back projected to the PXD planes (detailed view in right picture). According to [57]

Data Acquisition Tracking Concentrator Online Node (DATCON)

The DATCON[10] is a track reconstruction system running on a FPGA based hardware (Compute Node (CN), see chapter 3.1). The system receives the data from SVD via 48 optical links from the SVD front end electronics. With this data source it needs at least three hits in SVD to be able to reconstruct. At a first step the data get concentrated on 12 AMC cards and forwarded to the two tracking AMCs.

The tracking system of DATCON is using a conformal transformation[11] followed by a fast Hough transformation[12] algorithm. With the conformal transformation, hits on a circular shaped track in real space will be on a line in conformal space. The following fast Hough transformation is then used to find the lines. Based on the track parameters found by this algorithms, ROIs in the PXD sensors get calculated within maximum 10 µs and transmitted to the ONSEN system. cf. [57][58]

---

[10]At earlier stages of the development DATCON was an acronym for Data Concentrator. Later it got changed to Data Acquisition Tracking Concentrator Online Node.

[11]A conformal transformation is an angle preserving transformation which converts all coordinates in real space to corresponding coordinates in conformal space over the formulas $x' = (x - x_0)/r^2$ and $y' = (y - y_0)/r^2$ with $r^2 = (x - x_0)^2 + (y - y_0)^2$. With the reference point (x_0, y_0) it is vertex constrained and all circular tracks through this point appear as straight lines in the conformal space. cf. [64][65]

[12]A Hough transformation is a method to recognizes any kind of patterns which are possible to describe by a mathematical function. The tracking system uses it to find lines in the conformal space described over $r'(\theta) = x' \cos(\theta) + y' \sin(\theta)$. In the hough space with the axes r' and θ all possible combinations which describe a line going through a point in the $x'y'$ space are registered. At the end the parameters of a reconstructable track appear as a peak in the hough space and has to be found by a separate peak finding algorithm. In a so-called fast hough transformation the hough transformation will have a very rough resolution of e.g. 2×2 pixels and continue recursively on the areas with the most entries. This algorithm includes a peak finding as well. cf. [66][65]

3.5. ROI Selection Logic

The selection process needs as first information the ROI data. These data arrive serial and get stored to a buffer for later parallel processing. This buffer has parallel outputs, one for each ROI.

At next the corresponding DHC data get sent in. For non-PXD data the frames get forwarded to the output without processing while PXD data are sent to a FIFO to buffer the original data format while in parallel they get decoded and forwarded to several ROI check cores. These cores check the pixels for all ROIs in parallel. If the pixel is in at least one ROI, the undecoded original data for this pixel are sent out. If requested by a flag in the ROI data, al ROIs are sent out in an own frame. This whole process is handled by a frame handler which controls if a frame should go though the selection logic or not. A schematic overview about the selection logic is shown in figure 3.9. In the following chapters I describe the components of the ROI selection logic in detail.
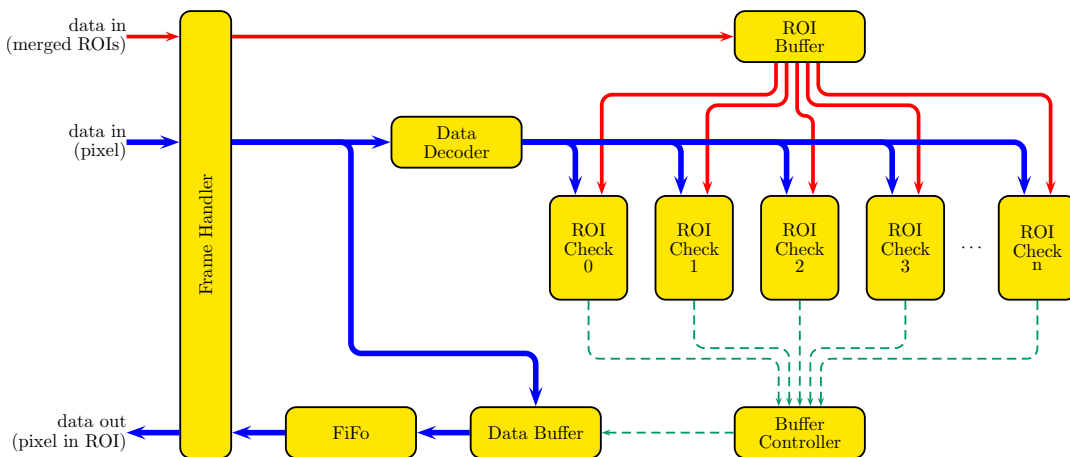
Figure 3.9.: Schematic diagram of the ROI selection logic. The ROI data path in red ■ with a parallel distribution of the ROIs to ROI check logic. The pixel from the merger node in blue ■ gets distributed to all ROI checks in parallel and send control signals (green ■ dashed lines) to operate the pixel data buffer for data reduction or output.

3.5.1. Frame Handler

The data stream from DHE contains data frames of several types. Some frames have the purpose of structuring the stream and delivering information which do not have to be transmitted with every frame. Other frames contain the data from the detector. The processing logic add two new frame types with e.g. debug informations. This data frames arriving from DHC have to be recognized and handled depending of their content. For this a frame handler reads out the frame type ID. A second input stream

delivers the ROI frames, but there is only one per event. With these two inputs, the frame handler starts to process the data.

- First part is that the event builder behind ONSEN wants to have a guaranteed information about the trigger number. If no data arrive from DHC (e.g. because of a link error) at least the HLT ROIs arrive. To have the trigger number in the ROIs also on the event builder, the header information in the ROI frame will be sent out as a new ONSEN trigger frame in from of all frames.

- All frames not containing the DHP zero-suppressed data will be forwarded unchanged. This frames are e.g. the different start and end frames.

- For debug reasons it is interesting to have the ROIs from HLT and DATCON also in the offline data. The HLT delivers its ROIs beside ONSEN also directly to the event builder, but the DATCON does not. To have all this information available for later checks the ROIs will be sent out as a separate ONSEN ROI frame in front of the last frame for the event (DHC end frame).

- If the input frame is a DHP data frame which contains the zero-suppressed data, the header will be passed through to the output and the frame type will be changed to a processed data frame. The data content will be forwarded
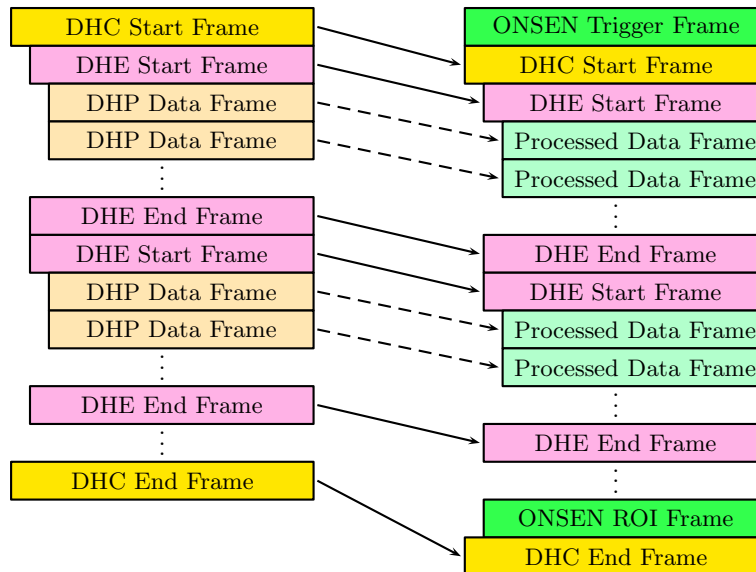
Figure 3.10.: Data structure before (left) and after (right) processing on ONSEN. The DHC■/DHE■ start and end frames are sent forward unchanged. The DHP frames (DHP Data Frame ■) are processed (dashed arrow) if there exist corresponding ROIs and a frame with reduced date is sent out (Processed Data Frame ■). Additionally the frame handler adds an ONSEN trigger frame ■ and optional an ONSEN ROI frame ■ for debug purpose.

together with the corresponding ROIs to the selection process. The data frames are always only for one DHP which is a quarter of a sensor while the ROIs are for the whole PXD. To match this two data streams only ROIs for one sensor are forwarded to the ROI buffer and then the pixel data for the same sensor are sent to the ROI check logic. If the next pixel are for an other sensor, the ROI buffer will be reset and new ROIs are sent.

A more detailed description of the frame handler and its state machine is presented in chapter B.2 in the appendix. Here all states and their transition conditions are explained.

3.5.2. ROI Buffer

The ROI buffer receives the ROIs serial. One ROI consist of two 32 bit words containing DHE-ID and the two corners $(row_1, column_1)$ and $(row_2, column_2)$ to describe the minimum and maximum coordinates of a ROI (figure 3.11). All received ROIs are written into a buffer which is 36 bit wide (two times 10 bit for row addresses and two times 8 bit for the column addresses) and recently it has a depth of 32 . This buffer has two functions. At first it has to buffer all ROI for the processing time of the whole PXD data frame. As second function this buffer has 32 outputs to provide a permanent parallel output of all ROIs during the whole ROI check process. Before receiving new ROIs this buffer has to be reset.

In case of receiving more ROIs for one PXD data frame than available buffers, it was decided to count it as a case of so many ROIs that we keep the whole content of the PXD sensor, which is realized by setting the last buffer entry to the value for a full sensor ROI: $(0, 0)(767, 255)$.

31	30	29	28	27	26	25	24	23	22	21	20	19	18	17	16	15	14	13	12	11	10	9	8	7	6	5	4	3	2	1	0
						unused until now															flag	DHE-ID						$row_1[9:6]$			
$row_1[5:0]$						$column_1$								row_2							$column_2$										

Figure 3.11.: ROI data format: Two 32 bit words. In the first word are transmitted the DHE-ID and the upper 4 bits of the row_1 address. The flag in bit 10 is set by the ROI merger node and shows if the ROI originally comes from HLT (0) or from DATCON (1). In the second word are transmitted the lower 6 bits of row_1 as well as the values for $column_1$, row_2 and $column_2$.

3.5.3. Data Decoder

To be able to process a ROI selection, I need to have the pixel data as unencrypted values. For this the data frames from DHE containing zero-suppressed pixel data I have to decode these data. Each sensor is split into four sections in the column address, each read out by a separate DHP. Its identification number is transmitted in the header. Together with the column address in the data word (DW) the 8 bit

column address is built (see 3.12). The row address is then included partly in the start of row (SOR) word and partly in the DW (see 3.12). After decoding, the unencrypted pixel coordinates are forwarded to the ROI check logic. Because this whole process is pipelined, the output has a delay compared to the input, but allows to decode input data in with full speed.

(a) Data format for the start of row (SOR) words from DHP.

(b) Data format for the data word (DW) from DHP.

Figure 3.12.: Data format for zero-suppressed data from DHP. These data are encapsulated in the frame format from DHE. Both send some header words in front of the data where the first of all this words contain the upper two bits for the column address. The 8 bit column address is then sent with $column[7:6]$ in header as an ID to identify the origin DHP where the data are from. The $column[5:0]$ is then sent with each DW. The row address is split as well. The upper bits $row[9:1]$ are in the SOR while the last bit $row[0]$ is in the DW.

3.5.4. ROI Check Logic

The ROI check itself is based on a basic comparison for both coordinates of pixel data from the decoder and ROI coordinates from the ROI buffer:

$$row_1 < row < row_2 \quad ; \quad column_1 < column < column_2$$

The processing time is independent from the input data and therefore it was possible to parallelize the check for each ROI. At the current setup are implemented 32 ROI check in parallel. The data buffer controller handles the result of the comparison to send out the data for pixel which are in at least one region.

3.5.5. Data Buffer and Data Buffer Controller

To be able to send out the pixel data in the decoded zero-suppressed format the original input data are stored in a buffer. Based on the information from the ROI check whether the pixel was in at least one ROI or not, the controller of this buffer decides which data words have to be sent out. The challenge on this task is, that the SOR information have to be sent only if a DW for this row has to be sent. Therefore a simple FIFO as buffer does not work. Because the decode and check process is pipelined, the undecoded data are delayed to keep them synchronous with the ROI check output. The SOR informations are buffered separately to send them out as soon as corresponding DW has to be sent out. Additionally the output of the 16 bit words of the zero-suppressed format will be filled up at the end of a frame to guarantee a 32 bit alignment.

3.5.6. First Tests of ROI selection algorithm

Figure 3.13.: ROI selection test with random data. In this plot ROIs are marked yellow ▮. All red ▮ hits were rejected and green ▮ once were identified. Also an overlap of ROIs was simulated and is handled correctly.

During development process the first tests of the ROI selection logic I did with random data. At this time for column and row I used 12 bits which allowed to have a unique pixel number for all pixel inside PXD. In the later development this changed because of a more precise defined data format which uses then less bits and delivers a separate ID for the sensor. Because of the 12 bit in the first test, it was possible to address 4096×4096 pixel as you can see in figure 3.13. In this test I generated the random data and random ROIs under Linux and sent them into the ROI selection hardware. The out coming data I checked for consistence and bit errors.

- $1.9 \cdot 10^6$ events with 31 ROIs checked.

- in total $1.9 \cdot 10^{10}$ pixel were processed with the ROI selection.

- $\approx 40\%$ were correctly identified as inside ROI.

- $\approx 60\%$ were correctly rejected as outside ROI.

- No bit errors or selection errors observed in this test.

This test was done still on the version 2 compute node, which is the previous version to the currently used hardware. As an second test I used simulated Touschek background data with random ROIs (se figure 3.14) to check the ROI selection algorithm. Also in this test I observed no bit errors or selection errors.
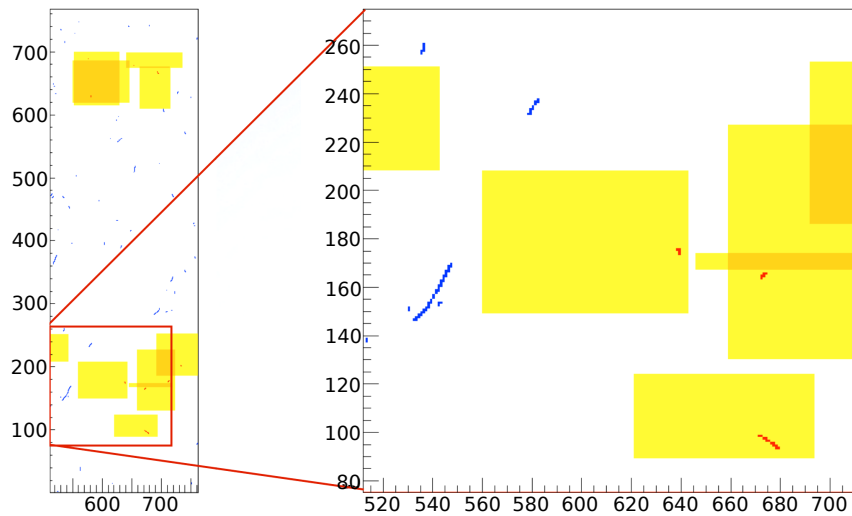
Figure 3.14.: ROI selection test with simulated Touschek scattering data. In this plot ROIs are marked yellow ■. All blue ■ hits were rejected and red ■ hits were identified.

3.6. Cluster Based Pixel Data Format

It is planned to provide the pixel data in a cluster based format. In this format each cluster will have a seed pixel and all other pixel belonging to the same cluster will be addressed relative to this pixel. The total data amount will not change significantly compared to the DHP format. The originally planned format was called DCE and was based on three different types of 16 bit word. Because this format uses 8 bit for the column address a split in four frames for each DHP as in the zero-suppressed is not needed in this format.

- Start-of-cluster: This word defines the start of a new cluster. As data content it includes the row address (10 bit) and the upper half of the column address (4 of 8 bit) of the first pixel.

- First cluster-member: After the start-of-cluster word follows the cluster-member words. One for each pixel. The First one includes the lower half of the column address (4 of 8 bit) of the first pixel and its ADC value.

- Next cluster-member: All other cluster members contain a relative position to the previous pixel. With some control bits the position can be pushed to or read back from a stack to allow a tree-like description of a cluster. As well as the first cluster-member they include also the ADC value (figure 3.16).

15	14	13	12	11	10	9	8	7	6	5	4	3	2	1	0
0	0					row[9:0]							$column$[7:4]		
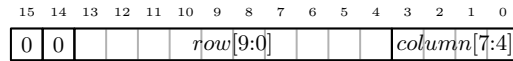
(a) Start-of-cluster word. The bit 15 is `1` for the header words which are not needed for decoding. For all words defining a cluster this bit is `0`. Bit 14 is `0` for start of frame and is followed by 10 bit for the row address of the seed pixel. For the 8 bit column address only the upper half is included in the start-of-cluster word.

15	14	13	12	11	10	9	8	7	6	5	4	3	2	1	0
0	1	1	$column$[3:0]				pu			adc[7:0]					
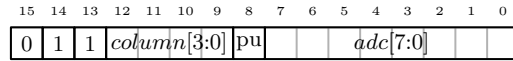
(b) First cluster-member word. Bit 15 is the same as in (a) and bit 14 is `1` for cluster-member. For a first cluster-member bit 13 is set to `1` and followed by the lower half of the seed pixel column address. Bit 8 (pu) is used as a flag to push the recent position to the stack during decoding. At the last 8 bit the ADC value is provided.

15	14	13	12	11	10	9	8	7	6	5	4	3	2	1	0
0	1	0	po	rel2prev			pu			adc[7:0]					
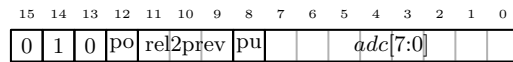
(c) Next cluster-member word. It is mostly the same as for the fist cluster-member in (b). The differences are bit 13 is set to `0` and instead of the lower column bits is provided informations for relative position description. Bit 12 (po) is here a flag to read back a position from the stack and bits 9-11 are the number to describe the direction to move compared to the previous pixel.

Figure 3.15.: Cluster based DCE data format. Each cluster starts with a start-of-cluster (a) followed by a first cluster-member (b) for the seed pixel. In case of more than one pixel additional next cluster-member (c) are attached.
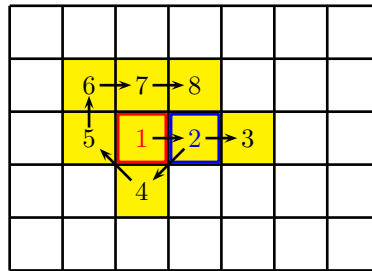
Figure 3.16.: Possible description of a cluster in DCE format. The Pixel 1 is the seed pixel. The cluster-member 2 is stored in the stack and will be read back after pixel 3 to be used as reference position to calculate the pixel 4. There exist multiple possibilities to describe a cluster with this format with different paths of the relative position calculation.

3.6.1. Cluster Data Decoder

Similar to the zero-suppressed data, for the processing of a ROI selection, it is needed to have the pixel data as decoded values. A decoder for this format reconstructs the real pixel positions to provide them to the ROI check logic. Also at this decoding the whole process is pipelined and the output has a delay compared to the input. Otherwise the output has the same speed as the input. Because of the future format

changes from DCE to FCE this decoder has to be rewritten.

3.6.2. Cluster Selection

The check for each pixel in a cluster works in the same way as the check for the zero-suppressed data (see chapter 3.5.4). A big difference is the handling of the clusters. During the development process three different possibilities were discussed. A pixel wise selection, full cluster selection by cluster seed and full cluster selection as soon as the cluster is partly inside the ROI. For clusters completely inside or outside a ROI all options have the result. For cluster on the edge it was discussed which option to choose. In the following I describe the three options. The chosen one is the third where all clusters which are at least with one pixel inside a ROI are selected completely.

Pixelwise Selection

The simplest idea to select the pixel of a cluster inside a ROI is a pixelwise selection. Here all pixel inside are selected while all outside are rejected. The advantages and disadvantages are:

+ The check process is very simple because each pixel is handled single.

− Clusters which are on the edge of a ROI get split.

− Loses cluster shape.

− Loses cluster amplitude.

− May lose cluster seed.

− Cluster data format has to be reencoded.

Here only pixel inside the region are selected. This causes a loss of the cluster amplitude and shape. It is possible that even the seed is lost. At the end the left part of the cluster is not usable for any reconstruction because the information is not significant anymore.
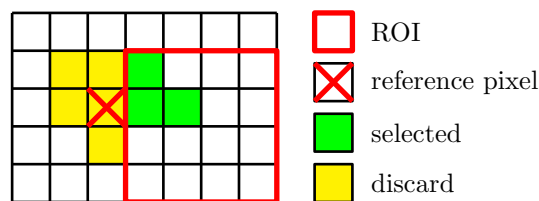
Figure 3.17.: Pixel wise selection of cluster each cluster. Each pixel will be checked separately if it is inside the ROI to be selected.

Selection by Reference Point (Cluster Seed)

Another idea was the selection of the whole cluster by its seed. Here only one pixel has to be checked to decide if the whole cluster is kept. Also the part outside the ROIs.

+ Keeps full cluster shape and cluster amplitude.

+ Check process is still simple because only the firs pixel (seed) has to be checked.

+ Cluster data format can be kept as it is.

+ No controlled buffer needed because each cluster decision is done at its first pixel.

− Position of cluster seed has to be the peak. In DCE format it was not guaranteed that this is the case. Here the seed could be random and a selection by this seed would be not significant.

(a) Whole cluster will be discarded. **(b)** Whole cluster will be selected.
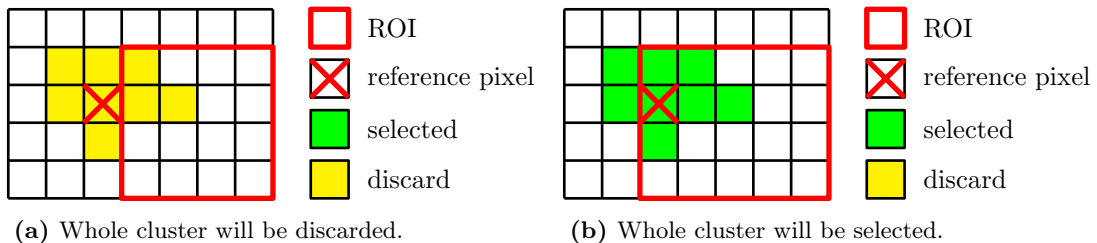
Figure 3.18.: Selection of cluster based on check of the seed pixel. If the seed pixel of the cluster is inside the ROI, the whole cluster will be selected.

Check Full Cluster

The finally chosen option is a selection of all clusters which are at least partly inside a ROI. With this selection also cluster are kept where the seed is outside but it is guaranteed that all pixel inside a ROI are forwarded to the event builder.

+ Keeps full cluster shape and cluster amplitude.

+ Cluster data format can be kept as it is.

+ Independent of seed position.

+ All pixel inside ROI are kept.

− All pixel of cluster have to be checked. Maybe only the last one is inside.

− A controlled cluster buffer is needed to store the data until the decision for keeping or discarding is made.

(a) Whole cluster will be discard.

(b) Whole cluster will be selected.
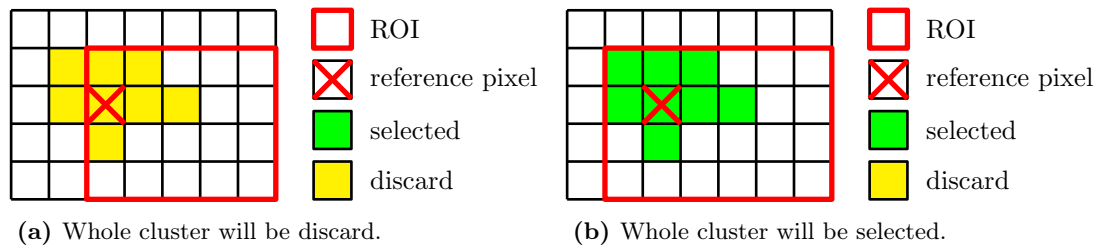
Figure 3.19.: Selection of cluster based on check of all pixel belonging to the cluster. If at least one pixel of the cluster is inside the ROI, the whole cluster will be selected.

3.6.3. Future Cluster Format

An important note is, that the DCE format described here is no longer in use. The clustering engine for DCE format was planned as an ASIC and will be replaced by a FPGA based algorithm and then called FCE. The data format will change, but was not defined during this work. An major change will be inclusion of a new flag to mark cluster to be kept, even if they are not inside a ROI. For this flag was no bit available at the old format.

CHAPTER 4

INVESTIGATION OF THE PROTOTYPE DATA REDUCTION SYSTEM

To verify that the ROI reduction system works as required, several tests were done. The large scale test so far was a test with a test beam at DESY. They offer test stations with electron beams in several energies (figure 4.2). At the electron/positron synchrotron DESY II a bremsstrahlung beam is generated by a carbon fibre. This γ beam hits on an exchangeable converter to generate electron-positron pairs. These electrons and positrons have a wide spread of energy between $1\,\mathrm{GeV}/c$ and $6\,\mathrm{GeV}/c$. To be able to provide defined energies for the tests, a dipole magnet spreads the
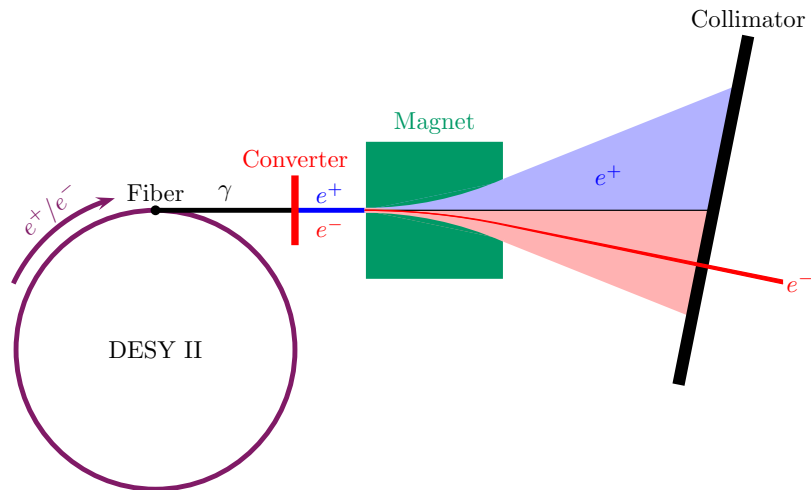
Figure 4.1.: Illustration of the test beam generation at DESY. At a converter electrons and positrons are generated and a magnet expands them by momentum and charge. A selected momentum will be cut out (red ■) and is then used at the experimental setup. According to [67]

particles horizontal and with a collimator one is able to cut on a certain energy (figure 4.1). At the test area is also a solenoid available to simulate the situation of the final experiment, where we will have charged particles in a magnetic field, which produce curved tracks. In addition, DESY provided six telescope detectors (pixel detectors). These were installed three in front of the PXD and three behind the SVD (figure 4.3). These detectors are calibrated and can be used to adjust the test setup.
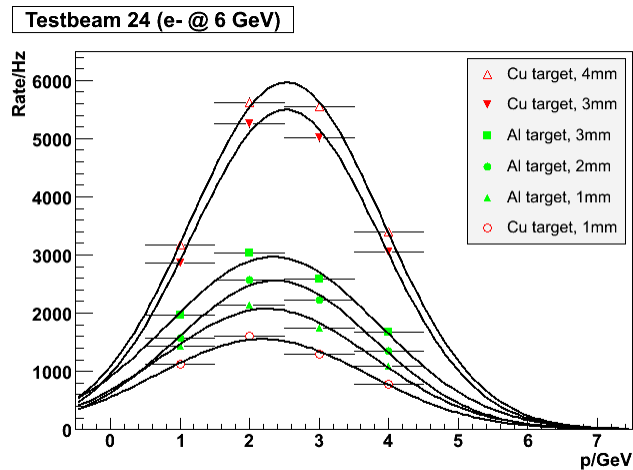
Figure 4.2.: Rate at DESY on beam line 24 on different beam momentums with different targets. [68]
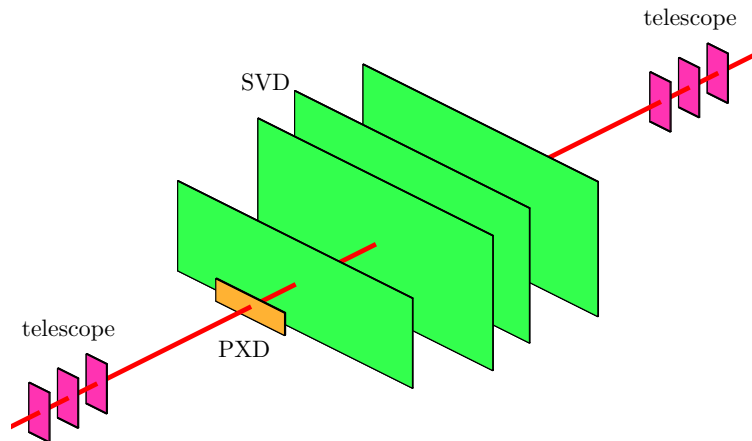
Figure 4.3.: Schematic view of the detector setup at DESY in january 2014. The PXD sensor (orange ■) in front of four SVD sensors (green ■) placed in the way to represent one detector segment of the final vertex detector. The small detectors in front and back of the setup (purple ■) are the telescope detectors provided by DESY.

4.1. Experimental Setup at DESY Beam Test

For this test the first prototypes of PXD and SVD sensors were available as well as a setup of event builder with HLT. From DAQ side the system was scaled down to read out one PXD and four SVD. The system was then running like a small scale version of the final setup and without the outer detector parts including ROI calculation from HLT and DATCON.

The downscaling on PXD side had the effect, that we had only one DHE and therefore also only one DHC with one output in use. The DHC did no load balancing and therefore had only one input channel and one output channel. For this setup we needed only one ROI Selection Node. The ROI Merger Node was still needed because both ROI sources were running, but the ROI distribution on the Carrier Boards of the CN were not needed (figure 4.5). Because of this we used for the small scale Pocket-ONSEN only the AMC cards in a MicroTCA development shelf.
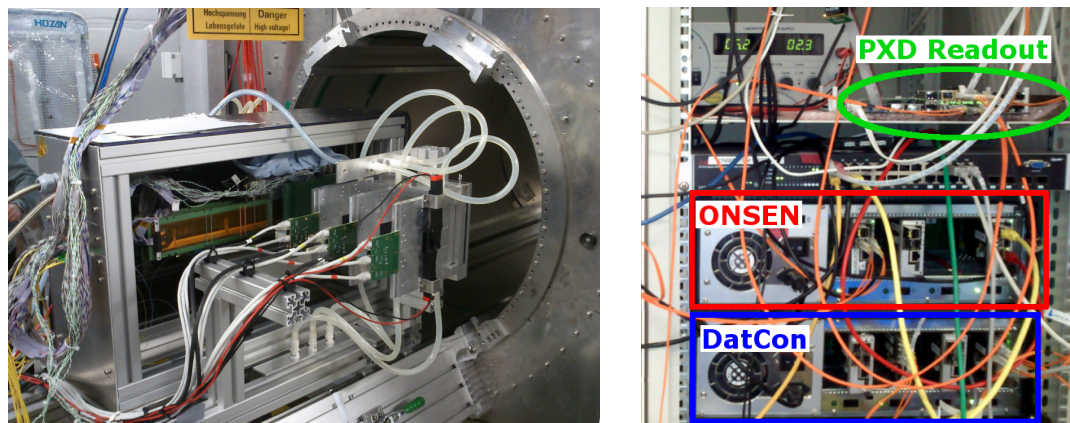
(a) Detector setup at DESY beam test. A schematic overview of the sensor placement is shown in figure 4.3.

(b) The Pocket-ONSEN (middle) setup at DESY together with the DATCON (bottom) and the DHC (upper right).

Figure 4.4.: Pictures of the detector setup and the DAQ system at DESY beam test.

4.2. Verification of ROI Selection Mechanism

At the data acquisition it is foreseen, that the data get reduced in the ONSEN system to reduce the bandwidth. This causes that the original PXD data like they were transmitted by the DHC are not saved on any kind of system, otherwise the bandwidth would not be reduced. With the kept informations after the ROI selection we only could verify if the out-sent pixel are inside one of the corresponding ROIs. To be able to verify the ROI selection mechanism it is important to check if all discarded pixel
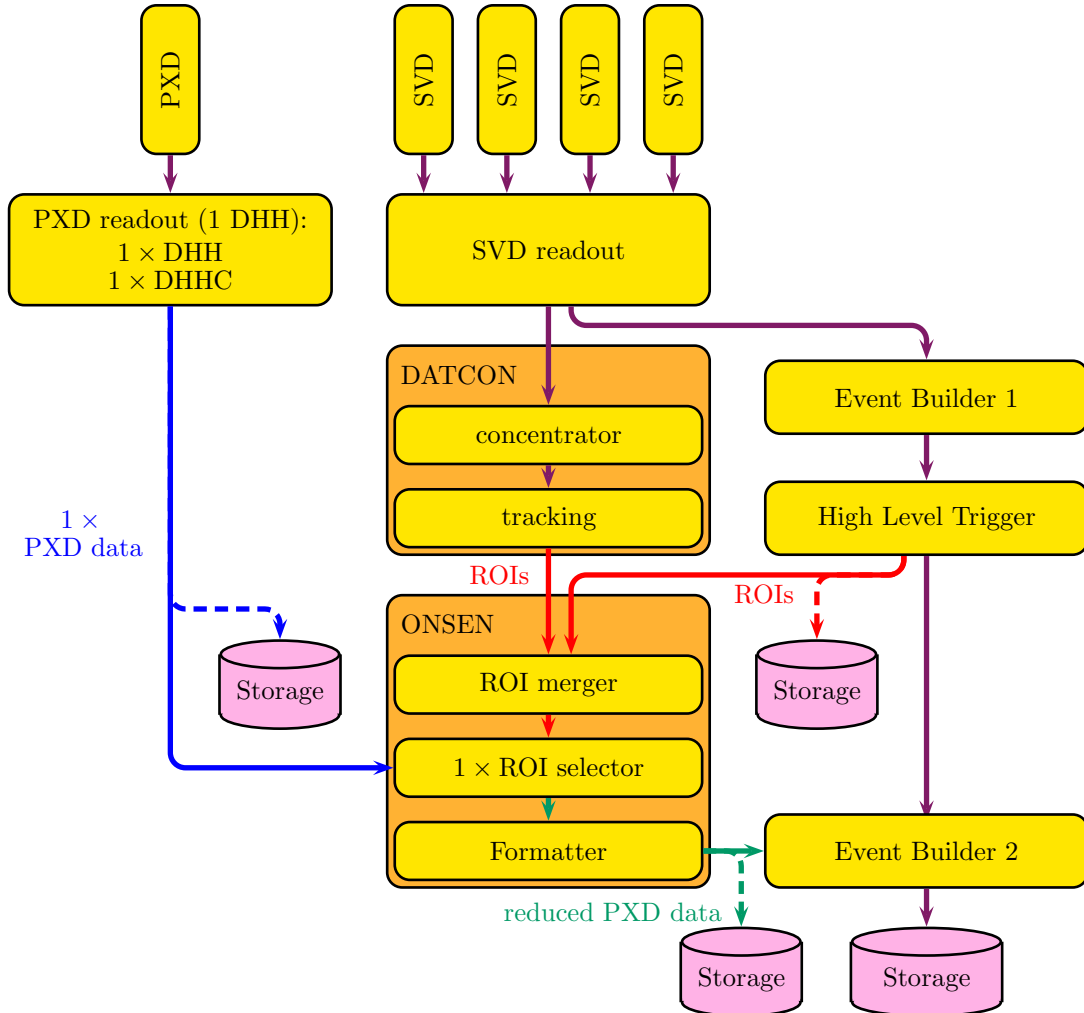
Figure 4.5.: Schematic view of the DAQ at DESY in january 2014. It is based on the final setup at KEK (figure 2.10). Here only one PXD and DHC were used to send data over one link (blue ■) to one ROI selector node to reduce the data based on the ROIs (red ■) from High Level Trigger and DATCON. The outer detectors were excluded in this test. The reduced data (green ■) were sent to the event builder via an additional formatter. To verify the ROI selection mechanism, the in- and outputs at ONSEN were recorded as well (dashed lines).

were outside of ROIs. It is also important to check that the out-sent pixel exist in the input data, or more precisely, to verify that there are no bit errors.

To support this it is important to have the data which were sent from DHC. To exclude external systems like the event builder as sources for errors, also the data stream to send out from ONSEN is interesting. For the test setup on selected runs these data were saved additional to the storage of the event builder.

4.2.1. Results of the Verification

During the whole beam test more than 20 million events were processed. At most cases a $4\,\mathrm{GeV/c}$ beam without magnetic field was used. To check different conditions and track shapes, we also varied these parameters to have different energies and magnetic fields up to $1\,\mathrm{T}$.

The final PXD sensors will have a pixel size of 250×768 (see chapter 2.3). For the test, a prototype with a reduced active pixel area of 128×480 was used.

For selected runs we included the full recording mode and saved all incoming pixel data from DHC and ROIs from HLT, as well as the output data sent to the event builder. The output data also included the full ROI frame like it was sent from the ROI Merger Node to the ROI Selector Node. In total we saved in full recording mode $1.2 \cdot 10^6$ events with altogether $4.8 \cdot 10^8$ hits.

The hitmap of a selected run (figures 4.6) contains $186\,000$ events. For debug possibilities full matrix ROIs (a single ROI covering the full sensor) were sent which are excluded in these hitmaps. As shown in figure 4.6(a), the average occupancy before reduction was $\approx\ 0.80\%$.

To reduce the data by ROI selection on the ONSEN system, HLT and DATCON were calculating ROIs. Additional the HLT was sending some ROIs covering the full PXD matrix to have the unreduced data from the sensor in data storage. In figure 4.6(b) is shown the same run as in 4.6(a), but after the ROI selection. The same $186\,000$ events produce an occupancy of $\approx\ 0.12\%$ after this data reduction. With these numbers we get a factor of 6.9 for the data reduction. This factor is strongly dependent on the size of the ROIs calculated by HLT and DATCON which is again dependent on the accuracy of the track reconstruction algorithms. This algorithm got improved during the test time.

For an illustration of the ROI selection on an earlier run was sent a fixed alternating pattern of eight different ROIs. Four were selected for a summed up hitmap (figure 4.6(c)).

All $1.2 \cdot 10^6$ events in full recording mode were checked for accuracy of the selection process. All hits inside at least one ROI got selected and sent out correctly while all hits outside those regions got rejected. As you can see in table 4.1 the cases representing a selection error were not observed in these $1.2 \cdot 10^6$ events.[59]

(a) Hitmap of recorded data stream from DHC to ONSEN. In this selected run 186 000 events were recorded with an average occupancy of ≈ 0.80%. [59]

(b) Hitmap of recorded data stream from ONSEN to event builder. The same selected run with 186 000 events and an average occupancy of ≈ 0.12% after ROI reduction. [59]

(c) Hitmap of test ROI pattern. To verify the selection process in an earlier run alternating fixed ROIs were sent. Column address is mirrored because of deactivated remapping. [59]

Figure 4.6.: Hitmaps of data before and after ROI reduction to illustrate the data reduction and the selection quality.

4.3. Quality Study of ROI Calculation Systems

To verify the quality of the ROI calculation systems we must compare the hit coordinates in PXD with the position of the ROIs (figures 4.7). With a perfect tracking the projected track should lead directly to the corresponding hit on PXD. The error of the tracking algorithm defines the ROI size. For a correct ROI calculation I have to see a line in the coordinate comparison plots for row and column. The expected line should follow the relations $row_{PXD} = row_{ROI}$ and $column_{PXD} = column_{ROI}$. Because the ROI center coordinate contains errors which are included by the ROI size (figures 4.8(a) and 4.8(b)) I observed a smearing in ROI direction and in the size of ROI (figures 4.7(a) and 4.7(b)).

Additional to the expected line in figure 4.7(a) I observed a second line with a different direction. This is the case because the HLT was sending each ROI twice. Beside the correct coordinates, it was sending the ROIs mirrored in row direction. This was implemented to check the coordinate orientations of the different sub detector components during the beam test.

74

Table 4.1.: Accuracy check of the ROI selection process. Four cases are possible where only pixel inside ROI should appear in the output data and all pixel outside ROI should be rejected. The two cases for pixel inside ROI which are rejected or pixel outside ROI which got forwarded to output data represent selection errors. cf. [59]

	Pixel inside ROI	Pixel outside ROI
Pixel in output data	OK (all selected)	OK (not observed)
Pixel not in output data	OK (not observed)	OK (all rejected)
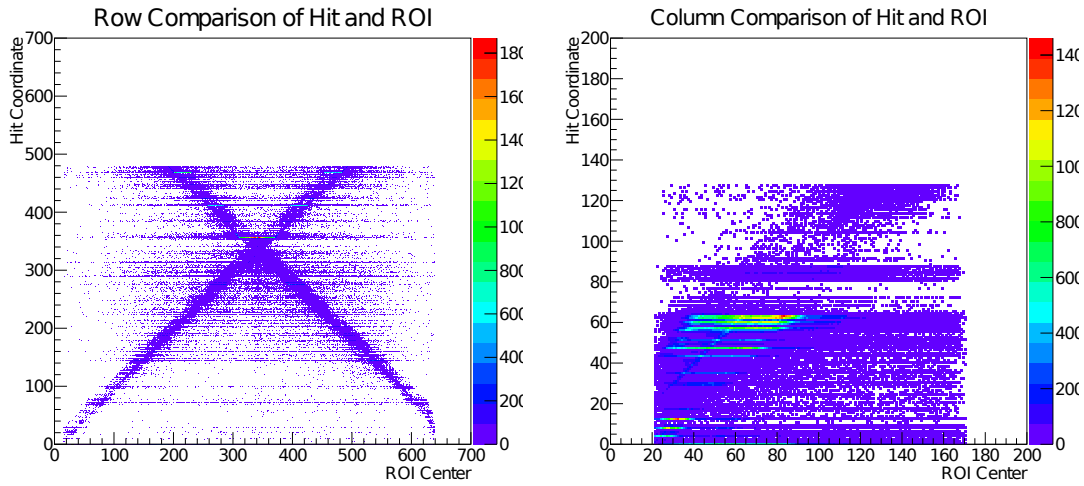
(a) Comparison of row number of PXD hit with center of ROI. The X shaped structure appears because each ROI was sent double with mirrored row coordinate.

(b) Comparison of column number of PXD hit with center of ROI.

Figure 4.7.: Comparison PXD hit and ROI center. The blurring in ROI direction of figures (a) and (b) depends on the accuracy of the track projection which affects to the ROI width (figures 4.8(a) and 4.8(b)).

4.3.1. ROI Size Analysis

The row direction describes the pixel numbering parallel to the beam direction. If we look at the size of the ROIs in this direction, we see that 90.32%[13] of the ROIs

---

[13]The exact formula for the Gaussian distribution used by Root is: $f(x) = c \cdot e^{-\frac{1}{2}\left(\frac{x-x_0}{\sigma}\right)^2}$ with mean x_0, amplitude c and standard deviation σ. With this the integral of the Gaussian distribution is: $\int f(x)dx = c|\sigma|\sqrt{2\pi}$.
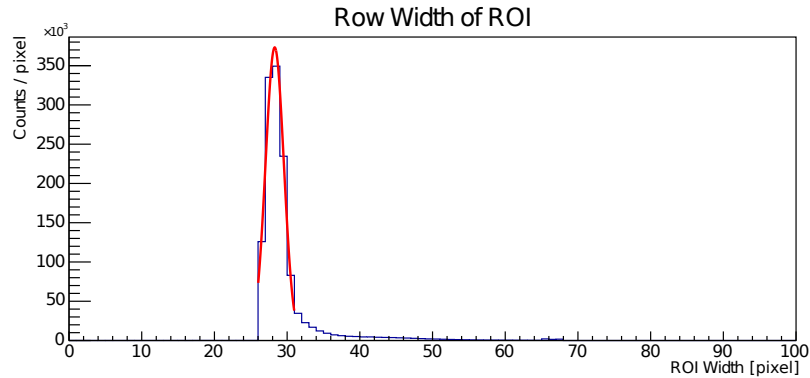
(a) ROI width in rows. In average the ROIs have a size of ≈ 28.34 pixel in row direction.
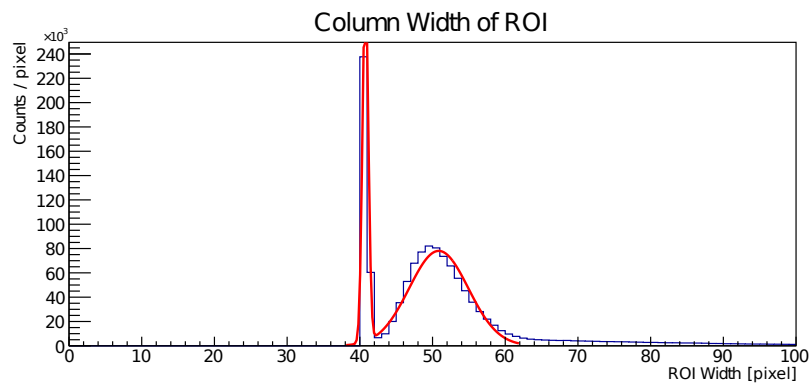
(b) ROI width in columns. In column direction we observe two different ROI sizes. A fraction has a size of ≈ 41 pixel while the others have a size of ≈ 50 pixel. The peak at ≈ 50 is caused by the hot pixels in rows between 350 and 370 (see hitmap in figure 4.6(a) and column width by row in figure 4.9(b)).

Figure 4.8.: Analysis of ROI width which is calculated by the tracking systems based on the tracking accuracy. As smaller the ROI width as better the reduction factor on the ONSEN system.

have a width of 28.290 ± 0.001 pixel with $\sigma = 1.256 \pm 0.001$ (see figure 4.8(a)). We can see in figure 4.8(a) that there is a minimum row size of 26. This result gives a assumption that there is a factor for tracking inaccuracy which is constant and an additional error which has a small variance of only a couple of pixel.

At the column width we observed two different ROI sizes. Beside the fact that there exist ROI widths in column direction of all sizes, we observed, that 61.22% of the ROIs have a width of 50.854 ± 0.005 with $\sigma = 4.070 \pm 0.005$, and 22.61% have a width of 40.767 ± 0.001 with $\sigma = 0.400 \pm 0.002$. At the column direction the shape of the data distribution gives the assumption that for about 83.83% of the cases, the width has minimum inaccuracy 40 with two different additional errors, one with a small variance and one with a wide variance.
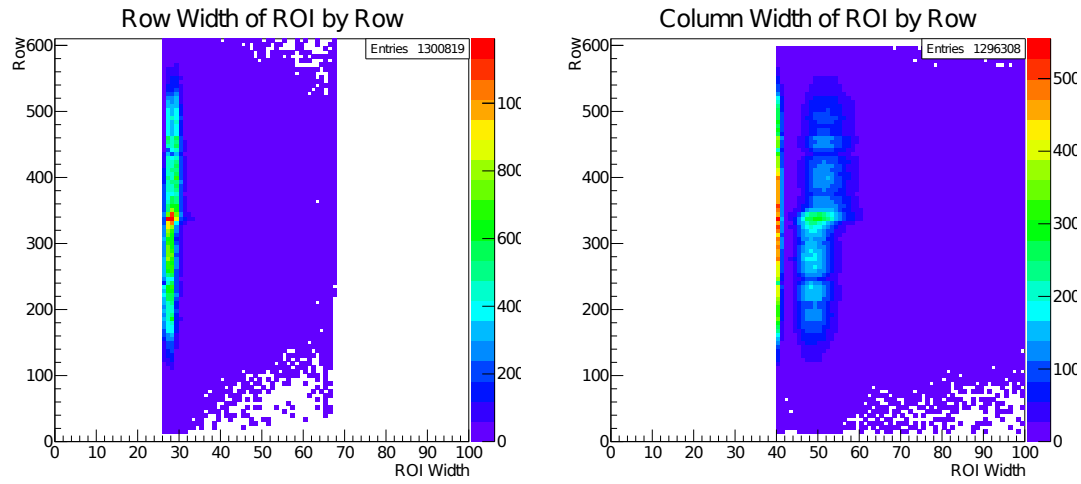
(a) ROI width in rows by row. We see that the shape of the ROI width distribution in row direction is independent of the row position. There is just an accumulation at the center of the sensor which is caused by some hot pixels in these rows. In the final experiment we would expect a dependency of the position because of the detector geometry.

(b) ROI width in columns by row. Beside the accumulation at the center of the sensor, there is a row independent distribution of column width. In the final experiment it is expected to have a isotrope distribution in this direction as well.
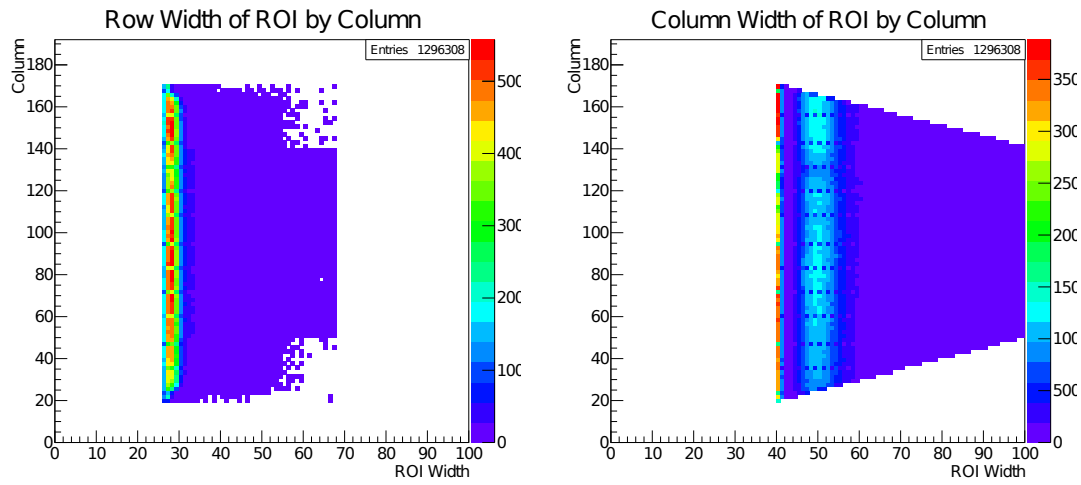
(c) ROI width in rows by column. We can observe that the row width of the ROIs is independent of the column position at the test. In the final experiment it is expected to have a isotrope distribution in this direction as well.

(d) ROI width in columns by column. It is possible to see that the shape of the ROI width distribution in column direction is independent of the column position. In the final experiment it is expected to have a isotrope distribution in this direction as well.

Figure 4.9.: Analysis of ROI width by position. Same as in figure 4.8 but spread out in row and column position. The triangle shaped cuts for the minimum and maximum position of ROIs is caused by the fact, that the ROI position is calculated by the center coordinate of the ROI, which causes that the minimum coordinate is dependent on the width.

In the figures 4.9 I show the ROI width in dependency of the row respectively column position of ROI center. At the test setup at DESY in january 2014 electrons got shot though the detector plains in an angle close to 90 degree. Because of this geometry I expect to have a mostly position independent ROI width.

The column dependency of the row width I show in figure 4.9(c) and it is mostly independent from column which is expected for the test setup. At the final setup the detector planes are placed cylindrical around the beam pipe and the column describes the radial coordinate while the row is in beam direction. I expect to have no column dependency with this geometry. In row direction I expect to have a dependency of the row width because if the ROI is closer to the forward or backward end, a particle track from the interaction point has a flat angle trough the sensor, which could cause a stretched ROI in row direction. This geometrical issue was not simulated at the test and therefore the distribution is row independent as I show in figure 4.9(a). Additionally the ROI might be stretched in any direction because of secondary vertex events. We only used electron beams in the test and didn't simulate secondary vertices.

As discussed before, the column width in the final setup shall be independent from its position as well as it was at the test setup. In figures 4.9(b) and 4.9(d) I show the position dependency of the ROI column width. A position dependency is not observed. There is only a general ROI accumulation for medium row numbers (about 350) which is caused by a hot pixel concentration at this area.

4.3.2. ROI Positioning Analysis

The ROI positioning analysis gives us a result about the accuracy of the placement. The theoretical perfect result would be that the radial distance of ROI center to hit is 0. A small offset is no problem, because the ROIs have a size which is based on the inaccuracy of the tracking algorithms. If this value is set big enough, the hit which is the reason for the selection is still inside the ROI. In the test at DESY in january 2014 we observed that in 29.15% of the cases, the distance between hit and ROI center is 17.624 ± 0.029 with $\sigma = 7.415 \pm 0.030$, while the rest forms a background distribution caused by hot pixels. With minimum ROI size of 26×40 seen in chapter 4.3.1 and the observed ROI offset from ROI center, the hit which has to be saved is still inside the region and it was no problem to have this misalignment.

If we look at the row and column dependency of the distance between ROI center and hit (figures 4.11), we can see that the Gaussian part of figure 4.10 is independent on the position. The linear patterns in the pictures are caused by the fact that some rows fire much more than others. The almost linear background in the ROI center to hit distance plot is caused by the hot pixel rows at about 350 (see figure 4.6(a)) and cause also a widespread artifact in figure 4.11(a).

An analysis of the direction of the ROI offset in figure 4.12 shows that the most of the ROIs have an offset in $\frac{\pi}{2}$ or $\frac{3\pi}{2}$ direction. These directions describe the row direction. At the beginning of the tests the geometry of the test setup was not exact measured. This got improved during the whole test period, so it might be possible
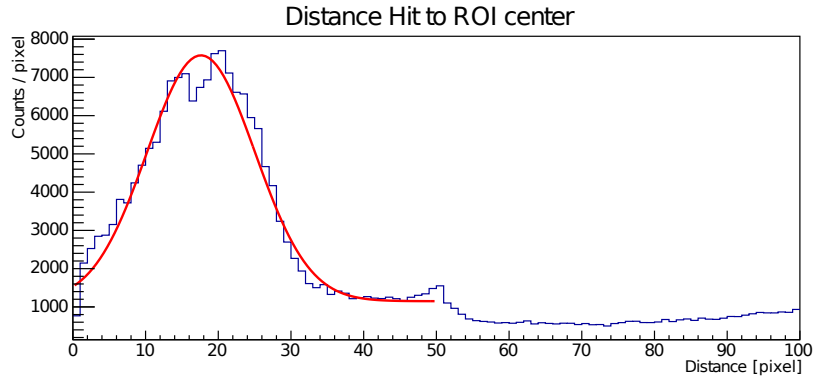
Figure 4.10.: Radial distance between PXD hits and ROI center. The radial distance is a value to estimate the quality of ROI positioning. A correct positioning would give a park at 0. The shown distance at 17.62 requires a size of the region which covers at least this radius to ensure that the hits are inside of the ROIs.
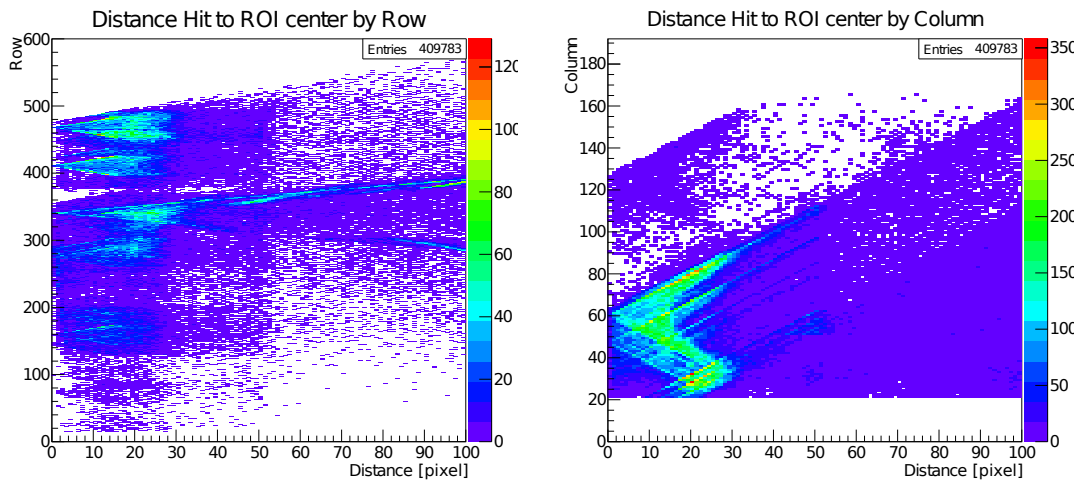
(a) Radial distance of ROI center to PXD hit by row. The high number of entries for distance over ≈ 40 and rows between 300 and 400 is caused by the hot pixel rows in this region (see figure 4.6(a)).

(b) Radial distance of ROI center to PXD hit by column.

Figure 4.11.: Distance between PXD hits and ROI center by position. The diagonal pattern has its origin in the fact that some rows and columns have much higher signals than others (see figure 4.6(a)).

ROI Offset Direction
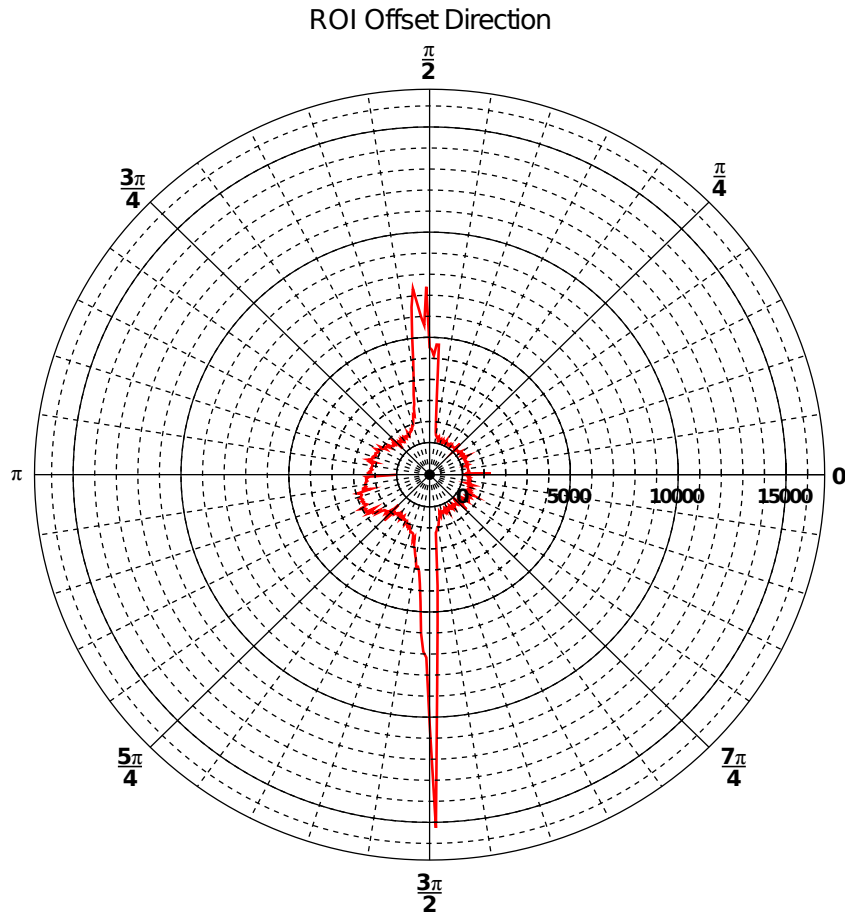
Figure 4.12.: Direction of the offset between ROI center and hit. One can see that the inaccuracy of the ROI positioning is the highest in $\frac{\pi}{2}$ and $\frac{3\pi}{2}$ direction. This describes the row direction.

that a final adjustment would have improved this result.

4.4. Conclusion for Prototype Data Reduction System

At the test setup at DESY with an integration of the full DAQ chain I successfully performed a ROI based data reduction. In full recording mode of in- and output data I analyzed $1.6 \cdot 10^6$ events containing $4.8 \cdot 10^8$ hits and observed no bit errors. The quality of the ROI calculation algorithms got optimized during the whole test period. At the last run with the full recording mode the occupancy before reduction was $\approx 0.80\%$. By ROI selection this occupancy was successfully reduced by a factor of 6.9 which gave a occupancy after reduction of $\approx 0.12\%$. I checked the data before and after selection and got the result, that all pixel were correctly selected or rejected.

CHAPTER 5

FEASIBILITY STUDY OF 6-LAYER TRACKING

To study rare decays of B mesons it is important to include the possibility of a generation of particles with very low momentum (momentum in the order of $100\,\text{MeV}/c$ or smaller) as well as the situation of a secondary vertex in the decay channel because of the lifetime of e.g. K_S^0. If for example an B meson ($5.279\,\text{GeV}/c^2$) decays in two D mesons (D^0: $1.865\,\text{GeV}/c^2$ or $D^\pm$: $1.870\,\text{GeV}/c^2$) and a kaon (K^0: $0.498\,\text{GeV}/c^2$ or $K^\pm$: $0.494\,\text{GeV}/c^2$), in the center of mass system, there is only about $1\,\text{GeV}/c^2$ left which can give a boost to the particles. In this chapter are discussed the limits of the VXD setup and the current systems to select data in the PXD system.
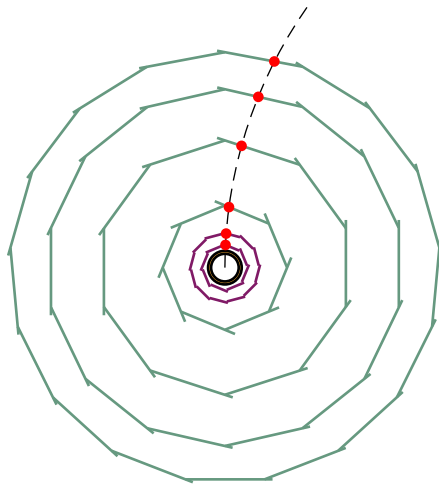
Figure 5.1.: Particle passing though VXD which is able to reach the outer detectors

5.1. Observability of Charged Particles in VXD System

In perpendicular projection[14] the radius of a particle track is proportional to its transversal momentum. If the momentum of a final decay product is small, its track can curl inside a detector setup. I case of the VXD system for transversal momentums $< 37.8 \, \mathrm{MeV}/c^2$ particles curl without reaching the CDC.

An other case is that the momentum is mostly in beam direction, which causes that the transversal momentum is very small. Those particles would be lost because they are not in the angular acceptance of $17°$ forward to $150°$ backward of the detectors. If such a final decay product has an offset caused by a secondary vertex, e.g. caused by the lifetime of a K_S^0, it can pass though some inner layer of the VXD before it leaves the acceptance of the system.

5.1.1. Charged Particles in Magnetic Field

At Belle II, as well as many other experiments in particle physics, there is a solenoid around the target region to generate a homogenous magnetic field parallel to the beam direction. If a charged particle moves through this magnetic field the Lorentz force affects to it. There are no strong electric fields inside the Belle II detector, so we can reduce the Lorentz force. cf. [69]

$$\vec{F} = q \left(\vec{v} \times \vec{B} \right)$$

Furthermore we look at the parallel and perpendicular component in relation to the magnetic field separately. For the parallel part the vector product of velocity and magnetic field is zero and therefore follows

$$\vec{F}_\parallel = q \cdot 0 = 0$$

For the perpendicular component, the particle will describe a circular path and its velocity will stay constant. To describe this path, the Lorentz force and the centrifugal force have to have the same absolute value which gives us the radius of this track by

$$\frac{m v_\perp^2}{R} = q v_\perp B \Rightarrow R = \frac{m v_\perp}{qB} = \frac{p_t}{qB}$$

Here p_t is the transversal momentum perpendicular to the beam. The combination of the circular track perpendicular to the beam and the linear component in parallel to the beam lead to a helix shaped track. With particles of charge of $e = 1.607 \cdot 10^{-19} \, \mathrm{C}$ and changing the units to electronvolt ($1.607 \cdot 10^{-19} \, \mathrm{kg \, m/s} = 0.2998 \, \mathrm{GeV}/c$) we can simplify this formula to get the momentum p in GeV/c.

$$p \approx 0.3 \cdot \frac{RB}{\cos \vartheta}$$

---

[14]If not specified differently in my reflection I use the coordinate system with magnetic field and beam in z direction. So here the term perpendicular describes the xy plane.

Here is the radius R in meter, magnetic field B in Tesla and ϑ as the angle between the track and the perpendicular plane.

If we describe a charged particle from vertex and want to know its maximum radial range from the beam line, we look at the transversal part only. The range r_{max} is then the double of the Radius R.

$$p_t \approx 0.3 \cdot RB \Rightarrow R \approx \frac{p_t}{0.3 \cdot B}$$

$$r_{max} \approx 2 \cdot \frac{p_t}{0.3 \cdot B}$$

This gives us a theoretical limit of minimum $p_{t,min}$ to reach a detector layer neglecting energy loss in the detector materials.

$$p_{t,min} \approx \frac{0.3 \cdot r_{max}B}{2}$$

5.1.2. Mathematical Limits for Helix Reconstruction

To describe a helix it is needed to know several parameters. Depending on the way to describe it, this parameters can be different. One possibility is, to use as parameters (a) the radius and (b) the center position in projection perpendicular to the helix orientation. Additional (c) the pitch, (d) a start position and (e) the helix orientation is needed. Because the magnetic field is fixed, the orientation of the helix is fixed as well. This reduces the helix definition to the first five parameters (where b is two
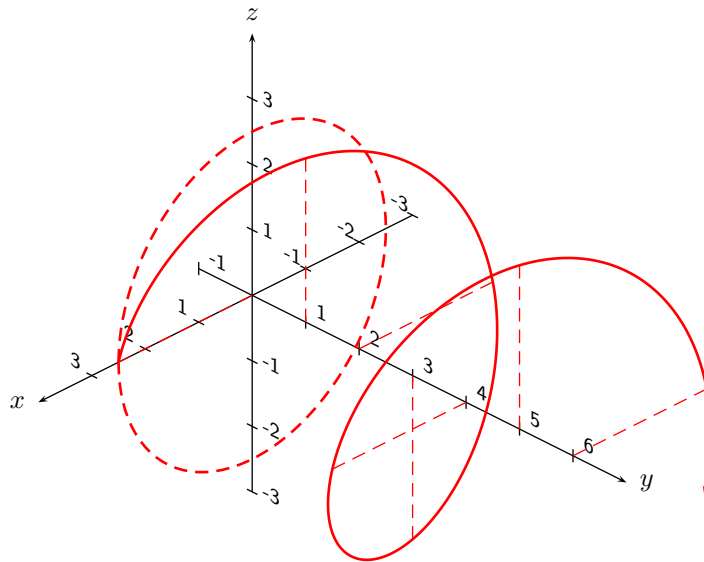
Figure 5.2.: Illustration of a helix orientated in y direction.

(a) With two hits an infinite amount of circles can be reconstructed. The correct one (purple ■) and fake tracks (green ■: four example fake tracks).

(b) With three hits the circle can be reconstructed. Alternatively for tracks from vertex it is possible to find the circle parameters using two hits and the vertex as third hit.
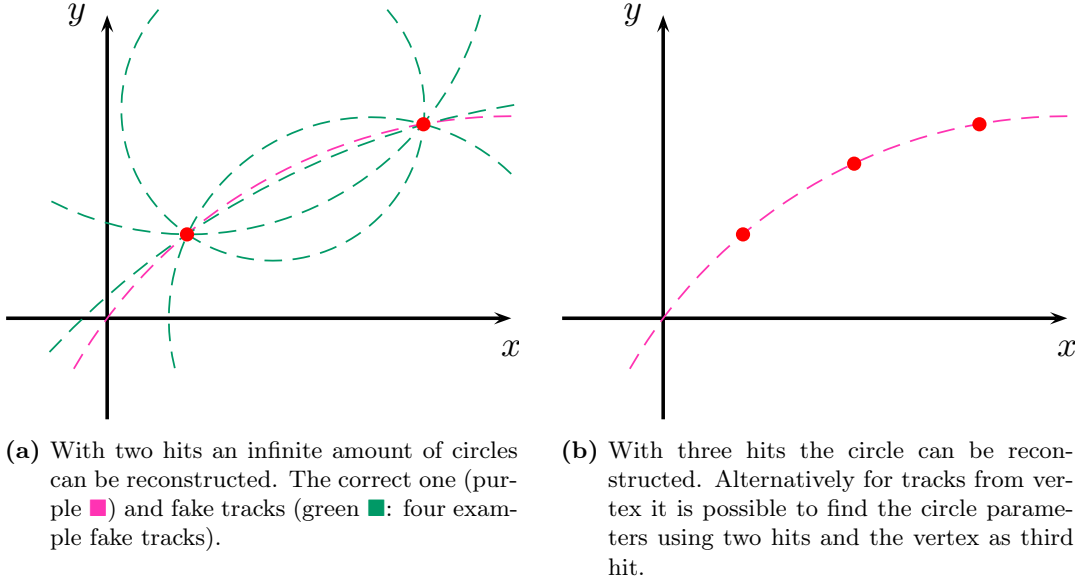
Figure 5.3.: A helix shaped track projected on a xy plane describes a circle. Here I compare the circle reconstruction based on two or three hits.

dimensional and therefore actually two parameters).

$$\vec{x}(t) = \begin{pmatrix} x_c + r \cdot \sin(2\pi \cdot t) \\ y_c + r \cdot \cos(2\pi \cdot t) \\ h \cdot t + z_0 \end{pmatrix}$$

With (x_c, y_c) as the center point, the radius r, the pitch h and z_0 as offset in z direction.

The reconstruction of a helix can be simplified in two steps. At first a circle reconstruction in the xy plane which returns the parameters for radius and center position. In a second step the parameters in z direction for pitch and start position can be reconstructed.

Perpendicular to the beam the helix has the shape of a circle, which needs for definition the center point (x_c, y_c) and the radius r.

$$\vec{x_\perp}(t) = \begin{pmatrix} x_c + r \cdot \sin(2\pi \cdot t) \\ y_c + r \cdot \cos(2\pi \cdot t) \end{pmatrix}$$

To be able to reconstruct a circle in a two dimensional plane at least three points are needed.

To be able to move from a circular track to a helix we need the description in z direction. In general the projection of a helix on a xz plane has the shape of a sinus function with the amplitude given by r.

$$\vec{x_\parallel}(t) = \begin{pmatrix} x_c + r \cdot \sin(2\pi \cdot t) \\ h \cdot t + z_0 \end{pmatrix}$$

(a) In xz projection, with known parameter of the circle reconstruction and two hits, the sinus shape in not exactly described. Beside the correct one (purple ■) there might be some fakes (green ■) found.

(b) With three hits the description is more accurate. If hits are on a helix, they describe a circle in xy plane and as well a sinus in xz projection. Certain hits can be removed from a track if they do not match this track or the whole track could be identified as fake.

Figure 5.4.: Comparison of z reconstruction with two or three hits.

For a reconstruction of the last two parameters at least two hits would be needed, but there are still multiple solutions to the reconstruction. Because we needed already minimum three hits for xy reconstruction, we can use those three also for xz direction. To use them again is possible, because the z components were not used yet. With three points multiple solutions are still possible, but the amount is much less, and with more hits it can be minimized.

5.2. Tracking Limitations in VXD

For a successful tracking in the VXD system there are some limitations. To be able to reconstruct a particle, there is needed at least three hits (chapter 5.1.2). The PXD data get reduced by the ROI reduction system (chapter 3) which causes that only hits in PXD are kept, where a corresponding track in SVD got found. Otherwise they are lost. For a further offline tracking of VXD only tracks, there are some limitations. Those particles would be very low transversal momentum particles which do not reach the outer detectors like CDC, or they pass through only a part of the detector because of a secondary vertex with a momentum mostly in beam direction.

(a) High transversal momentum particle passing though SVD. At least 3 hits in the SVD layer (green ■) needed for a possible tracking.

(b) Low transversal momentum particle passing though SVD. Lowest trackable p_t would reach inner three SVD layer (green ■) and always generates a hit.
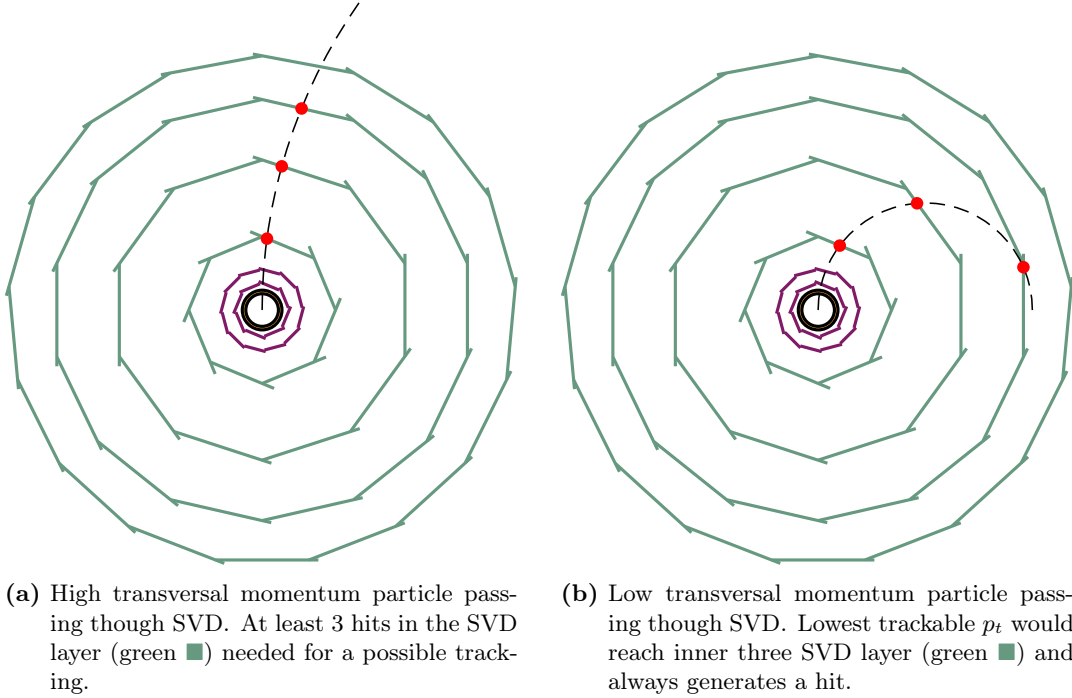
Figure 5.5.: Comparison of high and low transversal momentum particles in SVD.

5.3. Limitations with SVD

Hits in SVD are written to storage in any case as long as the event is kept. Particles which do not leave the VXD region pass maximum four layers in this detector. If the momentum is too low to reach the outer two layers of SVD, it is only possible to have two hits. For a reconstruction at least three hits are needed, so this would make it impossible to track such particles. Without a tracking, HLT or DATCON would not deliver ROIs, and the PXD hits of those particles are lost. An offline algorithm could perform a tracking including the PXD data, but this data are not available anymore in such a case.

A reconstruction of helix tracks which do not leave the VXD system is then only possible if they generate at least three hits in SVD and due to this the minimum transversal momentum is limited. Nelecting the energy loss of the particle in the detector materials, a magnetic field of $B = 1.5 \, \text{T}$ and radius of third SVD layer $r = 115 \, \text{mm}$ we get (chapter 5.1.1):

$$p_{t,min} \approx \frac{0.3 \cdot r_{max} B}{2} = \frac{0.3 \cdot 115 \, \text{mm} \cdot 1.5 \, \text{T}}{2} = 26 \, \frac{\text{MeV}}{c}$$

The particle has to pass different materials cf. [45]:

- Beam pipe
  - 50 µm gold (1.51% of X_0)[15]
  - 0.6 mm beryllium (0.17% of X_0)[16]
  - 1.0 mm cooling (paraffin) (0.21% of X_0)[17]
  - 0.4 mm beryllium (0.11% of X_0)[16]

- PXD sensors
  - 75 µm silicon per layer (0.08% of X_0)[18]
  - additional mounting material, cooling and electronics

- SVD sensors
  - 300 µm silicon per layer (0.32% of X_0)[18]
  - additional mounting material, cooling and electronics

Taking into account the different energy loss of particles in these materials and the possibility that a particle passes a sensor without generating a hit this value increases to a much higher value.

5.3.1. Tracking Improvement with PXD

By using data from PXD the tracking can be more accurate because in total it is possible to register up to six hits. Because only PXD hits in ROIs calculated by HLT or DATCON are kept, hits for track with momenta which do not reach at least three SVD layers are lost. To rescue those hits, there are two concepts: the so called cluster rescue under development by KIT (Karlsruher Institut für Technologie) and a 6-layer tracking.

---

[15]Gold: $X_0 = 6.46 \, \text{g/cm}^2$ respectively 0.33 cm [70]
[16]Beryllium: $X_0 = 65.19 \, \text{g/cm}^2$ respectively 35.28 cm [2]
[17]Paraffin: $X_0 = 44.71 \, \text{g/cm}^2$ respectively 48.1 cm [2]
[18]Silicon: $X_0 = 21.82 \, \text{g/cm}^2$ respectively 9.36 cm [2]

(a) High transversal momentum particle pass-
ing though PXD and SVD. At least 3 hits
in the SVD layer (green ■) are needed for a
possible tracking. For this a hit generating
possibility of only 50% or more is needed.

(b) Low transversal momentum particle passing
though PXD and SVD. Lowest trackable p_t
would pass the PXD layer (purple ■) and
reach only the innermost SVD layer (green
■) and always generates a hit.

Figure 5.6.: Comparison of high and low transversal momentum particles in VXD.

5.3.2. The Secondary Vertex Problem

Beside the fact that particles from the interaction point could have a small transversal
momentum and do not reach at least three layers of the SVD, there exists an other
case with track loss. If a decay contains a particle which lives long enough to leave the
interaction region, it can cause a secondary vertex. In case of an K_S^0 this can easily
reach the beam pipe wall. In this case a track hits the inner detector layer even if it
has an angle below or above the angular acceptance of 17° forward to 150° backward
(see track with red ■ hits in figure 5.7). For such a case the transversal momentum
can be high enough to reach the outer detector regions, but because of the geometry
it is not possible to hit the sensors of the outer SVD layers. In order to not lose data
of such events, the hits in PXD caused by this particles have to be rescued.
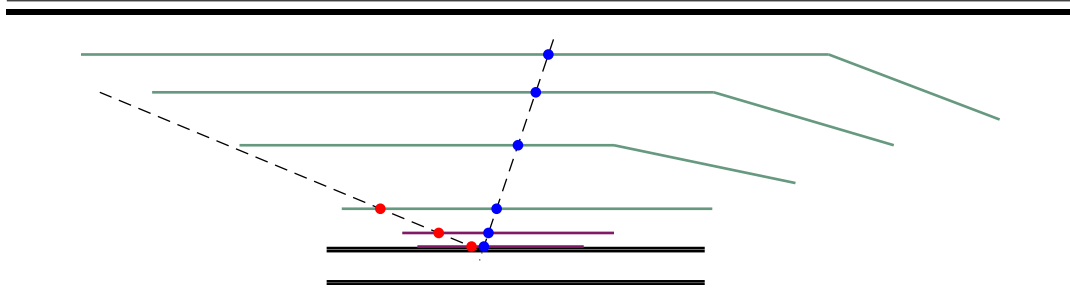
Figure 5.7.: Illustration of a secondary vertex event. A particle (dotted line) decays close to the beam pipe wall into two particles (dashed lines). One with a high transversal momentum causes hits in all six layers (blue ■). The other has a small transversal momentum compared to the component in beam direction and leaves the acceptance after three hits (red ■).

5.3.3. Energy Loss of Particles in the PXD System

Particles passing matter have an energy loss which can be described by the Bethe Bloch formula[19]. The cluster seed charge in PXD is based on such energy loss of the passing particles. In the plot shown in figure 5.8 we can see some structures which represent e.g. pions and kaons. Each particle has a range where it is minimum ionizing, which means that the energy loss has a minimum. For low momentum this energy loss increases very much. In the case of pions we can see that for energies $\lesssim 100\,\mathrm{MeV}$ the energy loss is above the threshold for the cluster rescue (see chapter 5.3.4), while for higher energies the seed charge will be too low for the cluster rescue. An idea to rescue those hits is the 6-layer tracking.

5.3.4. PXD Physics Data Rescue Mechanisms

With the ROI selection mechanisms of HLT and DATCON only data of particles are kept, fi they reach at least the SVD. To describe a helix of which the axis is fixed in beam direction, five parameters are needed (center (x_c, y_c) and radius of the helix in perpendicular plane, pitch and start direction; see chapter 5.1.2). To be able to reconstruct these parameters, at least three space points are needed. With this requirement, only tracks of particles which hit at least three detector planes are possible to find. The lowest possible perpendicular momentum p_t particles would just reach the inner three SVD layer (radius of third SVD layer: $115\,\mathrm{mm}$). Because of different energy loss of particles passing detector materials the minimum trackable p_t is different for each particle type.

---

[19]The Bethe Bloch formula describes the energy loss of charged particles passing though matter. cf. [71]
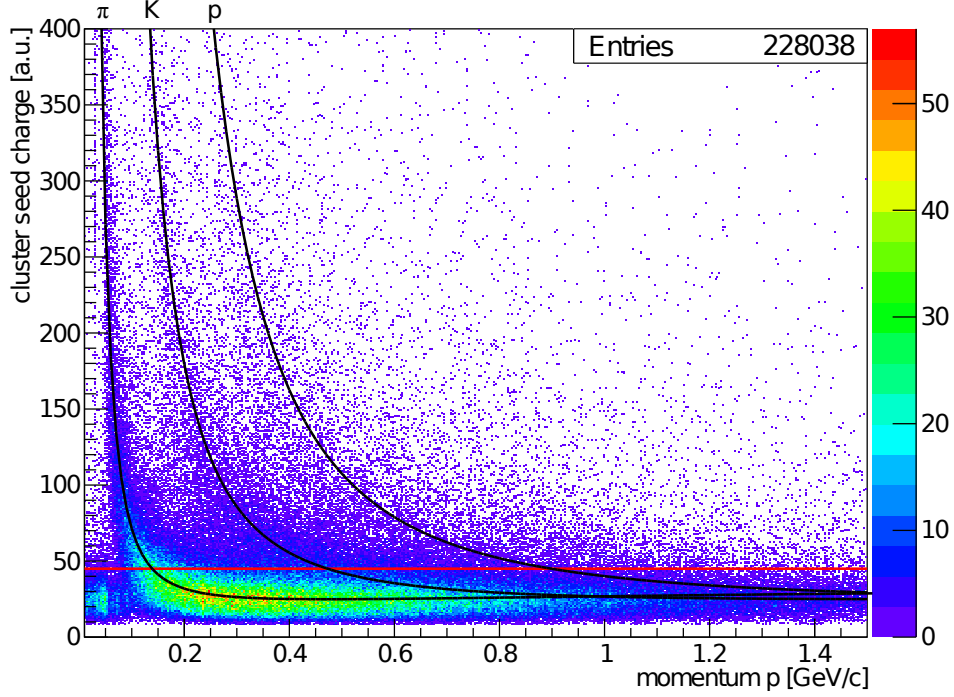
Figure 5.8.: Energy loss of particles in the PXD detector. The black ■ lines are the energy loss of charged pions, kaons and protons, calculated with the Bethe Bloch formula. The red ■ horizontal line at a cluster seed charge (see chapter Cluster Rescue on page 91) of 45 is marking the minimum ionizing value times 1.8 [72], which is the threshold for the cluster rescue system described in chapter 5.3.4.

The minimum values are:

- $K^{\pm}$: $\approx 400 \, \mathrm{MeV}/c$

- $\pi^{\pm}$: $\approx 50 \, \mathrm{MeV}/c$

- $\mu^{\pm}$: $\approx 50 \, \mathrm{MeV}/c$

- $e^{\pm}$: $\approx 30 \, \mathrm{MeV}/c$

These limits start to be a problem for decays including low momentum particles like the very slow pion in $D^{*-} \to \overline{D}^0 \, \pi^-$ in the possible decay channel of $Z_c(3900)^-$ mentioned in chapter 1.2.4. Here the transversal momentum of the slow pion is at this limit for a SVD tracking.

Because there could be the case that a particle does not effect a signal in each layer, the general conclusion is, that at least three of the four SVD layer need to show a hit, to be able to reconstruct the particle track. With additional PXD data which are selected based on the generated ROIs, the accuracy of the offline track finding

can be increased. This is possible because there may be up to six hits in the VXD per track.

Hits of lower momentum particles in SVD are kept, but the PXD data would be lost, because no ROI is created. To be able to find these very low momentum particles we need a rescue mechanism to keep possible physics data in PXD even if there is no ROI.

Cluster Rescue

A particle which passes through the PXD can generate a hit in each pixel it passes. A particle track can go though multiple pixel because of the angle it enters the sensor. Additional it is possible that a hit generates a high energy deposition in the sensor which affects also the neighboring pixel. Such a hit produces not a single fired pixel in the data but it causes signals in a cluster of multiple neighboring pixel.

A track which reaches the CDC, generates most probably many hits and a tracking by HLT is possible. Particles with low transversal momentum or secondary vertex events with geometric issues do not reach the detectors outside of VXD. They generate only hits in PXD and SVD. To keep the corresponding PXD data, the ROI algorithms of HLT and DATCON need to calculate ROIs based on the SVD data, and therefore it is required that at least three hits are generated. The additional PXD data would give more accuracy in an offline tracking which leads to more exact physics analysis.

In case that there is not enough data in SVD to perform a successful tracking, no ROIs would be sent to the ONSEN system and the corresponding PXD data are lost. To prevent this, an analysis of some parameter of the clusters in the PXD is performed. This has to be done in realtime on the unreduced data before ONSEN. Based on several properties, the clusters will be marked and can be excluded from the reduction in the ROI system. Among others, following parameters will be checked [72]:

- **Cluster seed charge:** This is the pixel with the highest ADC value in the cluster. Particles from background effects fly though the detector planes in almost any angle. A flat angle generates a long cluster with little charge in each pixel. Physics particles are coming from the vertex region and therefore do not hit the planes in a flat angle. Closer to the interaction plane the angle is almost perpendicular and clusters will be more circular shaped with a high energy deposit at the center pixel. This makes the cluster seed charge the most important value for the rescue system.

- **Total cluster charge:** The total charge of a cluster show particle hits with high energy loss in the detector. Most likely they will be on tracks of particles from the investigated decay, but also some background particles can generate such clusters. Nevertheless, it is still an important value for the system.

- **Cluster shape:** The majority of particles from background effect are electrons and photons. These particles mostly generate only small and long clusters

because of flat angles. Therefore the cluster shape is an other interesting value.

- **Hit Position:** Particles from interaction point hitting the detector layers close to the interaction point plane have an almost perpendicular angle to the sensor, while the angle at front and back end is quite flat. Selections on e.g. cluster shape or seed charge have to check the position as well, because these values are strongly dependent on the impact angle.

6-Layer Tracking

An additional concept would be a 6-layer tracking. If a helix tracking would use also the unreduced data from PXD, the minimum p_t to be able to track would be much lower. Particles only need to hit both PXD layer and the innermost SVD layer with a radius of only 38 mm. With this we could lower the limit of minimum trackable p_t by a factor of ≈ 3 because of the smaller helix radius needed to reach these layers. For particles below the minimum ionizing momentum the energy deposition in the PXD is high enough to cause a charge above the threshold of the cluster rescue system. These thresholds are:

- $K^{\pm}$: $\approx 130 \, \text{MeV}/c$

- $\pi^{\pm}$: $\approx 17 \, \text{MeV}/c$

- $\mu^{\pm}$: $\approx 17 \, \text{MeV}/c$

- $e^{\pm}$: $\approx 10 \, \text{MeV}/c$

Hits of tracks in PXD which are not above the thresholds of the cluster rescue system would be still lost and the physics in this event as well. A concept to keep also these hits would be a tracking, based on the unreduced data of the six VXD layers (therefore called 6-layer tracking). Because of mathematical limits, theoretically tracks with at least three hits in this six VXD layers would be found. The minimum requirement in transversal momentum for a 6-layer tracking would be to reach at least the inner three layers. Such an algorithm could find hits of low momentum tracks which are not found by the cluster rescue yet, as well as hits from secondary vertex track which reached just the inner layers before leaving the acceptance. In general for particles which pass through up to all layer only need to generate hits in three of the six layer. Compared to SVD tracking, where hits in 75% (3 of 4) of the layers are needed, here it is only a ratio of 50% (3 of 6). Because of the high occupancy of 3% in the inner PXD layer generated by background effects, the tracking will be computationally intensive and has to be investigated in further studies.

For the example of slow pions in the a $Z_c(3900)^-$ (out of B) decay over $D^{*-} \to \overline{D}^0 \, \pi^-$ the tracking efficiency can increase. If they are minimum ionizing, they cause a hit, but the charge is too low to get rescued by the cluster rescue (the cluster revue has a threshold of minimum ionizing times 1.8). They would usually reach the outer detectors, but in case of a displaced vertex (e.g. K_S^0 decays; see chapter 1.2.2) the

might leave the acceptance after some hits. In this case a 6-layer tracking could rescue hits which are not covered by other mechanisms. In chapter 5.4 the measurement of pions from displaced vertex is discussed.

5.4. Charged Pions from K_S^0

As already described in chapter 1.2.2, in Belle II the production vertex of K_S^0 has almost no offset from interaction point because of short lifetime of the mother particles of the kaon (e.g. $B^\pm$: $c\tau = 492.0\,\mu m$, $D^\pm$: $c\tau = 311.8\,\mu m$ cf. [2]). The mean lifetime of the K_S^0 of $\tau = (8.954 \pm 0.004) \cdot 10^{-11}$ s cf. [2] is long enough to leave the interaction point ($c\tau = 2.6844\,cm$ cf. [2]), but they are still inside the VXD system (figure 5.9).

To investigate the situation of pions from K_S^0 at Belle II, I simulated inclusive B decays from $\Upsilon(4S)$. These decays contain often one or sometimes multiple K_S^0 (e.g. $\mathcal{B}(B^0 \to K^0 \mathrm{anything}) = (78 \pm 8)\%$ cf. [2]) which decay in over 99.7% into two pions. These pions were checked if they hit the detector planes in VXD and based on the hits it was checked whether it will be possible to track those particles for a ROI calculation or to rescue the hits in PXD with the cluster rescue.
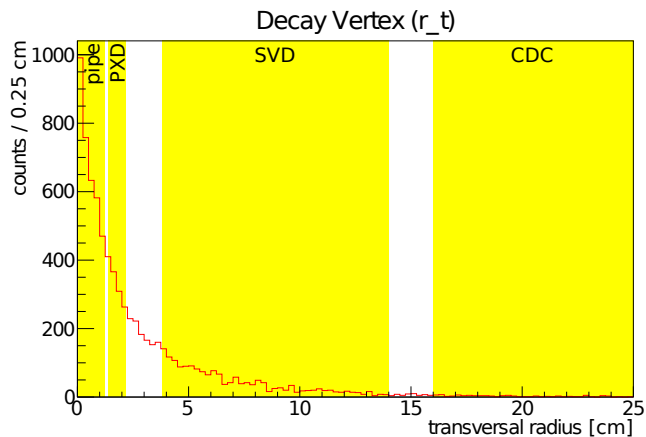
Figure 5.9.: Radial distance r_t of decay vertex of K_S^0 to the interaction point. Because of the long lifetime of the K_S^0 the decay vertex reaches easily the beam pipe $(1.0 - 1.2\,cm)$ but still stays inside the VXD $(14.0\,cm)$. The yellow ■ areas show the radii to reach or pass the beam pipe or the the inner most detectors.

The pion p_t distribution of simulated hits in the VXD system can be seen in figure 5.10. Separated for the six detector layers we can see in figure 5.11 that the general shape of the pion p_t distribution of the hits in each layer is similar in each layer. A difference we can see is that the total number of hits in the inner layer is much less than in the outer layers. The reason for this appearance is the position of the decay vertex of the K_S^0 as shown in figure 5.9. The most kaons pass the PXD area but only a very little ratio get until the outer SVD area, so it explains why there is a high hit

93
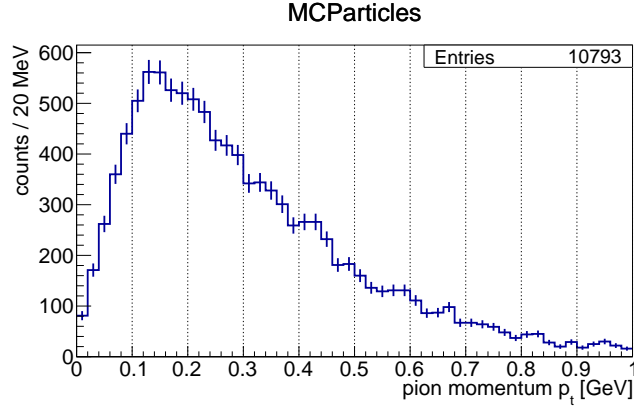
Figure 5.10.: p_t distribution of charged pions from K_S^0 in the simulated decay inclusive B decay from $\Upsilon(4S)$.
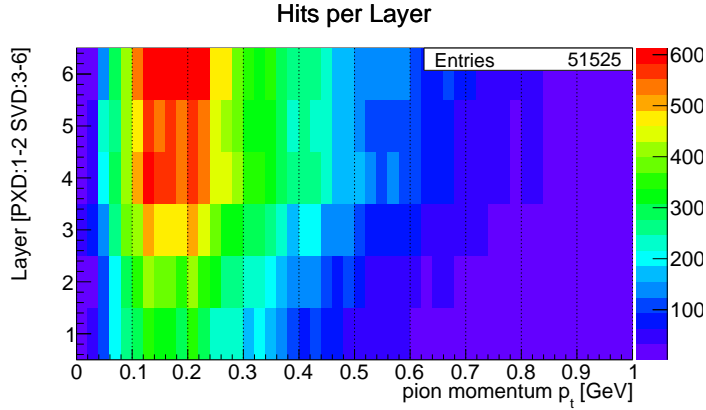
Figure 5.11.: p_t distribution of the hits caused by pions from K_S^0 on the VXD layers. The lower number of hits in the PXD layers $(1, 2)$ is caused by the fact that K_S^0 can pass the PXD layers before they decay (see figure 5.9).

count in all SVD layers but a much smaller in the PXD.

5.4.1. Example Events for K_S^0 Decays Generating a Secondary Vertex

To illustrate the situation for decays with secondary vertex, in this chapter three examples are chosen to see how the two recovery systems can help rescuing data which otherwise would be lost. In table 5.1 are shown the cluster charges and seed charges caused by pions from K_S^0 together with the transversal momenta. In the following the situation in the three events is described in detail. The events are chosen for one case where the 6-layer tracking is needed for both tracks (event A),

a case where HLT and cluster rescue manage everything (event B) and a combined case with one track by cluster rescue and one by 6-layer tracking (event C).

Table 5.1.: Cluster charges of pions in the three example events in figures 5.13, 5.14 and 5.15. With a seed charge threshold of 45, in event A the π^- hit in the inner layer would be saved by the cluster rescue. In event B in the outer layer the pi^- has a seed charge above the threshold and in event C all hits of the π^+. Here the π^+ generates two hits in the inner layer because it passes the overlapping region of two sensors.

event	track	layer	cluster charge	seed charge	p_t
A	40	L1	72	26	$89\,\mathrm{MeV}/c$
		L2	85	41	π^+
	41	L1	47	47	$292\,\mathrm{MeV}/c$
		L2	21	13	π^-
B	67	L1	40	22	$281\,\mathrm{MeV}/c$
		L2	29	14	π^+
	68	L1	81	34	$66\,\mathrm{MeV}/c$
		L2	59	55	π^-
C	47	L1	262	132	$48\,\mathrm{MeV}/c$
			296	140	π^+
		L2	398	251	
	48	L1	39	20	$771\,\mathrm{MeV}/c$
		L2	31	21	π^-

Event A

In this decay channel the K_S^0 decays into two pions (red ■ in figure 5.12(a)). A low π^+ with $89\,\mathrm{MeV}/c$ and a π^- with $292\,\mathrm{MeV}/c$. As one can see in figure 5.13 both pions generate only three hits, two in PXD and one in the innermost SVD layer. The reason why the pions do not generate more hits are different between the two cases. Because of the secondary vertex and a momentum mostly in backward direction, the π^+ leaves the acceptance after three hits. The π^- passes through the first three layers and generates hits. At the fourth layer (second SVD layer) it interacts with the detector material and ends without an additional hit. In total both tracks generate only three hits which means they would be lost with a HLT / DATCON only solution. With the cluster rescue, the innermost hit of the π^- would be recovered but this is still not enough to reconstruct the event. With a 6-layer tracking the other three missing hits could be rescued which would make it possible to reconstruct the whole event.

Event B

Here the decay channel contains two K^0_S and both decay into two pions. Here I discuss the possibility for a reconstruction of the red ■ marked in figure 5.12(b). The π^+ with a momentum of $281\,\mathrm{MeV}/c$ reaches the CDC and generates enough signals to make it possible to run a tracking on HLT. Here the corresponding hits in the PXD would be saved by the basic ROI selection. For the π^- with a momentum of $66\,\mathrm{MeV}/c$ we have again the situation that it leaves the acceptance. It generates two hits in PXD and two hits in SVD. The SVD hits are not enough for a tracking so nor ROIs would be generated, but for the outer PXD layer the seed charge is above the threshold so the cluster rescue can save a third hit for this track and a tracking ID when possible. A 6-layer tracking can improve the accuracy by rescuing also the inner layer hit, but the general possibility of a reconstruction is already given by HLT together with the cluster rescue.

Event C

In this event the K^0_S decays in two pions as well. The π^+ with $48\,\mathrm{MeV}/c$ is below the minimum ionizing region so the seed charge in PXD is above the threshold and both hits will be covered by the cluster rescue. After all, five hits will be saved and an offline tracking is possible even without tracking in HLT or DATCON. After the second SVD hit this pion reacts with the detector material and the track ends. This example shows also a possible track going through the overlap region of two PXD sensors, which generates two hits in one layer. The direction and momentum of the π^- is with $771\,\mathrm{MeV}/c$ high enough to reach the CDC, but after one SVD layer it reacts with the detector material and gets a kink. This causes that the original pion has only three hits. To reconstruct its track, the PXD hits need to be saved by the 6-layer tracking, because their seed charge is below the cluster rescue threshold.

(a) Complete decay in event A.

(b) Complete decay in event B.

(c) Complete decay in event C.
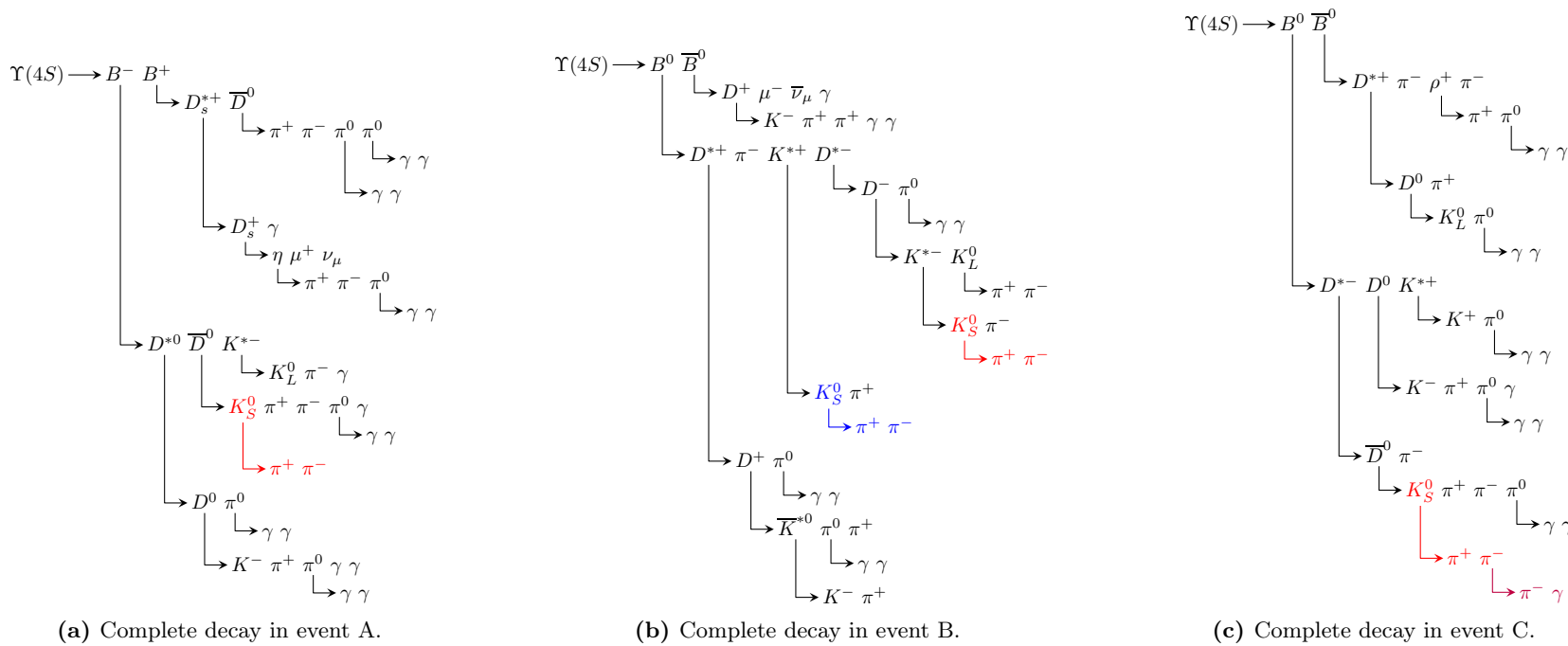
Figure 5.12.: Decays for the event display pictures 5.13, 5.14 and 5.15.
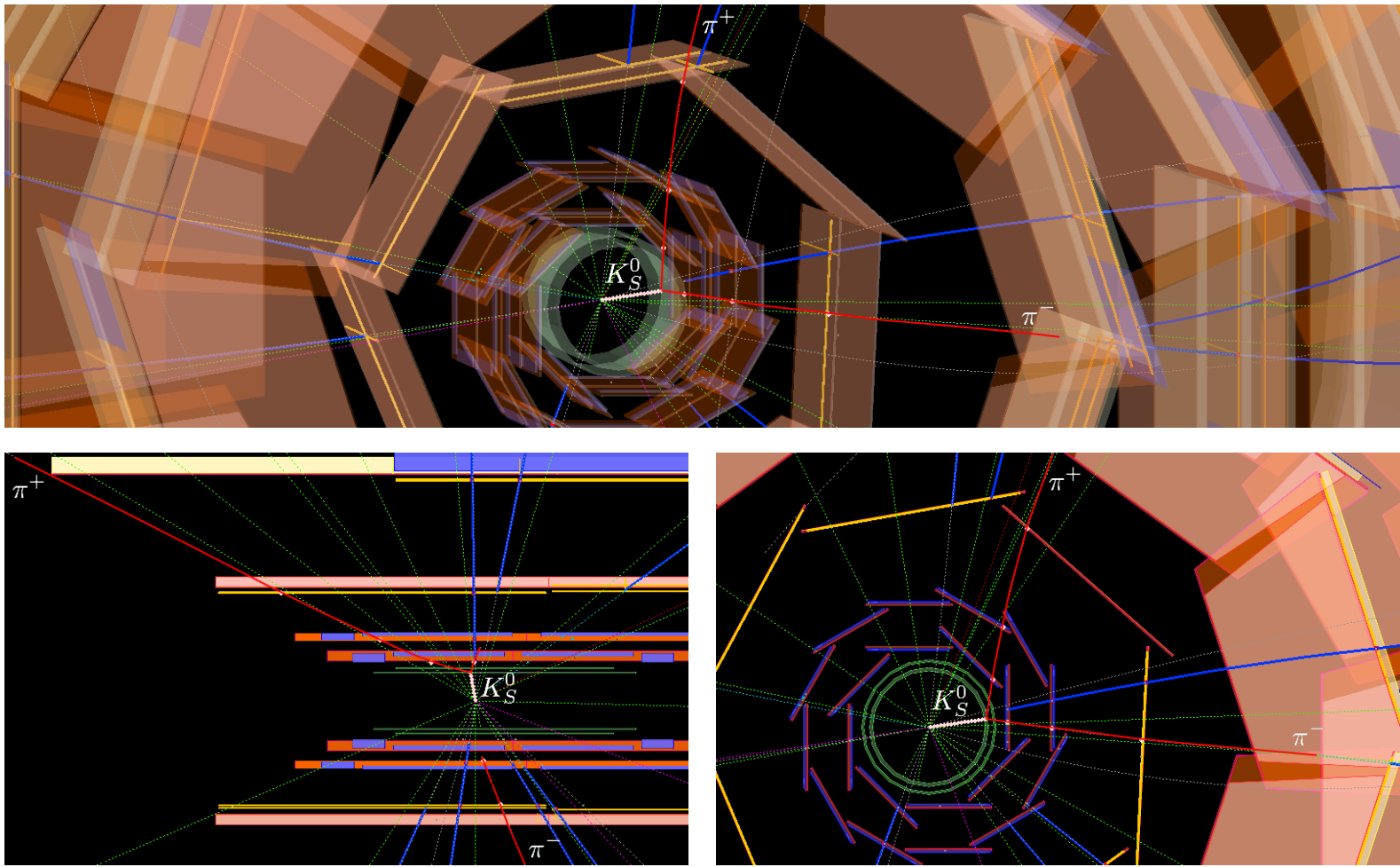
Figure 5.13.: Event display of event A. The highlighted K_S^0 decay is an example for a decay where both pions are only reconstructable with 6-layer tracking.
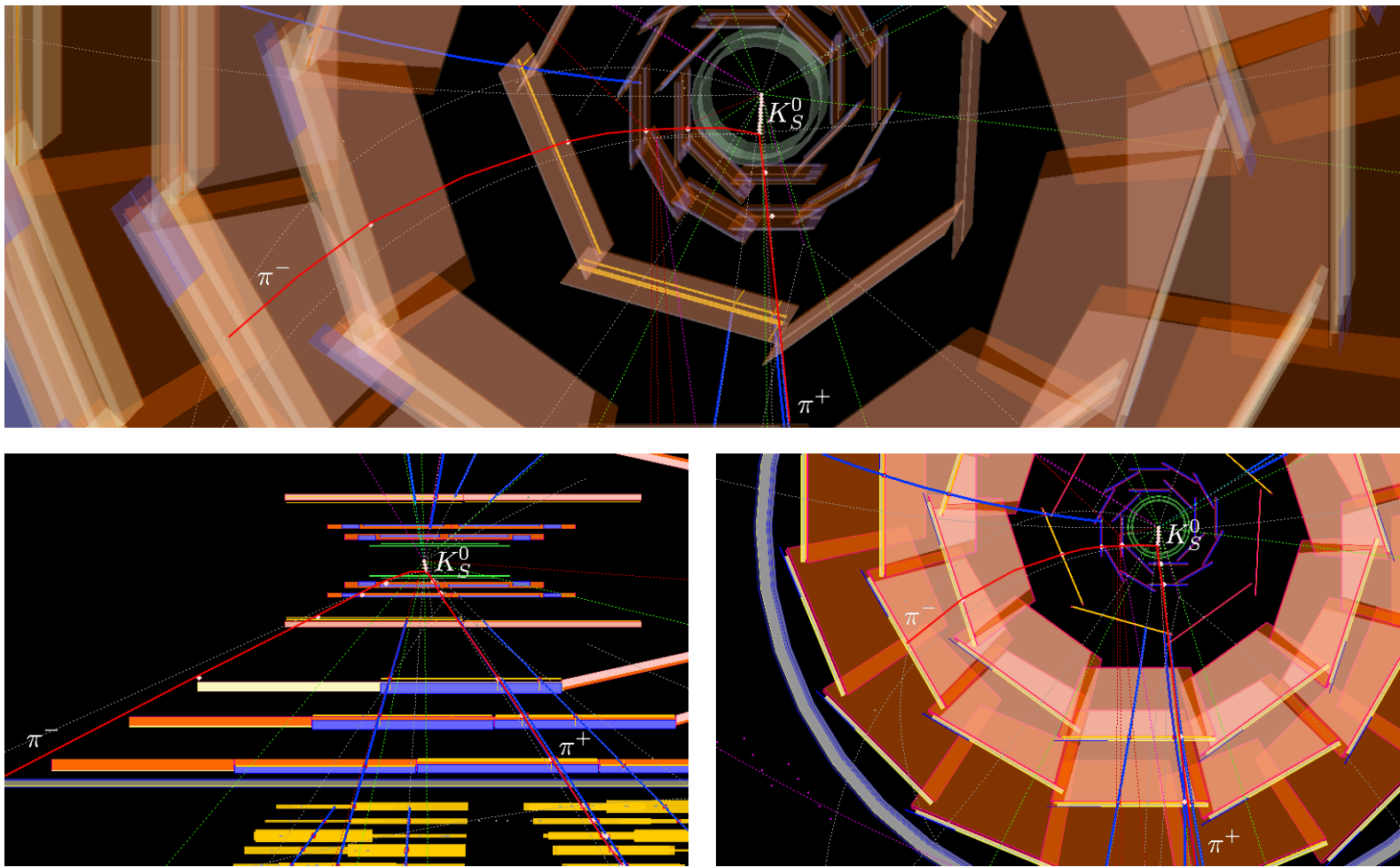
Figure 5.14.: Event display of event B. The highlighted K_S^0 decay is an example where one pion (π^+) is trackable with HLT and the second pion (π^-) is reconstructable with the cluster rescue data. A 6-layer tracking could improve the accuracy for the offline analysis.
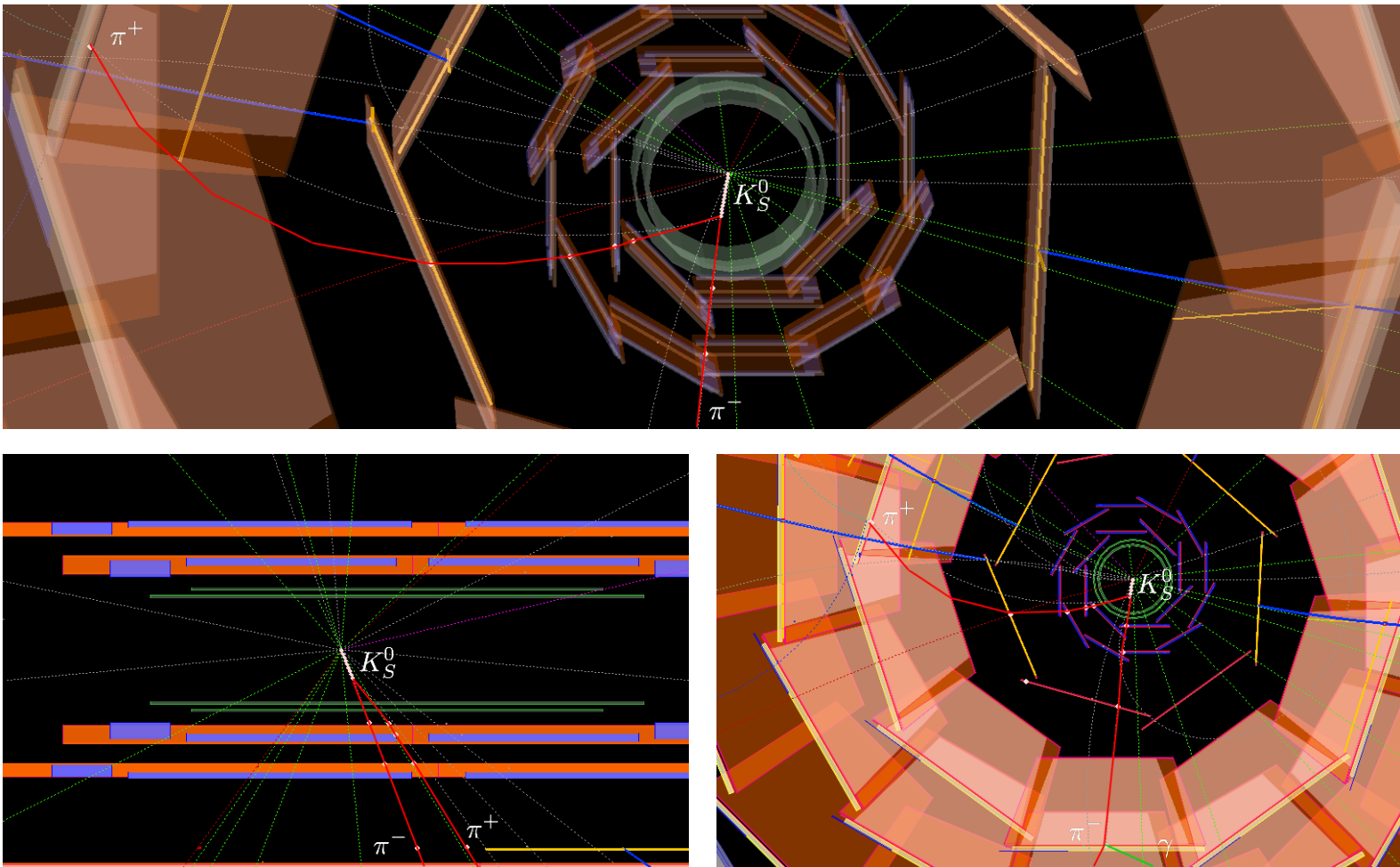
Figure 5.15.: Event display of event C. The highlighted K_S^0 decay is an example where π^+ will be rescued by the cluster rescue and the π^- can be rescued by a 6-layer tracking.

5.4.2. Analysis of the Pion Trackability with the Different Setups

For a study to check the feasibility of a tracking in the VXD by the different tracking systems it is important to check the number of hits in the different detector parts. For a tracking by HLT or DATCON only the hits in SVD can be used. In figure 5.16(a) one can see that the most pions from K_S^0 cause hits in four layers. For those pions it is possible to reconstruct the track and generate corresponding ROIs. The interesting part for additional rescue systems are those which have less than three hits. For those tracks the information in PXD would be lost after the ROI selection, because of non existing ROIs and rescue systems have to save those data. In figure 5.16(b) we can see that there is a reasonable amount of tracks with three hits in whole VXD. Those could be rescued by a 6-layer tracking, even if they have less than 3 hits in SVD or only small cluster charges in PXD (not covered by cluster rescue). The big amount of pions with no hits in the whole VXD (bottom row in the plots) is caused by geometric reasons. The simulated pions fly to all directions, but close to the beam pipe in forward ($< 17°$) a backward ($> 150°$) direction they leave the acceptance of the detectors.

As we can see in figures 5.17 and 5.18 of all pions (red ■) the most are already theoretical trackable by the HLT / DATCON systems (green ■). The theoretical prediction is done by the fact that a tracking would need at least 3 hits for a helix reconstruction. The tracking efficiencies of the systems is not considered in these calculations, because we want to check the possibilities of a future 6-layer tracking which is not existing yet, so we cannot predict any efficiency for this system. To have a comparison with equal conditions for all systems the calculations are done for the theoretical possibilities. With these conditions a cluster rescue was added to the HLT tracking possibility. The cluster rescue is based on > 1.8 of minimum ionizing which leads to an ADC value of > 45 for the seed charge. A trackable pion including cluster rescue is counted as soon as the number of hits in SVD together with the rescued clusters is at least three. This is needed to be able to successfully perform an offline tracking on the recorded data. The number of pions with this setup increase a bit (blue ■) as well as for a setup with HLT / DATCON with 6-layer tracking (purple ■).
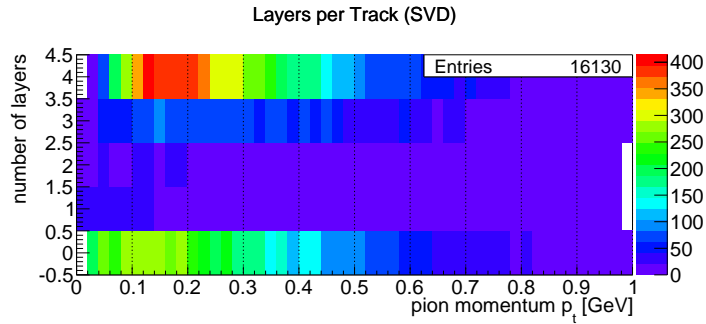
(a) Number of PXD and SVD layers with hits for a track for different p_t. Tracks with hits in three or four layers are trackable by the algorithms of HLT and DATCON which is the case for the most tracks, but tracks with less hits would be lost.
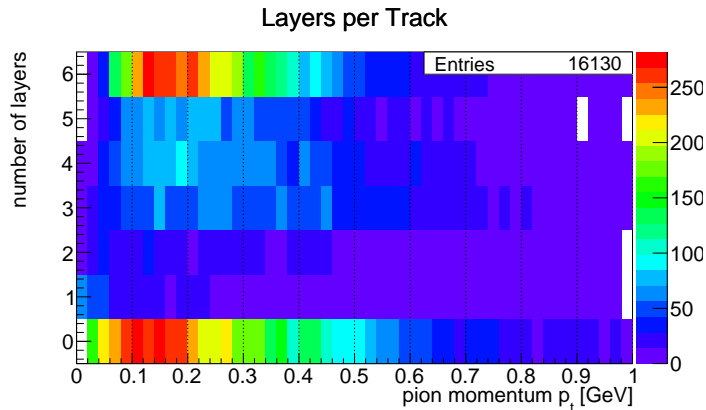
(b) Number of VXD layers (PXD+SVD) with hits for a track for different p_t. The majority of tracks have hits in all layers or in none. Tracks with no hits are e.g. caused by the angular acceptance ($17°$ forward to $150°$ backward). Tracks with hits in at least three VXD layers eve if they have less hits in SVD can be rescued by a 6-layer tracking while they are not covered by the algorithms of HLT and DATCON.

Figure 5.16.: Number of layer with hits by transversal momentum.
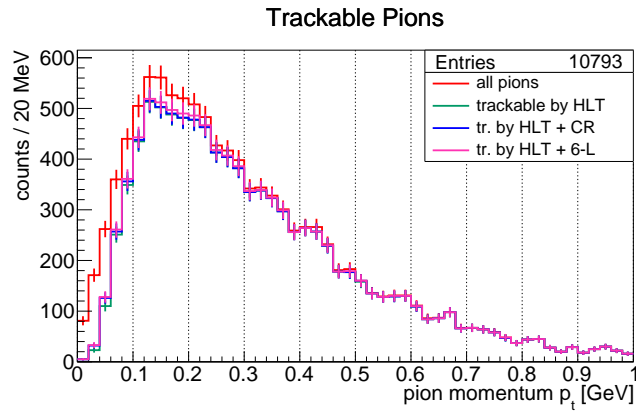
(a) Combined view of all pions (red ■) with the trackable pions (green ■, blue ■ and purple ■ line). The lines for trackable pions overlap, therefore take a look at the single plots in figures 5.17(b), 5.18(a) and 5.18(b).
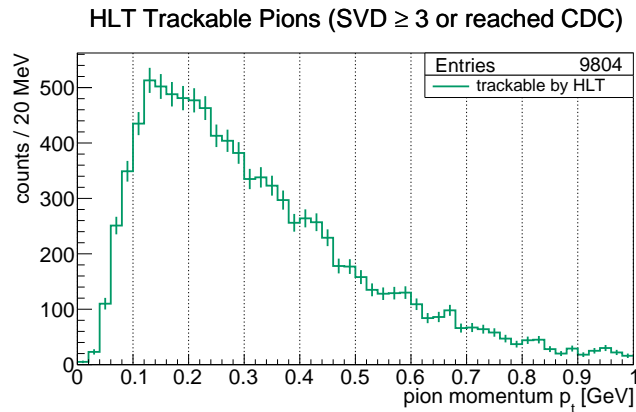
(b) Trackable pions with HLT or DATCON for different p_t. Requirement is at least three hits in SVD or any hits in CDC.

Figure 5.17.: Trackable pions for different p_t (combined and HLT; cluster rescue and 6-layer tracking in figure 5.18).
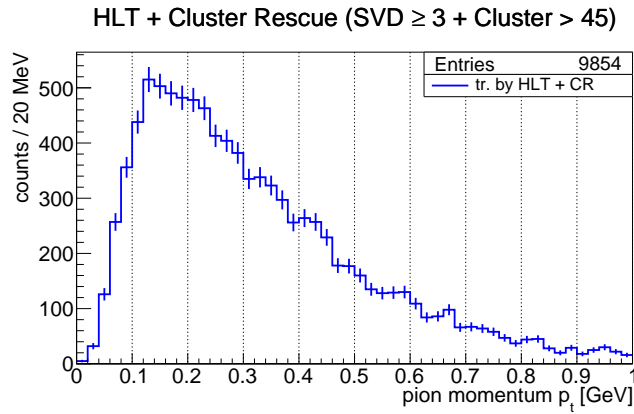
(a) Trackable pions with HLT, DATCON and additional the cluster rescue system for different p_t. Requirement is at least three hits in SVD together with rescued hits (seed charge > 1.8 of minimum ionizing which corresponds to an ADC value of > 45).
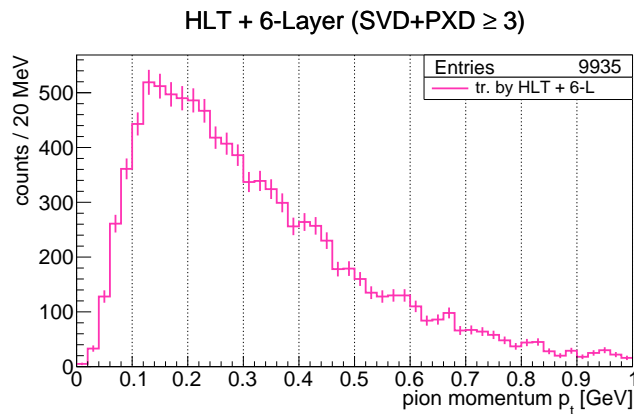
(b) Trackable pions with 6-layer tracking for different p_t. Requirement is at least three hits in SVD together with PXD.

Figure 5.18.: Trackable pions for different p_t (cluster rescue and 6-layer tracking; combined and HLT in figure 5.17).

5.4.3. Maximum Tracking Feasibility of Pions from K_S^0

For a better visualization of the increment of the tracking efficiency, in figures 5.19 the same data are normalized on the number of pions. In figure 5.19(b) one can see that for small momenta ($\lesssim 100\,\text{MeV}$) the cluster rescue as well as a 6-layer tracking can cover up to additional $\approx 7\%$ of the pions for momenta of $\approx 50\,\text{MeV}$. For momenta above this, the pions are in the area of minimum ionizing particles (see figure 5.8) as discussed in chapter 5.3.3. In this area the seed charge is below the threshold and the cluster rescue cannot recover those hits. Their momenta are high enough to reach the CDC, so there would be enough information to have ROIs and to find the pion offline in the recoded data. Because of geometric issues with secondary vertices (see chapter 5.3.2), they can leave the acceptance before generating at least 3 hits in the SVD. With a 6-layer tracking it is possible to track those particles and for certain momenta it increases the trackability with up to $\approx 2\%$.

In total, 10000 decays of $\Upsilon(4S)$ into two B mesons were simulated. In those decays 10793 pions from K_S^0 were included. These K_S^0 can decay e.g. into two as well as in three pions. The number of K_S^0 also varies, so more than one K_S^0 or none is possible. A detailed view about the tracking enhancement with cluster rescue and 6-layer tracking is shown in table 5.2.

Table 5.2.: Check of the tracking possibilities for the different systems. The percentage values are counted over all simulated pions from K_S^0 in all momenta. Total number of simulated pions from K_S^0 is 10793.

at least 3 hits in	HLT / DATCON only SVD or reach CDC	with cluster rescue SVD plus rescued cluster	with 6-layer tracking SVD with PXD
number of trackable pions	9804	9854	9935
ratio of trackable pions	90.84%	91.30%	92.05%
increment to HLT / DATCON cluster rescue		0.46%	1.21% 0.75%
max. incr. to HLT / DATCON **cluster rescue**		$\approx 7\%$ (at $p_t \approx 50\,\text{MeV}$)	$\approx 7\%$ (at $p_t \approx 50\,\text{MeV}$) $\approx 2\%$ (at $p_t \approx 200\,\text{MeV}$)
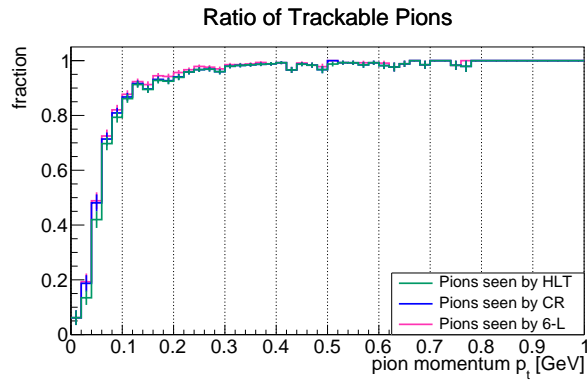
(a) Possible efficiency for a pion tracking with the three different setup options. The three lines overlap. In figures (b) and (c) is shown a differential plot between the shown ratios.
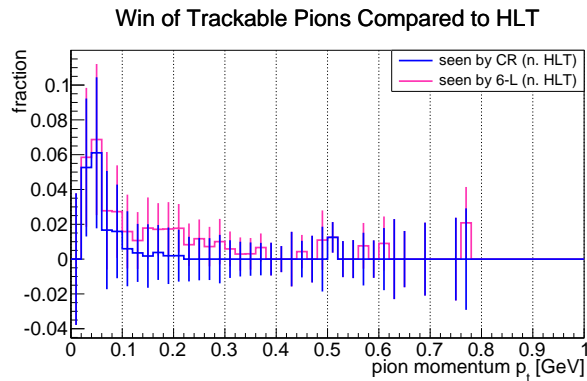
(b) Possible efficiency enhancement for a pion tracking with cluster rescue or 6-layer tracking compared to the HLT / DATCON only option.
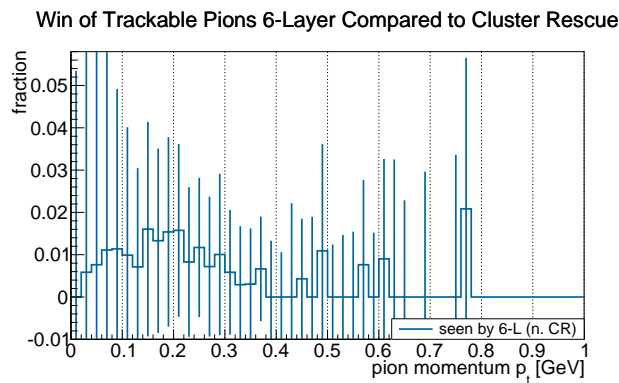
(c) Possible efficiency enhancement for a pion tracking with 6-layer tracking compared to cluster rescue.

Figure 5.19.: Tracking potential for a pion tracking and the increment of efficiency by adding cluster rescue and 6-layer tracking.

5.4.4. Momentum Distribution of the Pions Tracked by the Different Systems

To see at which total momentum p the cluster rescue and a 6-layer tracking works the best, I was analyzing the momentum distribution of the pions with the different systems. As we can see in figure 5.20(a) and 5.20(b), because of the high trackability of the most pions, these two plots are quite similar. If we look especially to those pions found by the cluster rescue but not by the HLT / DATCON (figure 5.21(a)), we see that the cluster rescue mostly rescues low momentum pions, fitting to the energy loss check in chapter 5.3.3. In figure 5.21(b) we see pions which could be found only by 6-layer tracking, and we can see that it can rescue the minimum ionizing particles, which are not covered by the cluster rescue.
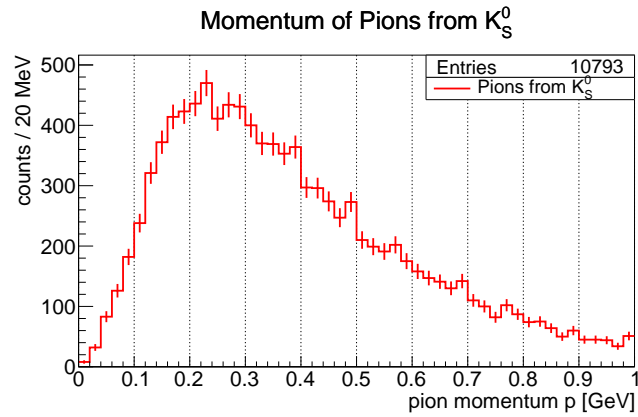
(a) Momentum distribution of all pions from K_S^0.
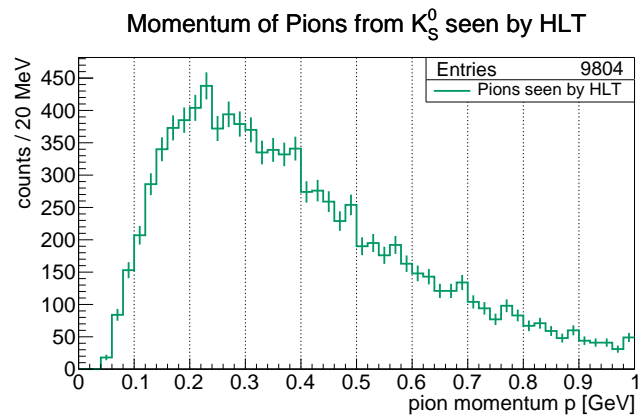
(b) Momentum distribution of HLT or DATCON trackable pions from K_S^0.

Figure 5.20.: Momentum distribution of pions from K_S^0 (all and HLT; cluster rescue and 6-layer tracking in figure 5.21). Because the most tracks have enough hits for the HLT and DATCON algorithms, also the most tracks are found. There is only a difference between the plots (a) and (b) for small momenta. These are subject of interest for cluster rescue and 6-layer tracking.
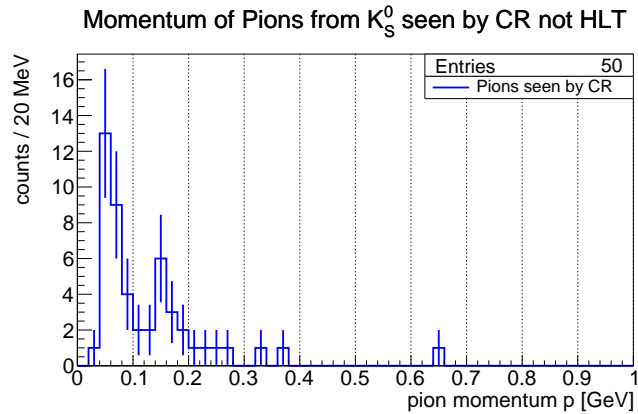
(a) Momentum distribution of pions from K_S^0 trackable with cluster rescue but not with HLT or DATCON.
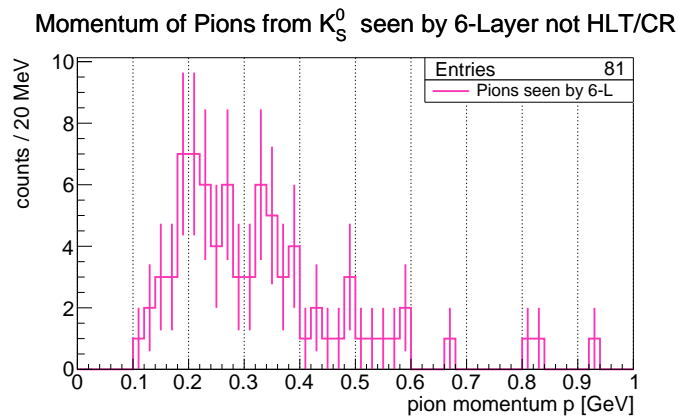
(b) Momentum distribution of pions from K_S^0 trackable with 6-layer tracking but not with HLT, DATCON or cluster rescue.

Figure 5.21.: Momentum distribution of pions from K_S^0 (cluster rescue and 6-layer tracking; all and HLT in figure 5.20).

5.5. $Z_c(3900)$ Decay Channel with Low Momentum Pions

To analyze the possibility of tracking and reconstruction including low momentum pions, a decay channel containing $Z_c(3900)^-$ was chosen (see figure 5.22) which is not observed yet and currently a subject of investigations. In this decay the π^- out of the D^{*-} gets only a small momentum out of the D^{*-} decay. The main part of its momentum will be from the decay of B^0 into $Z_c(3900)^-$ and K^+. The transversal momentum distribution of all simulated pions out of D^{*-} can be seen in figure 5.23 where the most pions have a momentum in the region of about $30 - 70\,\mathrm{MeV}/c$. In figure 5.24, we can see that this distribution is similar for all layers. We can see a small increment to the outer layer, but in general the difference is quite little. At the decay of K_S^0 its lifetime caused an observable secondary vertex. Here the short lifetime of the mother particles ($\tau_{B^0} = (1.519 \pm 0.007) \cdot 10^{-12}\,\mathrm{s}$) of $Z_c(3900)^-$ make it impossible to observe a secondary vertex.

$$
\begin{aligned}
\Upsilon(4S) &\longrightarrow B^0\ \overline{B}^0 \\
&\quad\ \hookrightarrow Z_c(3900)^-\ K^+ \\
&\qquad\qquad\ \hookrightarrow D^{*-}\ D^0 \\
&\qquad\qquad\qquad\qquad \hookrightarrow K^-\ \pi^+ \\
&\qquad\qquad\qquad \hookrightarrow \pi^-\ \overline{D}^0 \\
&\qquad\qquad\qquad\qquad\qquad\ \hookrightarrow K^+\ \pi^-
\end{aligned}
$$

Figure 5.22.: A decay channel of $\Upsilon(4S)$ via $Z_c(3900)^-$. In this chosen channel an D^{*-} decays in $\overline{D}^0$ and π^- (red ■) where the pion has a very low momentum.

Figure 5.23.: p_t distribution of charged pions from D^{*-} in the simulated decay. The plot describes the simulated data taken from the Monte Carlo data.

Figure 5.24.: p_t distribution of the hits caused by pions from D^{*-} on the VXD layers. The similar distribution for all layers indicates that tracks contain hits for all six layers.

5.5.1. Trackability of pions from D^{*-}

Like discussed before, the minimum condition for a successful helix reconstruction is that we have three hits. If we look at the hits per track in the SVD system in the bottom figure 5.25(a), we see a big amount of tracks with four hits, another big amount of tracks with no hits, and only a few in between. Those with four hits can be tracked by HLT or DATCON, while those without hits would be invisible for the SVD. They cannot be rescued with any PXD rescue system because even with two PXD hits a helix cannot be reconstructed. An interesting fact is, that almost all of these pions tracks in VXD are invisible for low momenta and they hit almost all layers for high momenta. The region where it changes is at about $30 - 40 \, \text{MeV}/c$. The reason for this is the detector geometry. If these pions have a low transversal momentum, they have a higher momentum in beam direction and therefore they are not in the acceptance of the detector. Because in these events we have almost no offset from interaction point, they just leave the acceptance and do not hit any sensor in the VXD.

This behavior we can see as well when we check the trackable pions by the different setups. In figure 5.26(a) we can see that there is a large amount of low p_t pions which are not covered by the HLT or DATCON tracking. Some of the low transversal momentum pions can be rescued by the cluster rescue or 6-layer tracking, but the very low momentum pions are not visible by any system. Because they are far below the minimum ionizing area, they would already cause a huge seed charge in the PXD, so the cluster rescue can cover them. The fact that they are invisible for everything shows us that they are out of the acceptance, mean they have high momentum in or against beam direction compared to the transversal component.
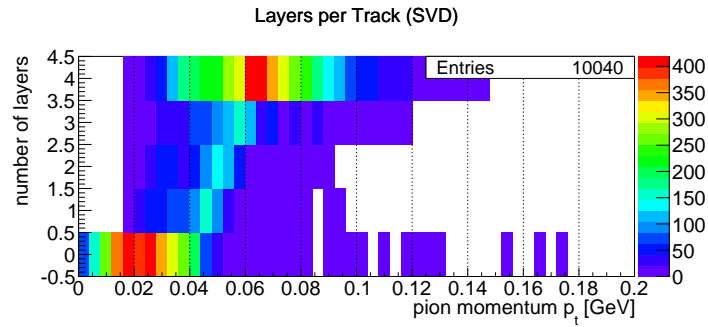
(a) Number of PXD and SVD layers with hits for a track for different p_t. One can see that there is a higher momentum region where the pions generate four hits and a lower momentum region with now hits. In between (at about $30 - 40\,\mathrm{MeV}/c$) is we can see the change which indicates the maximum radial distance a pion can reach.
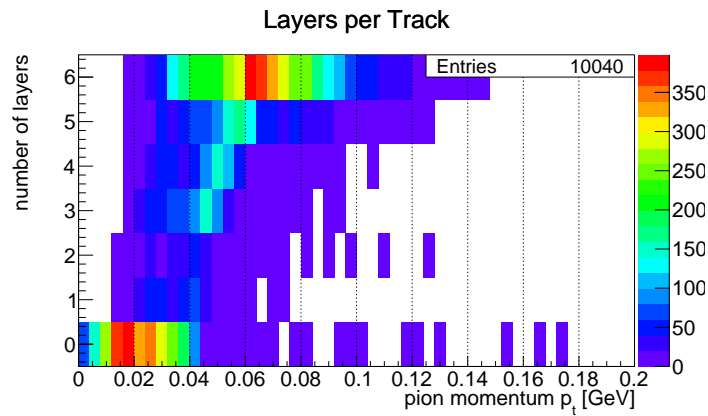
(b) Number of VXD layers (PXD+SVD) with hits for a track for different p_t. The observation is similar to figure (a). There is only a minimal difference. For a detailed discussion see the following chapters.

Figure 5.25.: Number of layer with hits by transversal momentum.
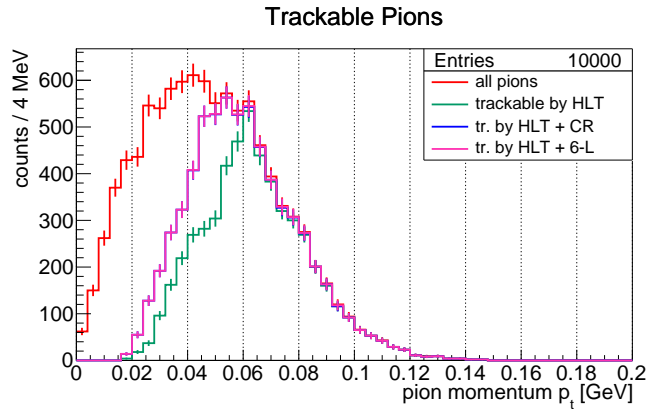
(a) Combined view of all pions (red ■) with the trackable pions from figure 5.26(b), 5.27(a) and 5.27(b). The blue ■ and purple ■ lines overlap. For details see figures 5.27(a) and 5.27(b).
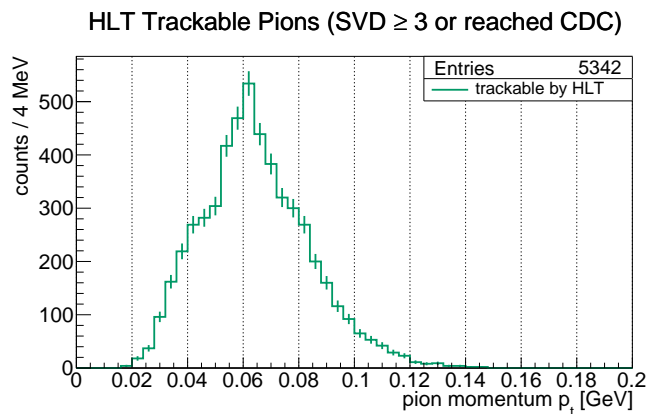
(b) Trackable pions with HLT or DATCON for different p_t. Requirement is at least three hits in SVD or any hits in CDC.

Figure 5.26.: Trackable pions for different p_t (combined and HLT; cluster rescue and 6-layer tracking in figure 5.27).
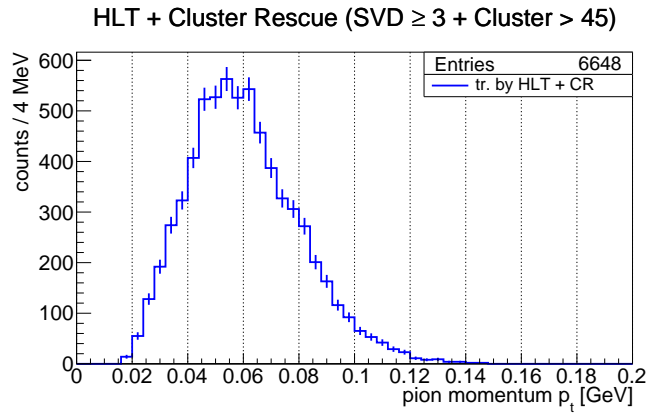
(a) Trackable pions with HLT, DATCON and additional the cluster rescue system for different p_t. Requirement is at least three hits in SVD together with reduced hits (seed charge > 1.8 of minimum ionizing which corresponds to an ADC value of > 45).
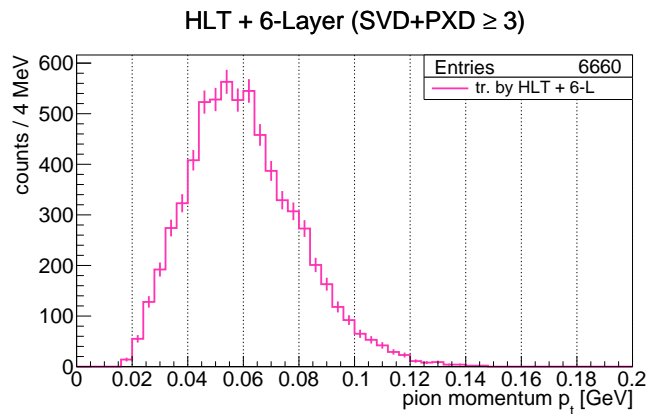
(b) Trackable pions with 6-layer tracking for different p_t. Requirement is at least three hits in SVD together with PXD.

Figure 5.27.: Trackable pions for different p_t (cluster rescue and 6-layer tracking; combined and HLT in figure 5.26).

5.5.2. Maximum Tracking Potential of Pions from D^{*-}

Because of the additional trackable pions with lower momenta the theoretical efficiency increases by using a cluster rescue or 6-layer tracking. In figure 5.28 is shown plots of the trackable pions normalized on the number of simulated pions from D^{*-}. In this case the increase in trackability for low momenta is much higher than it was for kaons (chapter 5.4). At momenta about $\approx 50\,\mathrm{MeV}$ the cluster rescue as well as a 6-layer tracking could increase the trackability by up to 40% (figure 5.28(b)). These pions are mainly pions with low momenta which do not reach the outer SVD layer. Because they are below the minimum ionizing region, they generate a seed charge which makes the cluster rescue highly efficient. For lower p_t they leave the acceptance, because their momentum points mostly in or against the beam direction. Because of the high efficiency of a cluster rescue at low momenta, the difference between cluster rescue and 6-layer tracking (figure 5.28(c)) is very small. Only at around $\approx 80\,\mathrm{MeV}$ a 6-layer tracking could get additional 1% which is almost nothing compared to the almost 100% trackability of the pions by the HLT or DATCON. Equivalent to the data for pions from kaons the detailed data for pions from Z_c(3900)$^-$ is shown in table 5.3.

Table 5.3.: Check of the tracking possibilities for the different systems. The percentage values are counted over all simulated pions from Z_c(3900)$^-$ in all momenta. Total number of simulated pions from Z_c(3900)$^-$ is 10000.

at least 3 hits in	HLT / DATCON only SVD or reach CDC	with cluster rescue SVD plus rescued cluster	with 6 layer tracking SVD with PXD
number of trackable pions	5342	6648	6660
ratio of trackable pions	53.42%	66.48%	66.60%
increment to HLT / DATCON cluster rescue		13.06%	13.18% 0.12%
max. incr. to HLT / DATCON **cluster rescue**		$\approx 40\%$ (at $p_t \approx 50\,\mathrm{MeV}$)	$\approx 40\%$ (at $p_t \approx 50\,\mathrm{MeV}$) $\approx 1\%$ (at $p_t \approx 80\,\mathrm{MeV}$)
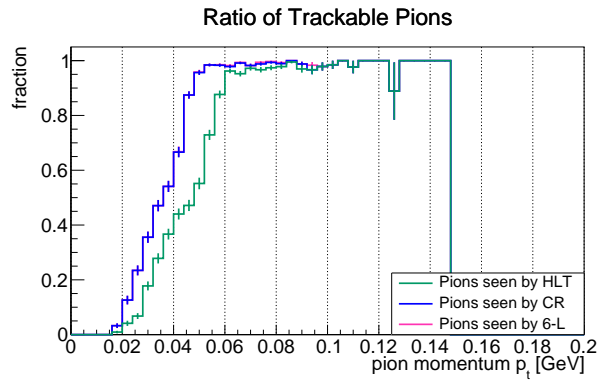
(a) Possible efficiency for a pion tracking with the three different setup options. The blue ■ and purple ■ lines overlap. In figures (b) and (c) is shown a differential plot between the shown ratios.
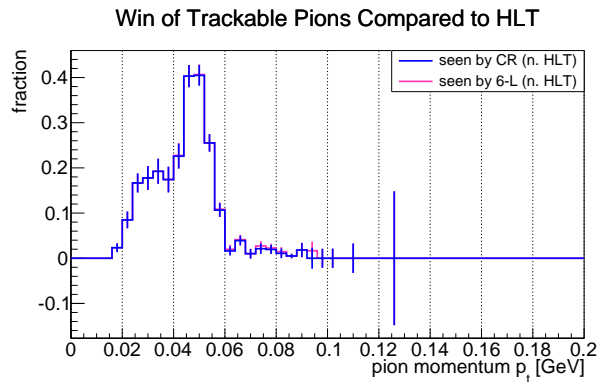
(b) Possible efficiency enhancement for a pion tracking with cluster rescue or 6-layer tracking compared to the HLT / DATCON only option. The two lines overlap. In figure (c) is shown a differential plot between the shown ratios.
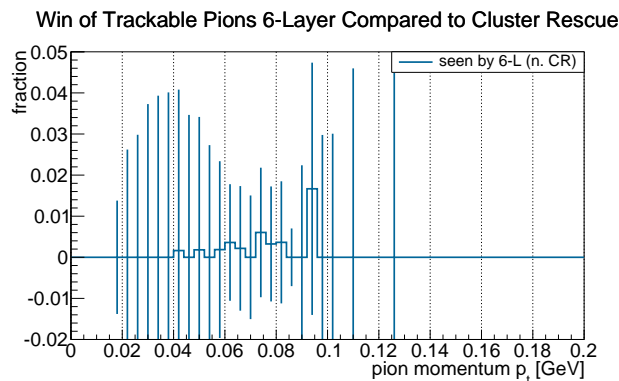
(c) Possible efficiency enhancement for a pion tracking with 6-layer tracking compared to cluster rescue. The error bar at 0.12 GeV is off scale.

Figure 5.28.: Possible efficiency for a pion tracking and the increasing of efficiency by adding cluster rescue and 6-layer tracking.

116

5.5.3. Momentum Distribution of Pions from D^{*-}

At the total momentum distribution of the pions from D^{*-} we can see that the overall distribution (figure 5.29(a)) is divided into three parts. Starting with high momenta, there are the pions which are trackable by the HLT or DATCON. Their momentum range ends at about $\approx 60\,\mathrm{MeV}$. Below this follows the range of pions down until $\approx 45\,\mathrm{MeV}$ which can be found by the cluster rescue or 6-layer tracking. The pions only seen by a 6-layer tracking are quite rare and do not describe a certain momentum range. The third big range at the total momentum distribution is below $\approx 45\,\mathrm{MeV}$. Here the pions do not hit any sensor because they are out of acceptance so the trackable pions are cut off at this point.
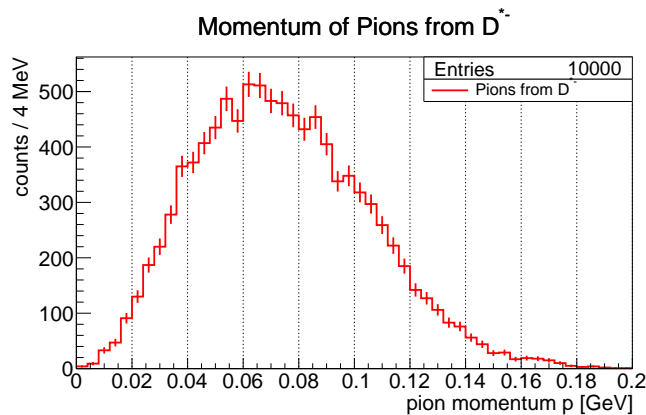
(a) Momentum distribution of all pions from D^{*-}.
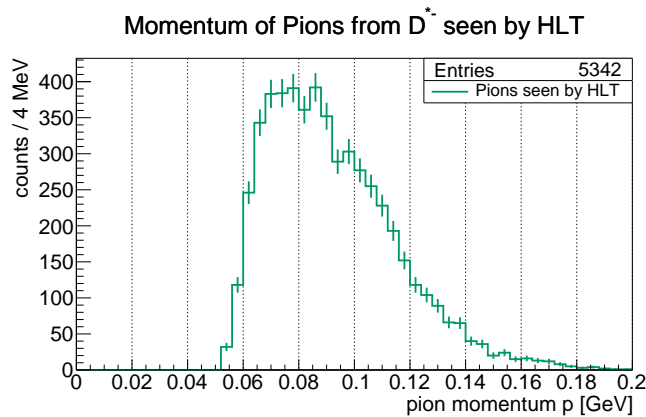
(b) Momentum distribution of HLT or DATCON trackable pions from D^{*-}.

Figure 5.29.: Momentum distribution of pions from D^{*-} (all and HLT; cluster rescue and 6-layer tracking in figure 5.30).
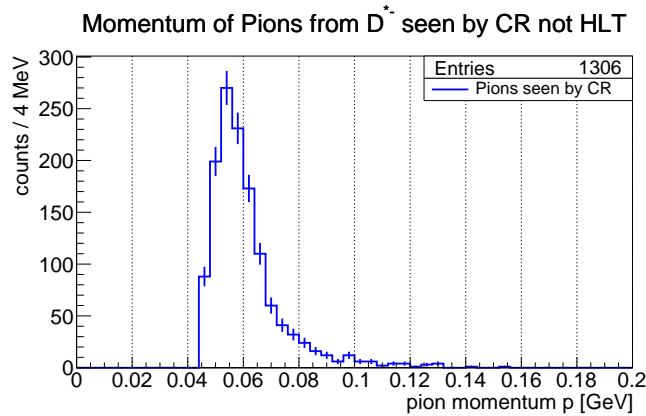
(a) Momentum distribution of pions from D^{*-} trackable with cluster rescue.
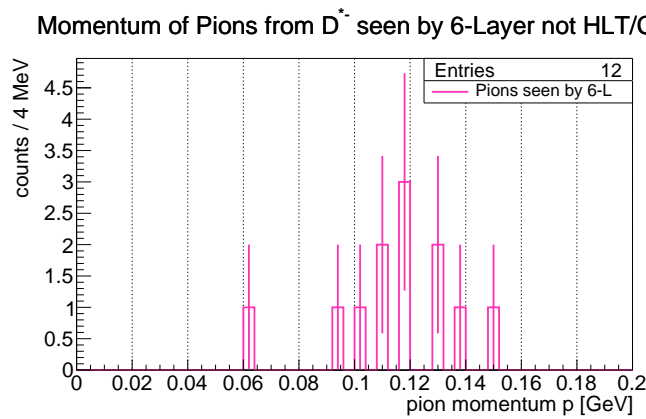
(b) Momentum distribution of pions from D^{*-} trackable with 6-layer tracking.

Figure 5.30.: Momentum distribution of pions from D^{*-} (cluster rescue and 6-layer tracking; all and HLT in figure 5.29).

5.6. Conclusion for Feasibility of 6-Layer Tracking

In my feasibility study for 6-layer tracking I found out, that for pions from secondary vertices like at K_S^0 events, the tracking algorithms of HLT and DATCON cover 90.48% of the pions. The cluster rescue algorithm covers all hits with a seed charge of at least 1.8 times the charge of a minimum ionizing particle. This rescues additional 0.46%. A 6-layer tracking could get 1.23% on top of the existing tracking algorithms, which is a gain of 0.75% to the cluster rescue and for pions with momenta of $p_t \approx 200\,\mathrm{MeV}$ this can reach $\approx 2\%$.

At the analyze of pions with small momenta in the case of a yet undiscovered decay of $Z_c(3900)^-$ the tracking algorithms cover 53.42% and the cluster rescue additional

13.06%. Because the particles are below the minimum ionizing region, the cluster rescue covers almost all hits to be rescued. A 6-layer tracking can increase this only by 0.12%.

All together the investigation shows that a future 6-layer tracking will have a potential to rescue additional hits of particles in the minimum ionizing region. Especially it will cover cases of particles from secondary vertices. Those tracks are not covered by the recent algorithms and may leave the angular acceptance of the detector before generating enough hits for a successful SVD based tracking.

CHAPTER 6

CONCLUSION AND OUTLOOK

The PXD at the Belle II experiment with an inner radius of only 14 mm will be placed in short distance around the beam pipe which has an outer radius of 12.5 mm. With this placement close to the beam the vertex resolution will be increased and therefore it will be possible to improve the reconstruction efficiency and accuracy of secondary vertices caused by short-lived particles.

Because of the short distance to the interaction point, we expect to have a very high background induced occupancy of up to 3% on the pixel detector. With this high occupancy we expect a data rate of about 20 GB/s which exceeds the bandwidth limitations of the data storage. To reduce this data rate we chose a concept of Region of Interests (ROI). Based on hits in the outer detectors, back projections of tracks are performed. With those tracks, ROIs in the PXD planes are calculated and used for data reduction. This reduction works in the way, that the pixel in the incoming data are checked if they are inside a ROI. In this case they are sent out, otherwise they are removed from the data stream.

As hardware platform we use a Compute Node (CN) developed in close cooperation of Institute of High Energy Physics (IHEP) in Beijing together with Justus-Liebig-Universität Gießen (JLU), Germany. In the newest revision it is based on a Xilinx Virtex5 fx70T FPGA and four SFP cages for e.g. optical links with up to 6.25 Gbit/s and supports a high rate of parallelization.

This thesis consists of two independent parts. In the first part of this thesis I focused on my development of the online data reduction algorithm which will be integrated in the DAQ of the Belle II experiment while in the second part I investigated the potential of a so called 6-layer tracking in the VXD system. Because of the highly different type of the parts, I give two separate conclusions.

Online Data Reduction for Belle II

At a test setup with electron beam at DESY a first test had been performed with the whole DAQ integration including PXD and SVD sensors. In this test the used prototype PXD had a smaller size (128×480 pixel) than the one which will be used in the final experiment (250×768 pixel). For the verification of the ROI selection logic a full recording of in- and output data was included. With this setup I recorded $1.2 \cdot 10^6$ events containing in total $4.8 \cdot 10^8$ hits. The final run with this setup had 186 000 events with an average occupancy before reduction of $\approx 0.80\%$. Based on the ROI sent by the two systems called HLT (High Level Trigger) and DATCON (Data Acquisition Tracking Concentrator Online Node) the data are reduced to an average occupancy after reduction of $\approx 0.12\%$ which gives a data reduction factor of 6.9. I checked for selection errors and got the result, that all received pixel were correctly selected or rejected. I could not observe any selection errors within this test.

At an investigation of the incoming ROIs I observed a peak for a distance between ROI center and hit of 17.624 ± 0.029 and a main offset direction of $\frac{\pi}{2}$ and $\frac{3\pi}{2}$. With a more accurate position of the ROIs their size could be reduced. The reduction factor of 6.9 is strongly dependent on the size of the received ROIs from the two tracking systems. For a higher reduction factor, which is favored for the final setup at Belle II, smaller and more accurate ROIs are needed.

As a future outlook of this project, the data will arrive in a cluster based format which will be defined in the future. The decoding and the re-encoding of the data have to be adapted to this format for a cluster based data reduction.

Feasibility Studies of 6-Layer Tracking at Belle II

The data reduction based on ROIs is strongly dependent on the tracking systems which deliver the ROIs. They use as base for their tracking the data of SVD and the outer detectors. Because of mathematical reasons at least three hits are needed to reconstruct a helix shaped track which is used to calculate the ROIs on the PXD. Additional will be used a so-called cluster rescue system to recover hits in the PXD which will be discarded otherwise.

In this part I investigated the limitations of the currently planned system with ROI selection and cluster rescue. Furthermore I investigated if it would be possible to increase the quality of data selection by adding a 6-layer tracking, a concept which would use all data from PXD and SVD before reduction to perform a tracking. With this system, additional data can be marked to be excluded from the data reduction. For this I focused on two cases which could cause problems at the reconstruction of events: secondary vertices and low momentum charged particles.

As an example for secondary vertex events I chose events including a K_S^0. These kaons have a lifetime long enough to leave the interaction point, but still mostly decay inside the PXD region. For all pions from K_S^0, the tracking systems can cover 90.48%. The cluster rescue can get additional 0.46%, while a 6-layer tracking could cover 1.23% which is 0.75% more than the cluster rescue. At transversal momenta of

about $p_t \approx 200\,\mathrm{MeV}$ this win by adding a 6-layer tracking can increase up to $\approx 2\%$.

For an example of low momentum particles I chose a decay channel of $Z_c(3900)^-$ via D^{*-} which decays in $\overline{D}^0$ and π^-. This pion has a very small momentum. Here my result was, that the pions which have a such low transversal momentum that they do not reach enough SVD layers to perform tracking will be below the minimum ionizing momentum region. Therefore the cluster rescue covers those pions. In total the tracking systems cover in this case 53.42%. The cluster rescue can cover additional 13.06% while a 6-layer tracking can cover 13.18%, which is an increase of only 0.12%.

As a result of this investigation, the cluster rescue will work well for the low momentum particles from interaction point. For secondary vertex events with higher momentum the cluster rescue cannot register those hits but a 6-layer tracking would be able to perform a tracking on these hits. All this data are calculated on theoretical perfect basis. The reason for this is, that the 6-layer tracking is only a concept and a real algorithm does not exist yet. A future project is needed to construct such an algorithm and calculate efficiencies for the realized algorithms to compare all three systems.

APPENDIX

SELECTED DECAY IN BASF2 FRAMEWORK

A.1. K_S^0 Decay Modes

Table A.1.: K_S^0 decay modes in basf2. 99.7% decay in two pions where only the 69.1% charged pions are visible in the vertex detectors. cf. [2]

ratio	particles
0.691 321 852	$\pi^+ \ \pi^-$
0.306 221 852	$\pi^0 \ \pi^0$
$2.01 \cdot 10^{-7}$	$\pi^+ \ \pi^- \ \pi^0$
$1.722\,185 \cdot 10^{-3}$	$\pi^+ \ \pi^- \ \gamma$
$4.2831 \cdot 10^{-5}$	$\pi^+ \ \pi^- \ e^+ \ e^-$
$2.5 \cdot 10^{-8}$	$\pi^0 \ \gamma \ \gamma$
$2.399 \cdot 10^{-6}$	$\gamma \ \gamma$
$3.443\,28 \cdot 10^{-4}$	$\pi^+ \ e^- \ \nu_e$
$3.443\,28 \cdot 10^{-4}$	$\pi^- \ e^+ \ \nu_e$

APPENDIX B

DOCUMENTATION OF ROI SELECTION CORE V1.16

Here is documented the different components of the ROI Selection Core v1.16 written in VHDL (VHSIC Hardware Description Language). The source code of this core as well as the previous versions you can find on:

`fb07-nucular.physik.uni-giessen.de`

in the repository:

`/home/dmuenchow/repository_roi.git`

The content of this repository is attached to this thesis as a CD.

As a remark to this chapter and to the code of the ROI selection core, here the acronyms DHH and DHHC are used in their old meaning. The renaming of those systems to DHE and DHC happened after the development of the selection core.

The core has two LocalLink inputs and one output as well as some control flags. Data frames from PXD have to be delivered at the input port `LL_IN_DHH` and the corresponding ROIs to the input `LL_IN_ROI`. The reduced output data is then sent out on `LL_OUT`. For a detailed description of the data handling and selection process see chapter 3.5.

ROIs have to be always delivered together with corresponding data from DHC. The ROIs have to be delivered in the recent ROI data format (see figure 3.11). The corresponding DHC data are expected to have start with a frame marked as DHC start frame and end with a DHC end frame. At the output is added a new frame with the first five header words of the ROI frame as a new ONSEN trigger frame and if wanted as second last frame an ONSEN ROI frame (see figure 3.10).

From the DHC data input, all frames except the DHP zero-suppressed data are forwarded to the output as they are. The DHP zero-suppressed are processed in the ROI section logic and only pixel inside at least one ROI are sent out. The CRC checksum is calculated new in this case.

Figure B.1.: Detailed schematics of the ROI selection logic. The functionalities of the inner components are described in the following chapters.
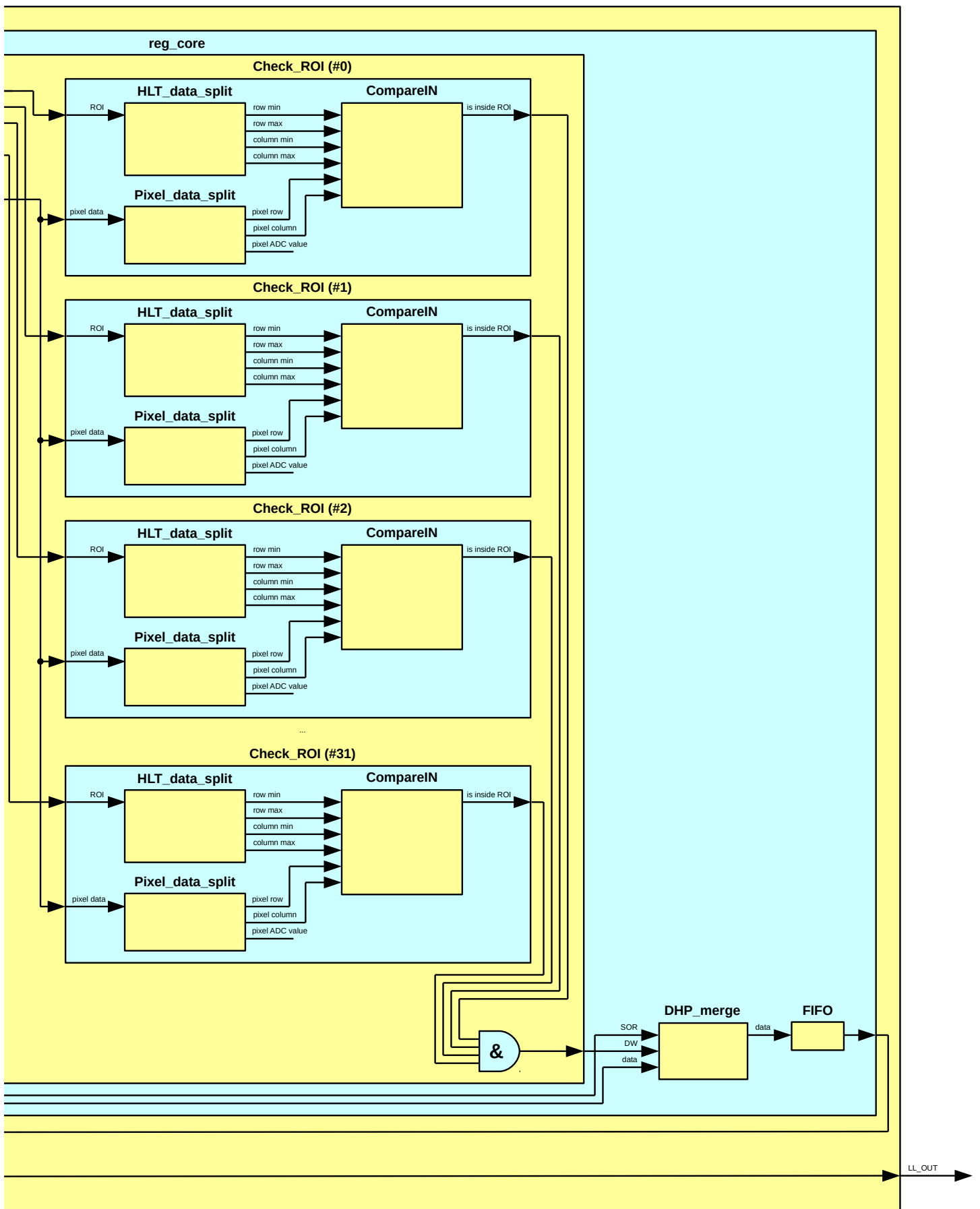
Beside the usage for the selection process, the ROI data input is forwarded to the output as ONSEN trigger frame and as ONSEN ROI frame. The second one is only sent out if this is activated. This activation can be set by the ROI data by setting the flag in the header or by setting the input `ROI_OUT` of the core to high.

The incoming data can contain up to two pixel in one data word. Because they have to be processed serial for decoding and data reduction, the inner part of the selection logic has to run in double speed compared to the incoming data. To support this, the core has an additional `Core_CLK` which needs to be at least the double of the LocalLink clock signals.

With the `Core_RST` input all FIFO are reseted and the core starts by waiting for new ROIs and DHC data. For monitoring issues a 32 bit slave register is used.

Table B.1.: Content of the 32 bit slave register of the ROI selection core.

Bits	Data Content
`[31:24]`	Data word counter of LocalLink `LL_IN_ROI` (8 bit wide).
`[23:16]`	Data word counter of LocalLink `LL_IN_DHH` (8 bit wide).
`[15: 8]`	Data word counter of LocalLink `LL_OUT` (8 bit wide).
`[ 7: 4]`	not used (always `0000`).
`[ 3]`	Signal `Trigger_Error` from selection logic. Is high if trigger numbers of ROI and DHC data do not match. If the both trigger numbers are equal, this flag is low.
`[ 2]`	Destination ready signal of `LL_IN_ROI`. Low if destination ready.
`[ 1]`	Destination ready signal of `LL_IN_DHH`. Low if destination ready.
`[ 0]`	Source ready signal of `LL_OUT`. Low if source ready.

B.1. `roi_frame_handler_ll.vhd` **and** `user_logic.vhd`

The vhdl files `roi_frame_handler_ll.vhd` and `user_logic.vhd` are generated by the Xilinx tools during the user core generation. Only some parts were added to include the ROI selection logic and its needed ports and signals and clocks. Also the slave register are set in those parts and allow some monitoring of the core.

B.2. `frame_handler.vhd`

This is the main component to handle the incoming frames whether they shall be processed (pixel data with corresponding ROIs), whole frame content discarded (pixel data without corresponding ROIs) or just forwarded without processing (non-data frames). It also includes an additional frame with the header information of the ROI input frame and a ROI output frame to store the ROIs used for selection. Therefore
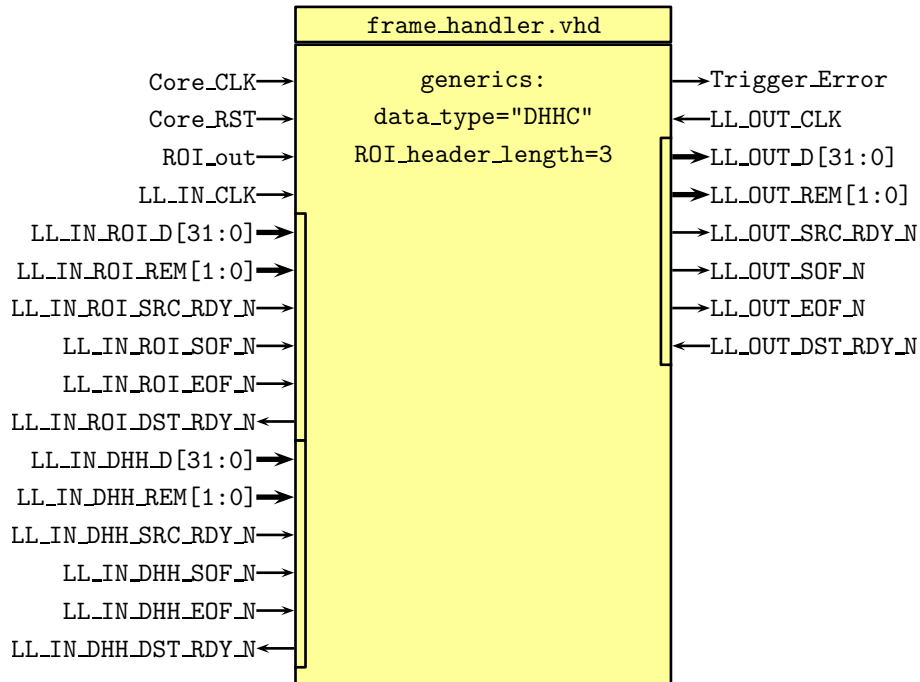
Figure B.2.: Diagram of the `frame_handler.vhd` ports.
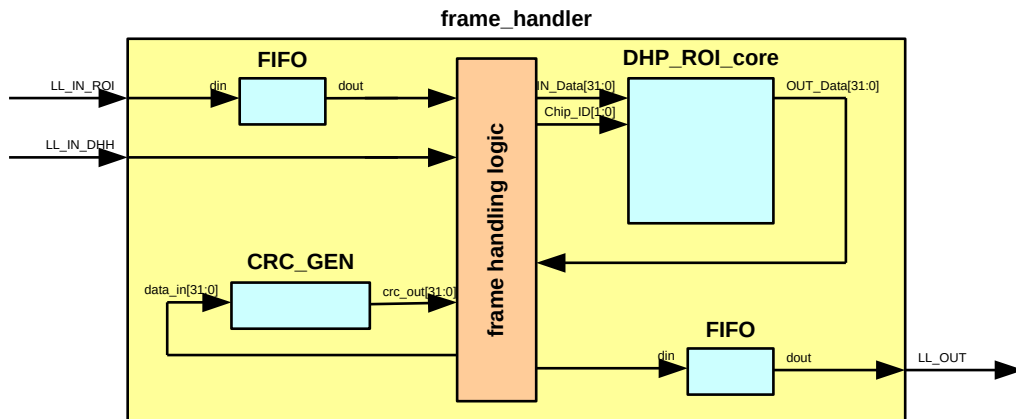
Figure B.3.: Simplified schematics of `frame_handler` component. It is reduced to the most important data signals. The frame handling logic controls the data routing. To process the data, generate new frames (trigger frame or ROI output frame) or forward them directly to the output FIFO. If needed, a CRC recalculation is processed.
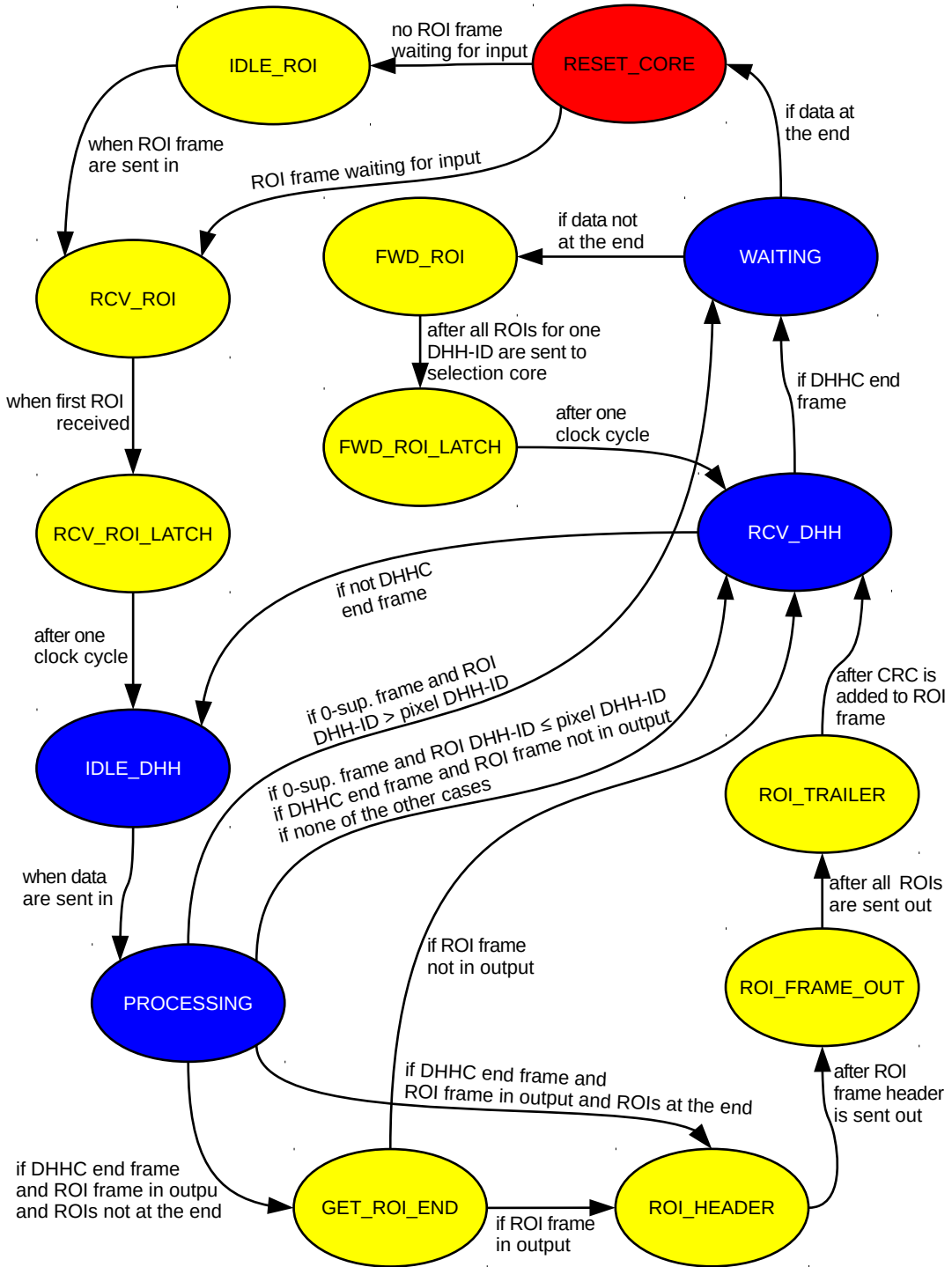
Figure B.4.: Schematics of the state machine in the frame handler. At start up the initial state is RESET_CORE (red ■).

Table B.2.: Description of the states of the state machine in `frame_handler.vhd`.

State	Description
RESET_CORE	Reset state to reset all signals. If ROI data already waiting for input next state will be **RCV_ROI** otherwise **IDLE_ROI**.
IDLE_ROI	Waiting for ROI data to start. As soon as ROI data are send in go to **RCV_ROI**.
RCV_ROI	Receive frame header of ROIs. As soon as first ROI received, stop ROI receiving and go to **RCV_ROI_LATCH** state.
IDLE_DHH	Waiting for DHC data input. As soon as DHC arrive then: **Zero-suppressed data and DHE-ID of ROI < pixel:** Pixel data for a higher DHH-ID than the ROIs. Other ROIs needed. Next state **PROCESSING**; afterwards **RCV_DHH**. **Zero-suppressed data and DHE-ID of ROI > pixel:** Pixel data for a lower DHH-ID than the ROIs. Pixel will be discarded because of no ROI. Next state **PROCESSING**; afterwards **WAITING**. **Zero-suppressed data and DHE-ID of ROI = pixel:** Pixel data for the same DHH-ID than the ROIs. Pixel will be reduced. Next state **PROCESSING**; afterwards **RCV_DHH**. **DHHC end frame:** Next state **PROCESSING**; afterwards if ROI output frame shall be send and ROIs not at the end go to **GET_ROI_END**, if ROI output frame shall be send and ROIs at the end go to **ROI_HEADER** otherwise go to **RCV_DHH**. **other cases:** Next state **PROCESSING** and afterwards go to **RCV_DHH**.
RCV_DHH	Receive DHE data until end of frame. Then for DHC end frame go to **WAITING** otherwise go to **IDLE_DHH**.
FWD_ROI	Forwards all ROIs on one DHH-ID to the selection component. Afterward go to **FWD_ROI_LATCH**.

State	Description
RCV_ROI_LATCH	Waiting state to for signal synchronization. After one clock cycle got to **IDLE_DHH** state.
FWD_ROI_LATCH	Waiting state to for signal synchronization. After one clock cycle got to **RCV_DHH** state.
ROI_HEADER	Generate ROI frame header and go to **ROI_FRAME_OUT**.
ROI_FRAME_OUT	Read out ROI input frame buffer to send the content as ROI output frame. When the buffer is empty go to **ROI_TRAILER**.
ROI_TRAILER	Add the CRC to the ROI output frame and then go to **RCV_DHH**.
GET_ROI_END	Read in ROIs until frame ends. Afterwards if ROI output frame shall be send go to **ROI_HEADER** otherwise go to **RCV_DHH**.
PROCESSING	Processing state at the end of data reduction. Provides a delay for 18 clock cycles until all processed data are send out of the reduction pipeline. Afterwards go to the previous chosen state.
WAITING	Reset ROI core after processing all pixel of one sensor. Includes an rely because of delay in FIFO resets. If DHE data are at the end of event, go to **RESET_CORE** otherwise to **FWD_ROI**

the ROI input data are buffered in a FIFO. The output of this component has a FIFO with programmable threshold. It is needed to be sure that after reaching this threshold and sending a destination-not-ready to the input link, still all data in pipeline fit in this FIFO.

With the generic `C_DATA_TYPE` it is possible to switch the data format whether it is from DHE or from DHC and with `C_ROI_header_length` the number of header words of the ROI input data can be adjusted. This process is realized with a state machine (overview of the state machine in figure B.4).

Table B.3.: The input and output ports of `frame_handler.vhd`.

Port		Description
`Core_CLK`	in	Clock input. Has to be at least double of `LL_IN_CLK`.
`Core_RST`	in	Reset signal.
`ROI_out`	in	Flag to always include ROIs to output data.
`Trigger_Error`	out	Output signal is '1' if trigger number in ROIs do not match the trigger number in pixel frames.
`LL_IN_CLK`	in	Clock input for `LL_IN_ROI` and `LL_IN_DHH`.
`LL_IN_ROI[31:0]`	in	32 bit wide LocalLink input for ROI data.
`LL_IN_DHH[31:0]`	in	32 bit wide LocalLink input for pixel data.
`LL_OUT_CLK`	in	Clock input for `LL_OUT`.
`LL_OUT[31:0]`	out	32 bit wide LocalLink output for reduced data.

B.3. `DHP_ROI_core.vhd`
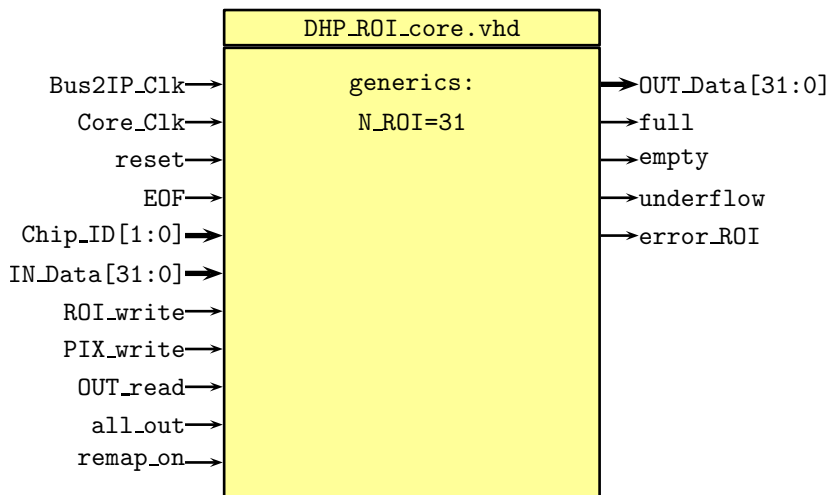
Figure B.5.: Diagram of the `DHP_ROI_core.vhd` ports.

This component handles encoded data streams as they are sent by HLT and DHHC. Pixel and ROIs are sent over the same input, while ROIs have to be sent first.

After the input data have passed through an input FIFO, ROIs are directly sent to `reg_core`. Pixel first will be decoded by `DHP_decode` and the decoded data are then send to `reg_core` for the ROI check while the encoded 16 bit aligned data from `split_out` are delivered to `DHP_merge`. The check result from `reg_core` is then the control signal for the `DHP_merge` to rearrange the zero-suppressed data.
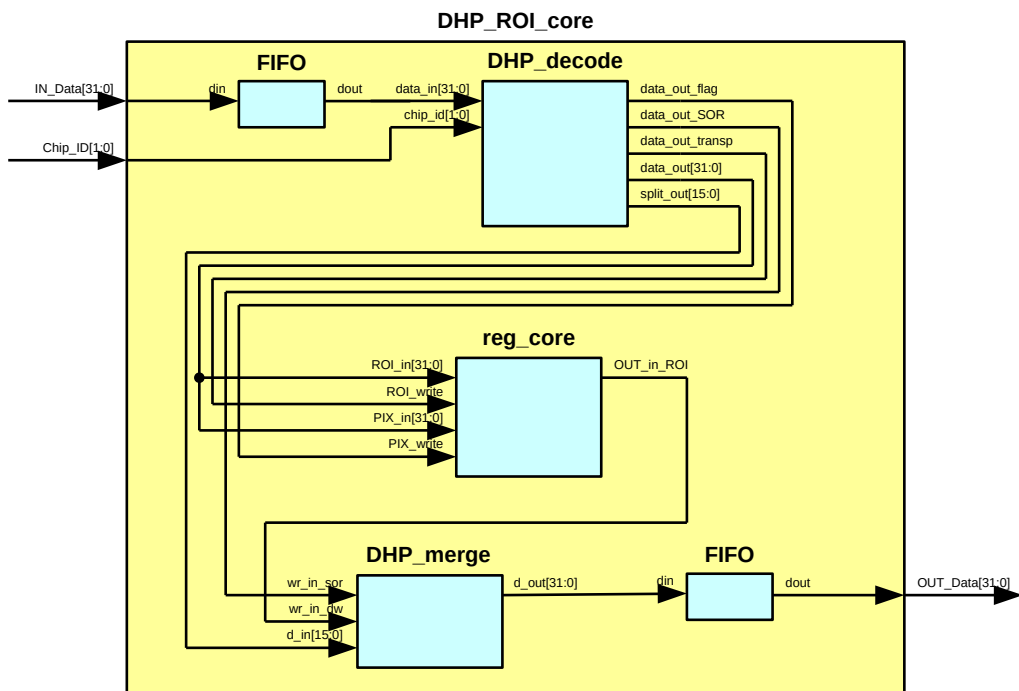
Figure B.6.: Simplified schematics of `DHP_ROI_core` component. It is reduced to the most important data signals for better clarity.

At the output the data have passed through an FIFO again.

Table B.4.: The input and output ports of `DHP_ROI_core.vhd`.

Port		Description
`Bus2IP_Clk`	in	Clock input.
`Core_Clk`	in	Clock input. Has to be at least double of `Bus2IP_Clk`.
`reset`	in	Reset signal.
`EOF`	in	Signal to mark end of frame words.
`Chip_ID[1:0]`	in	2 bit input for chip ID from frame header.
`IN_Data[31:0]`	in	32 bit input for ROI and zero-suppressed encoded pixel data as they are sent from HLT and DHHC.
`ROI_write`	in	Input signal is '1' for ROI input.
`PIX_write`	in	Input signal is '1' for pixel input.
`OUT_Data[31:0]`	out	32 bit output for zero-suppressed encoded pixel data of pixel which are inside at least one ROI.
`OUT_read`	in	Input signal is '1' to read out selected pixel.
`all_out`	in	Input signal to activate unreduced output of all pixel.
`full`	out	Signal full of output FIFO.
`empty`	out	Signal empty of output FIFO.
`underflow`	out	Signal underflow of output FIFO.
`error_ROI`	out	Output signal is '1' if number of intend ROIs is bigger than `N_ROI`. In this case all pixel will be sent out.

B.4. CRC_GEN.vhd
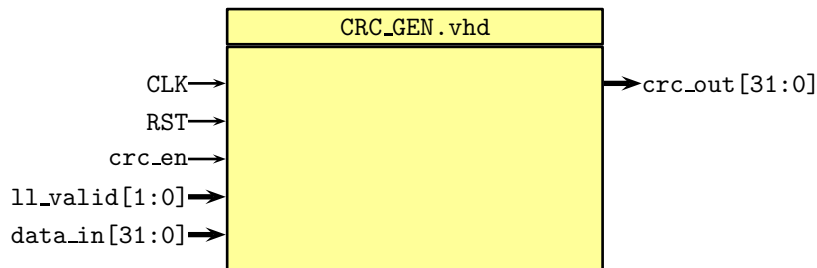
Figure B.7.: Diagram of the `CRC_GEN.vhd` ports.

This component is responsible to connect the hardware CRC component in the FPGA and use it with the chosen settings for CRC calculation in DHC data. As polynom is used the standard polynom which is also used e.g. for ethernet CRC. In contrast to ethernet, here the start value is `"00000000"`. Additional the bits of each byte in the input data had to be reflected. Therefore the function `reflect_bytes`

is added.

Table B.5.: The input and output ports of `CRC_GEN.vhd`.

Port		Description
`CLK`	in	Clock input.
`RST`	in	Reset signal.
`crc_en`	in	Enable signal. If high, CRC calculation is activated.
`ll_valid[1:0]`	in	Value to describe how many bytes of the `data_in` word contain data.
`data_in[31:0]`	in	Input data word.
`crc_out[31:0]`	out	Checksum output.

B.5. `reg_core.vhd`
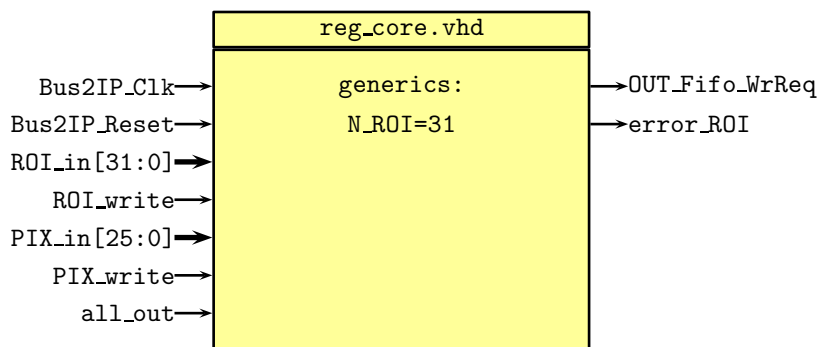
Figure B.8.: Diagram of the `reg_core.vhd` ports.

This is the head component for the ROI check. It receives first all ROIs in the format like it is provided by the input data from HLT. Afterwards it receives the already decoded pixel data. As output there is a logic signal if the pixel is inside at least one ROI.

The generic `N_ROI` is the value to define the maximum number of ROIs. if it shall be more than 31 the corresponding value in `roi_types` has to be adjusted as well.

This component handles the input data to be sent to the `roi_latch` buffer with parallel outputs. Each of these parallel outputs is connected to one `Check_ROI`. All this checking components receive the input pixel and if at least one of these checks return '1' the output `OUT_in_ROI` returns '1' as well.
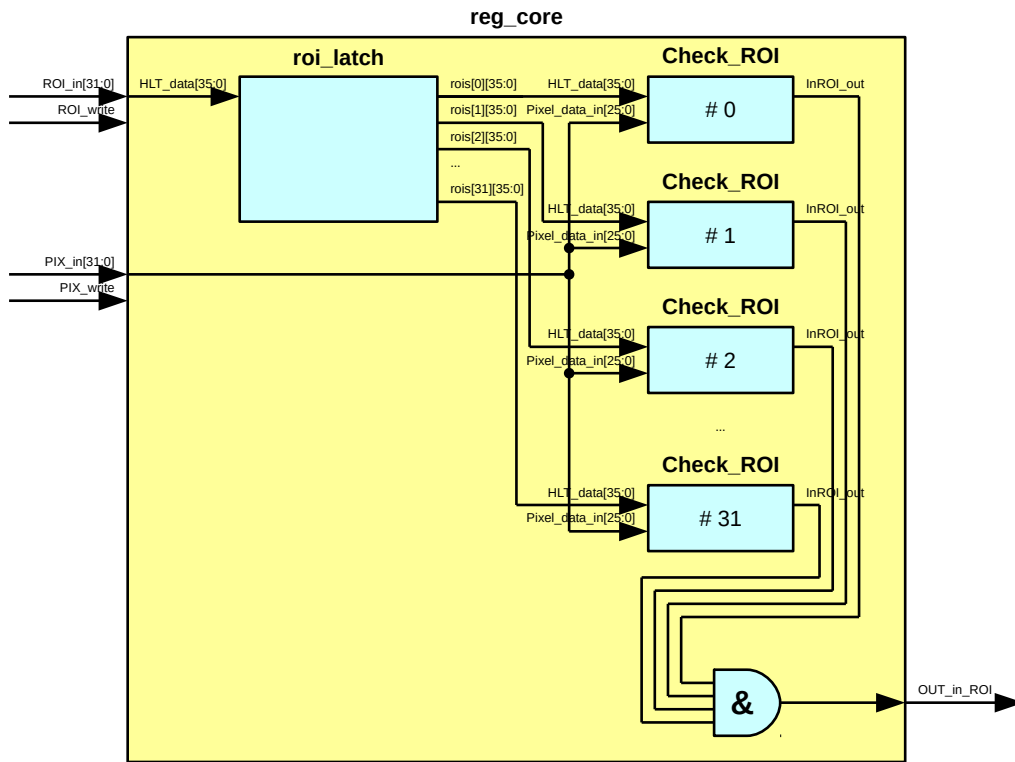
Figure B.9.: Simplified schematics of `reg_core` component. It is reduced to the most important data signals. The input signals `ROI_write` and `PIX_write` are used inside the component but their distribution is not shown in this diagram. The number of ROIs to be checked in parallel in this diagram is 32. Only 4 of the 32 `Check_ROI` are shown for more clear arrangement.

Table B.6.: The input and output ports of `reg_core.vhd`.

Port		Description
`Bus2IP_Clk`	in	Clock input.
`Bus2IP_Reset`	in	Reset signal.
`ROI_in[31:0]`	in	32 bit input for ROI data.
`ROI_write`	in	Input signal is '1' for ROI input.
`PIX_in[26:0]`	in	26 bit input for decoded pixel data.
`PIX_write`	in	Input signal is '1' for pixel input.
`all_out`	in	Input signal to activate unreduced output of all pixel.
`OUT_in_ROI`	out	Output signal is '1' if the pixel is inside at least one ROI.
`error_ROI`	out	Output signal is '1' if number of intend ROIs is bigger than `N_ROI`. In this case all pixel will be send out.

B.6. `DHP_decode.vhd`
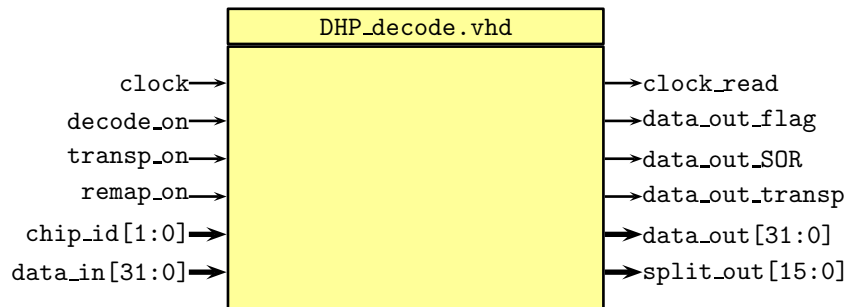
Figure B.10.: Diagram of the `DHP_decode.vhd` ports.

This component is used to decode zero-suppressed data from DHP. A remapping of the column numbers will be done on DHE but it is supported by this component as well. It has different modi:

Transparent: If it is set to transparent, the input data are forwarded unchanged to `data_out` and no data are sent out at `split_out`. Additional the `data_out_transp` is set to '1'.

Decode without remap: If it is set to decode, the input data will be decoded. For this the 32 bit input data are split into two words of 16 bit which are processed separately.

For a SOR the 16 bit zero-suppressed data are sent out at `split_out` and `data_out_SOR` is set to '1'.

For a DW the 16 bit zero-suppressed data are sent out at `split_out` and `data_out_flag` is set to '1'. On `data_out` the decoded data are sent.

Decode with remap: This mode works similar to the mode without remap. The only difference is that the column numbers are remapped, because the original numbers are not in ascending order. This is corrected on the DHH. If this was not done, the decoder can process the remapping as well.

Table B.7.: The input and output ports of `DHP_decode.vhd`.

Port		Description
`clock`	in	Clock input.
`decode_on`	in	Input signal to activate decoding.
`transp_on`	in	Input signal to activate unchanged forwarding from data input to data output.
`remap_on`	in	Input signal to activate remapping of column numbers.
`chip_id[1:0]`	in	Chip ID from header word. Represents the upper two bits of column number.
`data_in[31:0]`	in	32 bit wide data input. Contains two times 16 bit words in zero-suppressed format.
`clock_read`	out	Output clock for read out input FIFO. Clock is a divided by to from input clock.
`data_out_flag`	out	Output signal is '1' if decoded pixel on `data_out` and original coded data are sent on `split_out`.
`data_out_SOR`	out	Output signal is '1' if original coded start of row is sent on `split_out`.
`data_out_transp`	out	Output signal is '1' if original unchanged data are sent on on `data_out`.
`data_out[31:0]`	out	32 bit data output for forwarded unchanged data or decoded pixel.
`split_out[15:0]`	out	16 bit data output for split zero-suppressed data.

B.7. `DHP_merge.vhd`
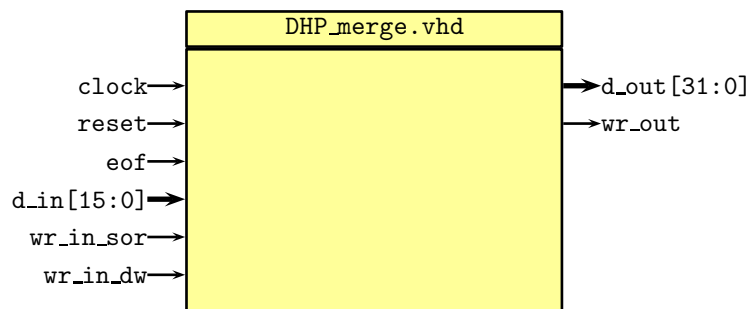
Figure B.11.: Diagram of the `DHP_merge.vhd` ports.

This component receives zero-suppressed data in 16 bit words over `d_in` together with a signal whether it is a start of row (SOR) (`wr_in_sor`='1') or a data word

(DW) (`wr_in_dw='1'`). This component reorganizes the data stream. In case there is a SOR without DW, it is not needed in the stream and will be removed. This function is used to remove unneeded SOR words from the data after the ROI selection is done. The output is 32 bit wide so always two DW are combined and the last word is filled up to provide a 32 bit alignment. As fill word is used the last SOR.

Table B.8.: The input and output ports of `DHP_merge.vhd`.

Port		Description
`clock`	in	Clock input.
`reset`	in	Reset signal.
`elf`	in	End-of-frame input; important to know when data stream ends and output possibly has to be filled up.
`d_in[15:0]`	in	Data input.
`wr_in_sor`	in	Input signal has to be '1' if input data is SOR.
`wr_in_dw`	in	Input signal has to be '1' if input data is DW and shall be kept.
`d_out[31:0]`	out	Data output.
`wr_out`	out	Output signal is '1' if data are sent out.

B.8. `Latch_bit.vhd`
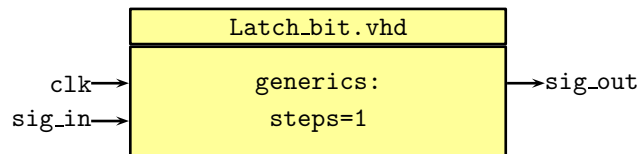
Figure B.12.: Diagram of the `Latch_bit.vhd` ports.

Delays the input signal `sig_in` for number of clock cycles set by `steps` before sending out at `sig_out`.

B.9. `Check_ROI.vhd`

Main component to check one pixel if it is in one certain ROI. This component is used in parallel to check one pixel for all ROIs at the same time. The check is done unclocked and the component uses further components to extract the coordinates from the pixel and ROI data words and to perform the check.
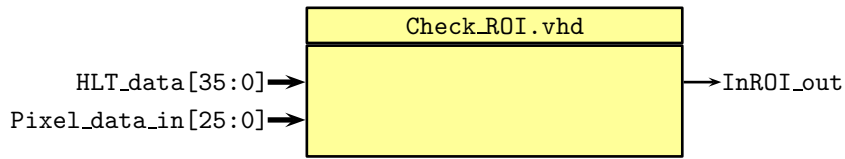
Figure B.13.: Diagram of the `Check_ROI.vhd` ports.
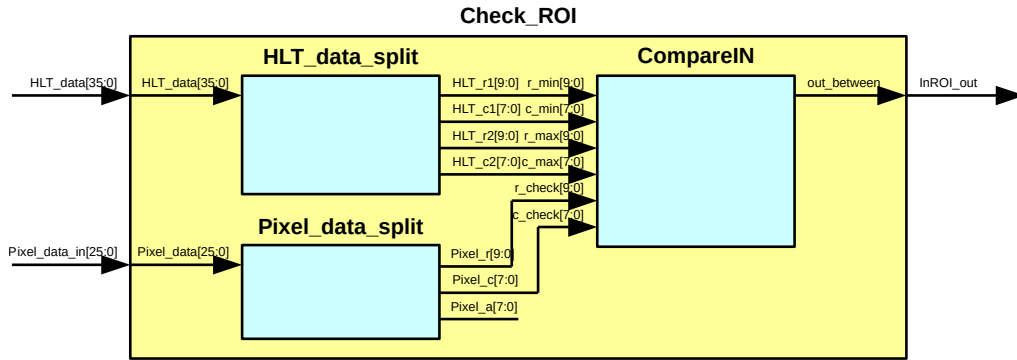
Figure B.14.: Simplified schematics of `Check_ROI` component.

B.10. `latch_pix.vhd`
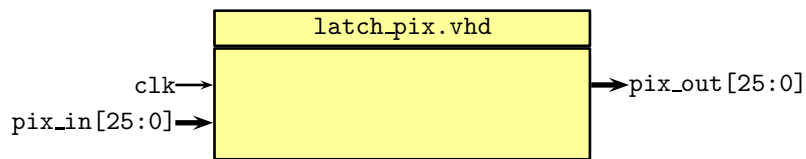
Figure B.15.: Diagram of the `latch_pix.vhd` ports.

Delays the 26 bit input signal `pix_in` for one clock cycle before sending out at `pix_out`.

B.11. `latch_roi_out.vhd`

Delays the input signal `roi_chk_in` for one clock cycle before sending out at `roi_chk_out`.

145

Table B.9.: The input and output ports of `Check_ROI.vhd`.

Port		Description
`HLT_data[35:0]`	in	ROI data input.
`Pixel_data_in[25:0]`	in	Pixel data input.
`InROI_out`	out	Output signal is '1' if the pixel is inside the ROI.
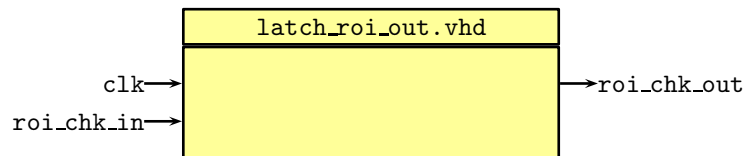
Figure B.16.: Diagram of the `latch_roi_out.vhd` ports.

B.12. `roi_latch.vhd`
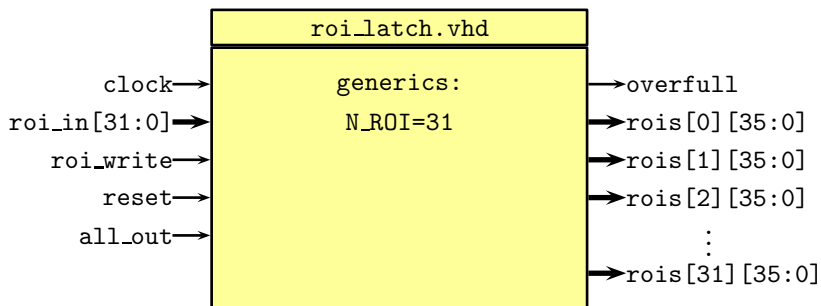
Figure B.17.: Diagram of the `roi_latch.vhd` ports.

With `roi_latch` the incoming ROI data are stored into a buffer with parallel outputs. The incoming ROIs are sent in two 32 bit words: The last 4 bit of the first word together with the second word contain the pixel coordinates for the ROIs. These are stored into a 36 bit wide buffer. With each intend ROI a new buffer entry is filled and is transmitted to the corresponding `rois[n][35:0]` output. The number of possible ROIs is set by the generic `N_ROI`. If this value shall be more than 31 the value in `roi_types` has to adjusted.

The standard value for non-set ROIs is `"FFFFFFFFF"` because this represents a ROI outside of the possible coordinates of one sensor. in case that more than `N_ROI` ROIs are send in, `overfull` is set to '1'. For this case as well as if `all_out='1'`, the last ROI is set to `"00002FFFF"`, which represents a ROI with the coordinates $(0,0)(767,255)$ which describes a ROI to cover the whole sensor (also called full-ladder-ROI).

31	30	29	28	27	26	25	24	23	22	21	20	19	18	17	16	15	14	13	12	11	10	9	8	7	6	5	4	3	2	1	0
							unused until now														flag		DHE-ID					$row_1[9:6]$			
		$row_1[5:0]$							$column_1$								row_2								$column_2$						

Table B.10.: The input and output ports of `roi_latch.vhd`.

Port		Description
`clock`	in	Clock input.
`roi_in[31:0]`	in	ROI input; alternating upper half and lower half.
`roi_write`	in	Write enable signal for ROI input.
`reset`	in	Reset signal; sets all ROIs in buffer to `"FFFFFFFF"`.
`all_out`	in	Input flag to write out all pixel; sets last ROI in buffer to full-ladder-ROI (`"00002FFFF"`).
`overfull`	out	Output flag if more ROIs than `N_ROI` were sent in. In this case last ROI in buffer to full-ladder-ROI (`"00002FFFF"`).
`rois[n][31:0]`	out	Parallel 36 bit outputs for all ROIs in buffer for further parallel check.

B.13. `HLT_data_split.vhd`

Figure B.18.: Diagram of the `HLT_data_split.vhd` ports.

The ROI data are handled internal as a 36 bit value containing the information of minimum and maximum for row and column. This value has to be split apart to get the single values for row and column thresholds. This splitting is done unclocked.

Table B.11.: The input and output ports of `HLT_data_split.vhd`.

Port		Description
`HLT_data[35:0]`	in	Data input for one ROI.
`HLT_r1[9:0]`	out	`HLT_data[35:26]` Data output of lower limit for rows.
`HLT_c1[7:0]`	out	`HLT_data[25:18]` Data output of lower limit for columns.
`HLT_r2[9:0]`	out	`HLT_data[17: 8]` Data output of upper limit for rows.
`HLT_c2[7:0]`	out	`HLT_data[ 7: 0]` Data output of upper limit for columns.

B.14. `Pixel_data_split.vhd`
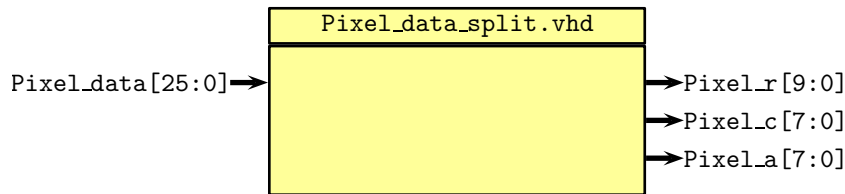
Figure B.19.: Diagram of the `Pixel_data_split.vhd` ports.

The pixel data are handled internal as a 26 bit value containing the information of row and column position as well as the ADC value from the corresponding pixel. This value has to be split apart to get the values for row, column and ADC value for each pixel. This splitting is done unclocked.

Table B.12.: The input and output ports of `Pixel_data_split.vhd`.

Port		Description
`Pixel_data[25:0]`	in	Data input for decoded data of one pixel.
`Pixel_r[9:0]`	out	`Pixel_data[25:16]` Data output of row address.
`Pixel_c[7:0]`	out	`Pixel_data[15: 8]` Data output of column address.
`Pixel_a[7:0]`	out	`Pixel_data[ 7: 0]` Data output of ADC value.

B.15. CompareIN.vhd
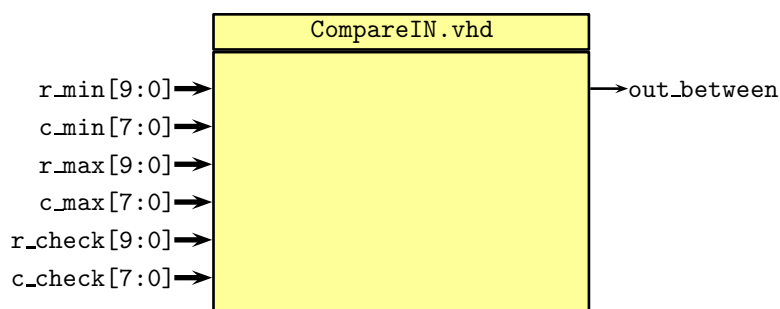
Figure B.20.: Diagram of the CompareIN.vhd ports.

The CompareIN processes a classical comparison of its input signals. The process is done unclocked. As input signals are provided the minimum and maximum values, as well as the values which have to be checked.

$$\text{out\_between} = (\text{r\_min} < \text{r\_check} < \text{r\_max}) \land (\text{c\_min} < \text{c\_check} < \text{c\_max})$$

The return value is a logical signal which tells whether the condition is fulfilled.

Table B.13.: The input and output ports of CompareIN.vhd.

Port		Description
r_min	in	Minimum row value
c_min	in	Minimum column value
r_max	in	Maximum row value
c_max	in	Maximum column value
r_check	in	Row value to check
c_check	in	Column value to check
out_between	out	Output signal; is high if check values are between limits

B.16. FIFO_32bit

This FIFO is generated by using the Xilinx core generator. For the functionality the important parameters are:

- Width of 32 bit for read and write.

- Depth of 512. This value can be adjusted to save provide bigger buffers. The size is chosen to use as little as possible blocks for the FIFO.

149

```
                  ┌──────────────────────────┐
                  │       FIFO_32bit         │
                  ├──────────────────────────┤
      rst ─────→  │        depth=512         │ ──→ dout[31:0]
   wr_clk ─────→  │      write width=32      │ ──→ full
   rd_clk ─────→  │      read width=32       │ ──→ empty
 din[31:0] ────→  │                          │ ──→ underflow
    wr_en ─────→  │                          │
    rd_en ─────→  │                          │
                  └──────────────────────────┘
```
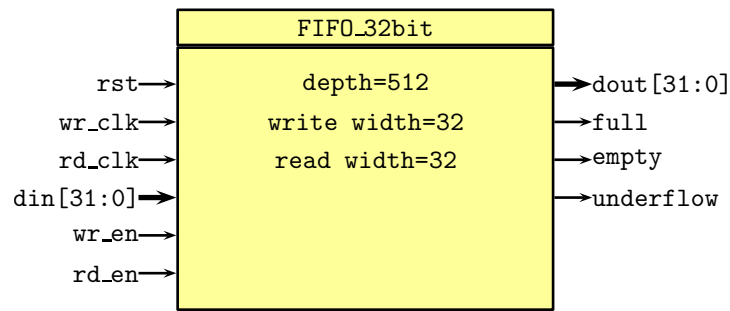
Figure B.21.: Diagram of the FIFO_32bit ports.

- Two independent clocks for read and write.

- Beside the standard signals for write enable, read enable, full and empty also the underflow is needed.

In the recent version it is chosen to have the FIFO in block RAM to save resources. For the functionality of the core it is not important which type of FIFO is generated but to be able to use the FPGA efficiently it is recommended to use block RAM.

B.17. FIFO_34bit

```
                  ┌──────────────────────────┐
                  │       FIFO_34bit         │
                  ├──────────────────────────┤
      rst ─────→  │        depth=512         │ ──→ dout[33:0]
   wr_clk ─────→  │      write width=34      │ ──→ full
   rd_clk ─────→  │      read width=34       │ ──→ empty
 din[33:0] ────→  │                          │ ──→ underflow
    wr_en ─────→  │                          │
    rd_en ─────→  │                          │
                  └──────────────────────────┘
```

Figure B.22.: Diagram of the FIFO_34bit ports.

This FIFO is generated by using the Xilinx core generator. For the functionality the important parameters are:

- Width of 34 bit for read and write.

- Depth of 512. This value can be adjusted to save provide bigger buffers. The size is chosen to use as little as possible blocks for the FIFO.

- Two independent clocks for read and write.

- Beside the standard signals for write enable, read enable, full and empty also the underflow is needed.

In the recent version it is chosen to have the FIFO in block RAM to save resources. For the functionality of the core it is not important which type of FIFO is generated but to be able to use the FPGA efficiently it is recommended to use block RAM.

B.18. `FIFO_36bit`
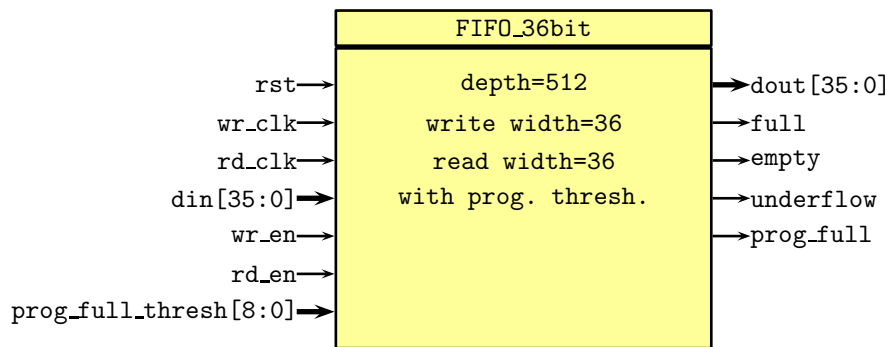
Figure B.23.: Diagram of the `FIFO_36bit` ports.

This FIFO is generated by using the Xilinx core generator. For the functionality the important parameters are:

- Width of 36 bit for read and write.

- Depth of 512. This value can be adjusted to save provide bigger buffers. The size is chosen to use as little as possible blocks for the FIFO.

- Two independent clocks for read and write.

- Beside the standard signals for write enable, read enable, full and empty also the underflow is needed.

- As special feature a programmable full signal together with a 9 bit input for its threshold is needed.

In the recent version it is chosen to have the FIFO in block RAM to save resources. For the functionality of the core it is not important which type of FIFO is generated but to be able to use the FPGA efficiently it is recommended to use block RAM.

B.19. `roi_types.vhd`

This file is used to define some specific types for the ROI selection core. Especially the array type `ROI_DATA_TYPE` to be able to provide the 31 parallel ROIs. If it is planned to use more than 31 ROIs the `N_ROI` variable in the `DHP_ROI_core` as well as the range of `ROI_DATA_TYPE` in this file have to be adjusted.

ADC	analog-to-digital-converter
AdvancedTCA	Advanced Telecommunications Computing Architecture
ATLAS	A Toroidal LHC ApparatuS
AMC	Advanced Mezzanine Card
ARICH	Aerogel Ring-Imaging Čerenkov detector
ASIC	Application-specific integrated circuit
BEPC II	Beijing Electron-Positron Collider II
BES III	Beijing Spectrometer III
BNL	Brookhaven National Laboratory
CAD	Computer-aided design
CDC	Central Drift Chamber
CDF II	Collider Detector at Fermilab II
CERN	french: Conseil Européen pour la Recherche Nucléaire, english: European Organization for Nuclear Research
CKM	Cabibbo-Kobayashi-Maskawa
CLEO	Cornell Electron Storage Ring
CMS	Compact Muon Solenoid
CN	Compute Node
CP	Charge, Parity
CPT	Charge, Parity, Time
CRC	cyclic redundancy check
DØ	DZero
DAQ	Data Acquisition
DATCON	Data Acquisition Tracking Concentrator Online Node
DCE	Data Clustering Engine
DDR2	double data rate 2
DEPFET	DEPleted Field Effect Transistor
DESY	german: Deutsches Elektronen-Synchrotron, english: German Electron Synchrotron

DHC	Data Handling Concentrator
DHE	Data Handling Engine
DHE-ID	Data Handling Engine Identifier
DHH	DEPFET Handling Hub
DHP	Data Handling Processor
DW	data word
ECL	Electromagnetic Calorimeter
FCE	FPGA Clustering Engine
FET	Field Effect Transistor
FIFO	First In, First Out
FPGA	Field Programmable Gate Array
GDL	Global Decision Logic
HLT	High Level Trigger
IHEP	Institute of High Energy Physics
JLU	Justus-Liebig-Universität Gießen
KEK	japanese: 高エネルギー加速器研究機構 kō-enerugī kasokuki kenkyū kikō, english: High Energy Accelerator Research Organization
KEKB	KEK-B-factory
KIT	Karlsruher Institut für Technologie
KLM	K_L^0 and μ detection
LHC	Large Hadron Collider
LHCb	Large Hadron Collider beauty
MicroTCA	Micro Telecommunications Computing Architecture
MSSM	Minimal Supersymmetric Standard Model
ONSEN	Online Selection Nodes
PID	Particle Identification
PXD	Pixel Detector
RAM	random-access memory
RJ45	standardized registered jack connector for data transmission
ROI	Region of Interests
SFP	small form-factor pluggable
SFP+	enhanced small form-factor pluggable
SLAC	Stanford Linear Accelerator Center
SM	Standard Model
SOR	start of row
SuperKEKB	SuperKEK-B-factory (upgrade of KEKB)
SVD	Silicon Vertex Detector
TOP	Time of Propagation
VHDL	VHSIC Hardware Description Language
VHSIC	Very High Speed Integrated Circuit
VXD	Vertex Detector
xFP	10 gigabit small form-factor pluggable
xTCA	here: card in AMC form-factor with some modifications

BIBLIOGRAPHY

[1]   GRIFFITHS, D. : *Introduction to Elementary Particles*. New York : John Wiley & Sons, 2008. – ISBN 978–3–527–61847–7

[2]   BERINGER, J. et al.: Review of Particle Physics. In: *Phys. Rev. D* 86 (2012), p. 010001

[3]   POVH, B. ; LAVELLE, M. ; RITH, K. ; SCHOLZ, C. ; ZETSCHE, F. : *Particles and Nuclei - An Introduction to the Physical Concepts*. Berlin Heidelberg : Springer Science & Business Media, 2006. – ISBN 978–3–540–36684–3

[4]   CHOI, S. et al.: Observation of a narrow charmonium-like state in exclusive $B^\pm \to K^\pm \pi^+ \pi^- J/\psi$ decays. In: *Phys.Rev.Lett.* 91 (2003), p. 262001. http://dx.doi.org/10.1103/PhysRevLett.91.262001. – DOI 10.1103/PhysRevLett.91.262001

[5]   AAIJ, R. et al.: Determination of the $X(3872)$ meson quantum numbers. In: *Phys.Rev.Lett.* 110 (2013), p. 222001. http://dx.doi.org/10.1103/PhysRevLett.110.222001. – DOI 10.1103/PhysRevLett.110.222001

[6]   SWANSON, E. : New Particle Hints at Four-Quark Matter. In: *Physics* 6 (2013), Jun, 69. http://dx.doi.org/10.1103/Physics.6.69. – DOI 10.1103/Physics.6.69

[7]   ABLIKIM, M. et al.: Observation of a Charged Charmoniumlike Structure in $e^+ e^- \to \pi^+ \pi^- J/\psi$ at $\sqrt{s} = 4.26$ GeV. In: *Phys.Rev.Lett.* 110 (2013), p. 252001. http://dx.doi.org/10.1103/PhysRevLett.110.252001. – DOI 10.1103/PhysRevLett.110.252001

[8]   LIU, Z. Q. et al.: Study of $e^+ e^- \to \pi^+ \pi^- J/\psi$ and Observation of a Charged Charmoniumlike State at Belle. In: *Phys.Rev.Lett.* 110 (2013), p. 252002. http://dx.doi.org/10.1103/PhysRevLett.110.252002. – DOI 10.1103/PhysRevLett.110.252002

[9]   *CKMfitter*. http://ckmfitter.in2p3.fr/www/results/plots_moriond14/ckm_res_moriond14.html, . – Accessed: 2014-12-01

[10] NAKAO, M. : Super B Factories. (2009)

[11] WOLFENSTEIN, L. : Parametrization of the Kobayashi-Maskawa Matrix. In: *Phys.Rev.Lett.* 51 (1983), p. 1945. http://dx.doi.org/10.1103/PhysRevLett.51.1945. – DOI 10.1103/PhysRevLett.51.1945

[12] KOBAYASHI, M. ; MASKAWA, T. : CP-Violation in the Renormalizable Theory of Weak Interaction. In: *Progress of Theoretical Physics* 49 (1973), p. 652–657. http://dx.doi.org/10.1143/PTP.49.652. – DOI 10.1143/PTP.49.652

[13] AUBERT, B. et al.: Observation of CP violation in the B^0 meson system. In: *Phys.Rev.Lett.* 87 (2001), p. 091801. http://dx.doi.org/10.1103/PhysRevLett.87.091801. – DOI 10.1103/PhysRevLett.87.091801

[14] ABE, K. et al.: Observation of large CP violation in the neutral B meson system. In: *Phys.Rev.Lett.* 87 (2001), p. 091802. http://dx.doi.org/10.1103/PhysRevLett.87.091802. – DOI 10.1103/PhysRevLett.87.091802

[15] BETHGE, K. ; SCHRDER, U. E.: *Elementarteilchen und ihre Wechselwirkungen.* New York : John Wiley & Sons, 2012. – ISBN 978–3–527–66216–6

[16] BEVAN, A. et al.: The Physics of the B Factories. (2014). – http://arxiv.org/abs/arXiv:1406.6311 – arXiv:1406.6311

[17] NEUBERT, S. ; WEITZEL, Q. : *Charmonium Spectroscopy - Part II.* 2005

[18] AUBERT, J. et al.: Experimental Observation of a Heavy Particle J. In: *Phys.Rev.Lett.* 33 (1974), p. 1404–1406. http://dx.doi.org/10.1103/PhysRevLett.33.1404. – DOI 10.1103/PhysRevLett.33.1404

[19] AUGUSTIN, J. et al.: Discovery of a Narrow Resonance in e^+e^- Annihilation. In: *Phys.Rev.Lett.* 33 (1974), p. 1406–1408. http://dx.doi.org/10.1103/PhysRevLett.33.1406. – DOI 10.1103/PhysRevLett.33.1406

[20] AUBERT, B. et al.: Observation of a broad structure in the $\pi^+\pi^- J/\psi$ mass spectrum around 4.26-GeV/c^2. In: *Phys.Rev.Lett.* 95 (2005), p. 142001. http://dx.doi.org/10.1103/PhysRevLett.95.142001. – DOI 10.1103/PhysRevLett.95.142001

[21] XIAO, T. ; DOBBS, S. ; TOMARADZE, A. ; SETH, K. K.: Observation of the Charged Hadron $Z_c^\pm(3900)$ and Evidence for the Neutral $Z_c^0(3900)$ in $e^+e^- \to \pi\pi J/\psi$ at $\sqrt{s} = 4170\,\mathrm{MeV}$. In: *Phys.Lett.* B727 (2013), p. 366–370. http://dx.doi.org/10.1016/j.physletb.2013.10.041. – DOI 10.1016/j.physletb.2013.10.041. – (arXiv:1304.3036)

[22] LANGE, S. : XYZ States - Results from Experiments. (2013)

[23] CHEN, W. ; DENG, W.-Z. ; HE, J. ; LI, N. ; LIU, X. et al.: XYZ States. In: *PoS* Hadron2013 (2013), p. 005. – (arXiv:1311.3763)

[24] ANTONIAZZI, L. et al.: Search for hidden charm resonance states decaying into J/ψ or ψ' plus pions. In: *Phys.Rev.* D50 (1994), p. 4258–4264. http://dx.doi.org/10.1103/PhysRevD.50.4258. – DOI 10.1103/PhysRevD.50.4258

[25] AUBERT, B. et al.: Study of the $B \to J/\psi K^- \pi^+\pi^-$ decay and measurement of the $B \to X(3872)K^-$ branching fraction. In: *Phys.Rev.* D71 (2005), p. 071103. http://dx.doi.org/10.1103/PhysRevD.71.071103. – DOI 10.1103/PhysRevD.71.071103

[26] ACOSTA, D. et al.: Observation of the narrow state $X(3872) \to J/\psi\pi^+\pi^-$ in $\bar{p}p$ collisions at $\sqrt{s} = 1.96$ TeV. In: *Phys.Rev.Lett.* 93 (2004), p. 072001. http://dx.doi.org/10.1103/PhysRevLett.93.072001. – DOI 10.1103/PhysRevLett.93.072001

[27] ABULENCIA, A. et al.: Measurement of the dipion mass spectrum in $X(3872) \to J/\psi\pi^+\pi^-$ decays. In: *Phys.Rev.Lett.* 96 (2006), p. 102002. http://dx.doi.org/10.1103/PhysRevLett.96.102002. – DOI 10.1103/PhysRevLett.96.102002

[28] AALTONEN, T. et al.: Precision Measurement of the $X(3872)$ Mass in $J/\psi\pi^+\pi^-$ Decays. In: *Phys.Rev.Lett.* 103 (2009), p. 152001. http://dx.doi.org/10.1103/PhysRevLett.103.152001. – DOI 10.1103/PhysRevLett.103.152001

[29] ABAZOV, V. et al.: Observation and properties of the $X(3872)$ decaying to $J/\psi\pi^+\pi^-$ in $p\bar{p}$ collisions at $\sqrt{s} = 1.96$ TeV. In: *Phys.Rev.Lett.* 93 (2004), p. 162002. http://dx.doi.org/10.1103/PhysRevLett.93.162002. – DOI 10.1103/PhysRevLett.93.162002

[30] AAIJ, R. et al.: Observation of $X(3872)$ production in pp collisions at $\sqrt{s} = 7$ TeV. In: *Eur.Phys.J.* C72 (2012), p. 1972. http://dx.doi.org/10.1140/epjc/s10052-012-1972-7. – DOI 10.1140/epjc/s10052–012–1972–7

[31] $X(3872) \to J/\psi\pi^+\pi^-$ invariant mass distribution. (2011)

[32] CHATRCHYAN, S. et al.: Measurement of the $X(3872)$ production cross section via decays to $J/\psi\pi\pi$ in pp collisions at $sqrts = 7$ TeV. In: *JHEP* 1304 (2013), p. 154. http://dx.doi.org/10.1007/JHEP04(2013)154. – DOI 10.1007/JHEP04(2013)154

[33] ABLIKIM, M. et al.: Observation of $e^+e^- \to \gamma X(3872)$ at BESIII. In: *Phys.Rev.Lett.* 112 (2014), Nr. 9, p. 092001. http://dx.doi.org/10.1103/PhysRevLett.112.092001. – DOI 10.1103/PhysRevLett.112.092001

[34] YUAN, C. et al.: Measurement of $e^+e^- \to \pi^+\pi^- J/\psi$ cross-section via initial state radiation at Belle. In: *Phys.Rev.Lett.* 99 (2007), p. 182004. http://dx.doi.org/10.1103/PhysRevLett.99.182004. – DOI 10.1103/PhysRevLett.99.182004

[35] HE, Q. et al.: Confirmation of the $Y(4260)$ resonance production in ISR. In: *Phys.Rev.* D74 (2006), p. 091104. http://dx.doi.org/10.1103/PhysRevD.74.091104. – DOI 10.1103/PhysRevD.74.091104

[36] AUBERT, B. et al.: Study of the $\pi^+\pi^- J/\psi$ Mass Spectrum via Initial-State Radiation at BABAR. (2008)

[37] WANG, X. et al.: Observation of Two Resonant Structures in e^+e^- to $\pi^+\pi^-\psi(2S)$ via Initial State Radiation at Belle. In: *Phys.Rev.Lett.* 99 (2007), p. 142002. http://dx.doi.org/10.1103/PhysRevLett.99.142002. – DOI 10.1103/PhysRevLett.99.142002

[38] AUBERT, B. et al.: Evidence of a broad structure at an invariant mass of 4.32GeV/c^2 in the reaction $e^+e^- \to \pi^+\pi^-\psi_{2S}$ measured at BaBar. In: *Phys.Rev.Lett.* 98 (2007), p. 212001. http://dx.doi.org/10.1103/PhysRevLett.98.212001. – DOI 10.1103/PhysRevLett.98.212001

[39] CLOSE, F. E. ; PAGE, P. R.: Gluonic charmonium resonances at BaBar and BELLE? In: *Phys.Lett.* B628 (2005), p. 215–222. http://dx.doi.org/10.1016/j.physletb.2005.09.016. – DOI 10.1016/j.physletb.2005.09.016

[40] ABLIKIM, M. et al.: Observation of a charged $(D\bar{D}^*)^\pm$ mass peak in $e^+e^- \to \pi D\bar{D}^*$ at $\sqrt{s} = 4.26$ GeV. In: *Phys.Rev.Lett.* 112 (2014), Nr. 2, p. 022001. http://dx.doi.org/10.1103/PhysRevLett.112.022001. – DOI 10.1103/PhysRevLett.112.022001

[41] AUSHEV, T. ; BARTEL, W. ; BONDAR, A. ; BRODZICKA, J. ; BROWDER, T. et al.: Physics at Super B Factory. (2010)

[42] SAKHAROV, A. D.: Violation of CP Invariance, C Asymmetry, and Baryon Asymmetry of the Universe. In: *JETP Letters* 5 (1967), p. 109

[43] Aaij, R. et al.: Searches for violation of lepton flavour and baryon number in tau lepton decays at LHCb. In: *Phys.Lett.* B724 (2013), p. 36–45. `http://dx.doi.org/10.1016/j.physletb.2013.05.063`. – DOI 10.1016/j.physletb.2013.05.063

[44] Ellis, J. R. ; Gaillard, M. ; Nanopoulos, D. V. ; Rudaz, S. : The Phenomenology of the Next Left-Handed Quarks. In: *Nucl.Phys.* B131 (1977), p. 285. `http://dx.doi.org/10.1016/0550-3213(77)90374-1`. – DOI 10.1016/0550–3213(77)90374–1

[45] Abe, T. et al.: Belle II Technical Design Report. (2010). – `http://arxiv.org/abs/arXiv:1011.0352` – arXiv:1011.0352v1

[46] *interactions.org - Beacons of Discovery - Tools of Particle Physics - High intensity.* `http://www.interactions.org/beacons/high-intensity`, . – Accessed: 2014-10-31

[47] *DESY - Belle & Belle II - Super KEKB and Belle II.* `http://belle2.desy.de/e103206`, . – Accessed: 2014-10-31

[48] *HEPHY Gallery - rev0_half_rendering.* `http://www.hephy.at/gallery2/v/electronics/mechanics/Renderings/rev0_half_rendering.png.html`, . – Accessed: 2014-10-31

[49] *HEPHY Gallery - VXD.* `http://www.hephy.at/gallery2/v/electronics/mechanics/Renderings/VXD.JPG.html`, . – Accessed: 2014-10-31

[50] Alonso, O. et al.: DEPFET Active Pixel Detectors for a Future Linear e^+e^- Collider. In: *IEEE Transactions on Nuclear Science* 60 (2013), p. 1457–1465. `http://dx.doi.org/10.1109/TNS.2013.2245680`. – DOI 10.1109/TNS.2013.2245680

[51] Ulrici, J. : *Bildgebung mit DEPFET-Pixelmatrizen für autoradiographische Anwendungen.* Bonn, Diss., 2003

[52] Moll, A. : *Data about Touschek background simulated and provided by Andreas Moll.* personal communication,

[53] Itoh, R. et al.: Data Flow and High Level Trigger of Belle II DAQ System. In: *IEEE Transactions on Nuclear Science* 60 (2013), p. 3720–3724. `http://dx.doi.org/10.1109/TNS.2013.2273091`. – DOI 10.1109/TNS.2013.2273091

[54] Levit, D. ; Konorov, I. ; Greenwald, D. ; Paul, S. : FPGA Based Data Read-Out System of the Belle 2 Pixel Detector. (2014). – `http://arxiv.org/abs/arXiv:1406.3864` – arXiv:1406.3864

[55] Levit, D. : *DHH Updates.* 2015

[56] Bilka, T. ; Casarosa, G. ; Frhwirth, R. ; Kleinwort, C. ; Kodys, P. et al.: Demonstrator of the Belle II Online Tracking and Pixel Data Reduction on the High Level Trigger System. (2014). – `http://arxiv.org/abs/arXiv:1406.4955` – arXiv:1406.4955

[57] Schnell, M. ; Dingfelder, J. ; Marinas, C. : Online data reduction with FPGA-based track reconstruction for the Belle II DEPFET Pixel Detector, Presented at the DPG Spring Meeting 2014, Mainz, 2014

[58] Schnell, M. : *Tracking Performance and Implementation of DATCON.* 2014

[59] MÜNCHOW, D. ; DINGFELDER, J. ; GESSLER, T. ; KONOROV, I. ; KÜHN, W. et al.: The data acquisition system of the Belle II Pixel Detector. In: *JINST* 9 (2014), p. C08009. `http://dx.doi.org/10.1088/1748-0221/9/08/C08009`. – DOI 10.1088/1748–0221/9/08/C08009

[60] GESSLER, T. ; KÜHN, W. ; LANGE, J. S. ; LIU, Z. ; MÜNCHOW, D. et al.: The ONSEN Data Reduction System for the Belle II PixelDetector. (submitted to the IEEE for possible publication)

[61] SPRUCK, B. et al.: The Belle II Pixel Detector Data Acquisition and Reduction System. In: *IEEE Transactions on Nuclear Science* 60 (2013), p. 3709–3713. `http://dx.doi.org/10.1109/TNS.2013.2281571`. – DOI 10.1109/TNS.2013.2281571

[62] XU, H. ; LIU, Z.-A. ; WANG, Q. ; ZHAO, J. ; JIN, D. et al.: An ATCA-based High Performance Compute Node for Trigger and Data Acquisition in Large Experiments. In: *Phys.Procedia* 37 (2012), p. 1849–1854. `http://dx.doi.org/10.1016/j.phpro.2012.02.509`. – DOI 10.1016/j.phpro.2012.02.509

[63] LIU, M. : *Adaptive Computing based on FPGA Run-time Reconfigurability*. Stockholm, Diss., 2011

[64] BUCHHOLZ, R. ; KRCKEN, W. ; MERCATOR, G. : *Die Mercator-Projektion - zu Ehren von Gerhard Mercator (1512 - 1594). Broschre*. Becker, 1994

[65] MÜNCHOW, D. : *Parallelisierung von Tracking Algorithmen für den Einsatz auf einer FPGA-Plattform*, Justus-Liebig-Universität Gießen, Diploma Thesis, 2009

[66] FERNANDES, L. A. ; OLIVEIRA, M. M.: Real-time line detection through an improved Hough transform voting scheme. In: *Pattern Recognition* 41 (2008), Nr. 1, 299 - 314. `http://dx.doi.org/http://dx.doi.org/10.1016/j.patcog.2007.04.003`. – DOI http://dx.doi.org/10.1016/j.patcog.2007.04.003. – ISSN 0031–3203

[67] *DESY - Test Beam - Brief Description*. `http://testbeam.desy.de/e130573`, . – Accessed: 2014-10-21

[68] *DESY - Test Beam - DESY II*. `http://testbeam.desy.de/e130573/e130791`, . – Accessed: 2015-01-09

[69] TIPLER, P. A. ; LLEWELLYN, R. A.: *Moderne Physik*. verbesserte Auflage. München : Oldenbourg Verlag. – ISBN 978–3–486–58275–8

[70] TSAI, Y.-S. : Pair production and bremsstrahlung of charged leptons. In: *Rev. Mod. Phys.* 46 (1974), Oct, 815–851. `http://dx.doi.org/10.1103/RevModPhys.46.815`. – DOI 10.1103/RevModPhys.46.815

[71] BETHE, H. : Zur Theorie des Durchgangs schneller Korpuskularstrahlen durch Materie. In: *Annalen der Physik* 397 (1930), p. 325400. `http://dx.doi.org/10.1002/andp.19303970303`. – DOI 10.1002/andp.19303970303

[72] HECK, M. : *Discussion about cluster rescue mechanism*. personal communication,

ACKNOWLEDGEMENT

Ich erkläre: Ich habe die vorgelegte Dissertation selbständig und ohne unerlaubte fremde Hilfe und nur mit den Hilfen angefertigt, die ich in der Dissertation angegeben habe.

Alle Textstellen, die wörtlich oder sinngemäß aus veröffentlichten Schriften entnommen sind, und alle Angaben, die auf mündlichen Auskünften beruhen, sind als solche kenntlich gemacht.

Bei den von mir durchgeführten und in der Dissertation erwähnten Untersuchungen habe ich die Grundsätze guter wissenschaftlicher Praxis, wie sie in der „Satzung der Justus-Liebig-Universität Gießen zur Sicherung guter wissenschaftlicher Praxis" niedergelegt sind, eingehalten.

Gießen, den 24. April 2015   David Münchow